PHASE FIELD MODELING OF MICROSTRUCTURE EVOLUTION IN CRYSTALLINE MATERIALS

A Dissertation

Submitted to the Faculty

of

Purdue University

by

Xiaorong Cai

In Partial Fulfillment of the

Requirements for the Degree

of

Doctor of Philosophy

December 2020

Purdue University

West Lafayette, Indiana

THE PURDUE UNIVERSITY GRADUATE SCHOOL
STATEMENT OF DISSERTATION APPROVAL

Dr. Marisol Koslowski, Chair

School of Mechanical Engineering

Dr. Carol Handwerker

School of Materials Engineering

Dr. John Blendell

School of Materials Engineering

Dr. Thomas Siegmund

School of Mechanical Engineering

Approved by:

Dr. Nicole L. Key

Head of the School Graduate Program

To my family.

ACKNOWLEDGMENTS

First and foremost, I would like to give my most sincere gratitude to my advisor, Dr. Marisol Koslowski. During my PhD studying, she gives me not only guidance and advise on my research, but also mental support. She inspires me and encourages me to always have a curious mind and a critical thinking. It is an honor for me to work for her and be her student.

Secondly, I would like to thank my committee member: Dr. Carol Handwerker, Dr. John Blendell and Dr. Thomas Siegmund. They provide a lot of invaluable insights and suggestions for my research work. I really appreciate their time and efforts.

I am also grateful to my group members: Akshay Dandekar, Camilo A. Duarte, Dr. Nicolò Grilli, Dr. Yifei Zeng and Dr. Ahmed OI Hamed. They all help me a lot and we share a wonderful time together.

Finally, I would like to thank my family for their love, patience and understanding.

TABLE OF CONTENTS

Page

LIST OF TABLES

LIST OF FIGURES

Figure Page

ABSTRACT

Xiaorong Cai Ph.D., Purdue University, December 2020. Phase Field Modeling of Microstructure Evolution in Crystalline Materials. Major Professor: Marisol Koslowski, School of Mechanical Engineering.

The material responses and the deformation pattern of crystals are strongly influenced by their microstructure, crystallographic texture and the presence of defects of various types.

In electronics, Sn coatings are widely used in circuits to protect conductors, reduce oxidation and improve solderability. However, the spontaneous growth of whiskers in Sn films causes severe system failures. Based on extensive experimental results, whiskers are observed to grow from surface grains with shallow grain boundaries. The underlying mechanism for these surface grains formation is crucial to predict potential whisker sites. A phase field model is coupled with a single crystal plasticity model and applied to simulate the grain boundary migration as well as the grain rotation process in Sn thin film, which are two possible mechanisms for surface grain formation. The grain boundary migration of three columnar grains is modeled and no surface grain is formed due to large plastic dissipation. In polycrystal Sn thin film, the nucleation of subgrains with shallow grain boundaries is observed for certain grain orientations on the film surface and the location of which corresponds to the regions with high strain energy density. From these simulations, it can be concluded that the grain rotation is the mechanism for whisker grain formation and the nucleated subgrains may be the potential whisker sites.

Sn-based solders are also widely used in electronics packaging. The reliability and the performance of SAC (Sn-Ag-Cu) solders are of key importance for the miniaturization of electronics. The interfacial reaction between Cu substrates and Sn-based solders forms two types of brittle intermetallic compounds (IMCs), Cu_6Sn_5 and Cu_3Sn.

During the operation, the interconnecting solders usually experience thermal loading and electric currents. These environmental conditions result in the nucleation of voids in Cu_3Sn layer and the growth of the IMCs. A phase field damage model is applied to model the fracture behavior in Cu/Sn system with different initial void densities and different Cu_3Sn thickness. The simulation results show the fracture location is dependent on the Cu_3Sn thickness and the critical stress for fracture can be increased by lowering the void density and Cu_3Sn thickness.

In alloys, the stacking fault energy varies with the local chemical composition. The effects of the stacking fault energy fluctuation on the strengthening of alloys are studied using phase field dislocation method (PFDM) simulations that model the evolution of partial dislocations in materials at zero temperature. Some examples are shown to study the dependency of the yield stress on the stacking fault energy, the decorrelation of partial dislocations in the presence of impenetrable and penetrable particles. Simulations of the evolution of partial dislocations in a stacking fault energy landscape with local fluctuations are presented to model the responses of high entropy alloys. A strong size dependency is observed with a maximum strength when the mean region size approaches the average equilibrium stacking fault width. The strength of high entropy alloys could be improved by controlling the disorder in the chemical misfit.

1. INTRODUCTION

Crystalline materials, although considered macroscopically homogeneous in macroscopic, exhibit heterogeneity at the mesoscale level. Over the past decades, extensive work has been done to study the influence of the microstructure and crystallographic texture on the properties of crystalline materials. The microstructure of crystalline materials is composed of grains with different orientations, thus rendering different mechanical and physical properties locally. So, it is important to take these factors into consideration when studying the microstructure evolution and the deformation in crystals. Along with the local misfit, defects of various types also have a great influence on the deformation mechanisms of crystalline materials. The arrangement of atoms of a crystal can be interrupted by crystallographic defects, examples of which are voids, dislocations, grain boundaries, stacking faults, twins and cracks. To model the local variation of material properties as well as the existence of the defects, phase field methods [1–5] are applied in different situations such as grain growth, grain rotation, phase formation, fracture and dislocations. In the phase field approach, the total free energy of the material is calculated and the evolution of microstructure follows an energy minimization process.

In Chapter 2, the problem of Sn whisker formation is studied. In the electronics industry, Sn coatings are widely used in electric circuits to protect conductors, reduce oxidation and improve solderability [6]. The spontaneous growth of whiskers in the Sn thin films arouses many concerns with regard to the reliability issues. Severe system failures are reported due to whisker growth. A number of experiments have been performed to investigate the whisker formation process. Sn grains are usually observed to form columnar structures with vertical grain boundaries after the deposition. However, the cross sections of Sn films from extensive experiments show that Sn whiskers grow from surface grains with shallow grain boundaries. Based on the

observations, different models of whisker nucleation mechanisms have been proposed to explain the microstructure evolution in the Sn thin films. Chason *et al.* [7,8] observed in the experiments that the whiskers grew out of the pre-existing grains and thus, proposed a strain-induced grain boundary migration model for creation of surface grains. Vianco *et al.* [9,10] and Kakeshita *et al.* [11] stated that the shallow grain boundaries were created by recrystallization.

However, there is still a gap between the experiments and the theories. It is almost infeasible to obtain the cross section of the whisker root during the whisker grain formation process in the experiments and yet no simulations have been performed to study this process. The evolution of the Sn grains from vertical boundaries to shallow boundaries remains unknown. Research showing microstructure evolution and whisker formation is needed to bridge the gap. The relationship between deformation and microstructure can be investigated by developing models and performing simulations at microscopic scale. Here, a phase field model of grain boundary migration and grain rotation are developed and applied to study the surface grain formation.

Sn-based solder materials are also widely used in the electronics packaging industry. In the recent years, the demand to decrease the size of the flip-chips increases the importance of the reliability and performance of solder joints. The interconnecting material widely used in Pb-free solder joints, are SAC (Sn-Ag-Cu). The interfacial reaction between Cu and Sn forms two types of brittle intermetallic compounds (IMCs), Cu_6Sn_5 and Cu_3Sn. During the operation of the electronic devices, the solder joints usually experience a current density up to 10^5 A/cm^2 [12], which results in a joule heating effect and mass transport due to electromigration. The on-going electromigration nucleates micro voids in the brittle IMC layers and affects the reliability of the solder joints. Besides the electric currents, the portable electronics may also experience shock loadings, mechanical loading or other operational environments.

To better understand the SAC solder performance in various environmental conditions, a phase field damage model is applied to study the voids evolution and crack

propagation in the solder joints. The effects of void density and the thickness of IMCs on the fracture evolution are investigated.

Chapter 4 presents the study of stacking fault strengthening of Ni-based alloys. The plasticity behavior of materials is reflected by the slipping of dislocations. Dislocations are linear defects, around which the atoms are not perfectly aligned. Under an applied deformation, dislocations can be generated and move. The interaction of the dislocations and the interaction between dislocations and other defects can result in the strengthening of the materials. The presence of dislocations increases the energy in materials compared with perfect crystals. A full dislocation can dissociate into two partial dislocations to lower its energy. Between two partial dislocations, a stacking fault will be generated. Stacking faults are planar defects which are defined as the disorder of the stacking sequence of layers in crystals.

In alloys, the energy of stacking faults varies with the local composition. The effects of the stacking fault energy fluctuations on the strengthening of alloys can be studied by tracking the evolution of partial dislocations in FCC metals at zero temperature. The classical deformation models are not capable of capturing the individual dislocation activities. The challenges of dislocation simulations not only lie in creating physically accurate models, but also using an appropriate simulation scale for efficiency. A phase field theory of dislocation dynamics is able to study dislocation behaviors such as dislocation loop nucleation, bowing out, pinching, and the formation of Orowan loops [13]. Phase field method is originally developed to solve interfacial problems, and is extended for a large variety of microscopic processes. Individual dislocations can be represented and evolved by phase field parameters. In this work, the influence of stacking fault energy on the strength of materials is studied by the motion of dislocations using phase field dislocation dynamics.

The structure of this report is constructed as follows.

The first chapter is the introduction, including the background knowledge, the research topics and the approaches used in the study.

Chapter 2 presents the surface grain formation in the Sn thin films. A single crystal plasticity model is discussed and the related parameters for material Sn are calibrated. A grain boundary migration model based on phase field method is introduced and applied to simulate compressive deformation of Sn grains. The effect of grain orientation on the shallow grain boundary formation is shown in the simulations. A grain nucleation mechanism is discussed and critical nucleation sizes are calculated for different grain boundary energies.

Chapter 3 contains the fracture evolution in the Cu/Sn solders. A phase field damage model is used to simulate the fracture behavior in the IMC layer. The effects of IMC thickness, the void density are studied to predict and improve the reliability of the solder joints.

Chapter 4 presents the effects of the stacking fault energy fluctuations on the strengthening of alloys. Relevant stacking fault strengthening models are reviewed and a phase field dislocation method (PFDM) is derived with emphasis on the incorporation of the gamma-surface. Some examples indicating the capabilities of PFDM are shown including the dependency of the yield stress on the stacking fault energy, the decorrelation of partial dislocations in the presence of impenetrable and penetrable particles. Simulations of the evolution of partial dislocations in a stacking fault energy landscape with local fluctuations are presented to model the responses of high entropy alloys.

2. SHALLOW GRAIN FORMATION IN TIN THIN FILM

Note part of this chapter is reproduced from "Shallow grain formation in Sn thin films"in Acta Materialia, 192, pp. 1-10 [14].

2.1 Introduction

With the development of the electronics industry, the reliability of electronic components becomes increasingly important in the electronics manufacturing. Sn is extensively used as coatings for its superior corrosion and oxidation resistance as well as easy bonding with other metals such as copper. Sn has long been used in alloys with Pb as solders and coatings for electric circuits in order to protect conductors, reduce oxidation and improve solderability [6]. The spontaneous growth of Sn whiskers and hillocks poses reliability concerns for inducing short circuits between electrical conductors. Adding Pb to Sn is an effective way to suppress whisker growth. Under the environmental regulations RoHS (Restriction of Hazardous Substances) [6], Pb-free manufacturing brings up whisker issues once again.

A number of experiments have been performed over years using different techniques to study Sn whisker growth. Experimental results show a variety of whisker morphologies including straight, kinked, bent, clustered, and plate-like [15]. The most common whisker morphology is either long and narrow or short and stubby. The length of whiskers is mostly around hundreds microns but some long whiskers can be up to millimeters. The growth morphology of Sn whiskers is highly likely related to the whisker nucleation mechanism, which still remains unclear. The objectives of this work is to apply phase field models to simulate two possible mechanisms and fully understand the whisker grain formation process.

2.1.1 Mechanisms for whisker growth

There are many significant whisker growth theories proposed to explain the growth mechanism. Several dislocation based theories were proposed during 1950s to 1970s. Peach [16] first came up with an explanation stating that a whisker grew at the tip by a screw dislocation in the center of the whisker. However, experiments performed by Koonce and Arnold [17] demonstrated that whiskers grew at the root rather than the tip. Later in 1953, Eshelby [18] proposed that whiskers grew by absorbing a dislocation loop generated by a Frank-Read source at the base. In the same year, Frank [19] stated that an rotating edge dislocation pinned by a screw dislocation would add an extra layer to the whisker root, and thus, extended the whisker length. However, the electron microscopy study of LeBret and Norton [20] suggested that the whiskers and the grains beneath them were defect free and contained no dislocations.

Other possible whisker formation mechanisms then came into being. Tu *et al.* [21] proposed that whisker growth could be analyzed as a model of grain boundary fluid flow, the rate of which was observed to be in agreement with whisker growth rate. Kakeshita *et al.* [11] studied grain size effect on Sn whisker growth. He proposed that a recrystallized grain would be generated and grew upwards as a whisker with the help of the internal stress. Vianco *et al.* [9, 10] stated dynamics recrystallization to be the mechanism for Sn whisker development. The recrystallized grains form to lower the strain energy and become the potential whisker sites. Chason *et al.* [7, 8] observed in the experiments that the whiskers grew out of the pre-existing grains and proposed a strain-induced grain boundary migration model for creation of surface grains. Handwerker and Blendell *et al.* [22,23] performed thermal cycling experiments and developed a model based on coupling between localized Coble creep and grain boundary sliding which explained the observed surface morphologies, the changing growth rate over time, and the dependence on the grain geometry.

The whisker growth mechanisms are closely related with the grain boundary structure. Sn grains in the thin films usually form columnar structures. The grains extend

to the bottom of the films with relatively vertical grain boundaries. Observations from extensive experiments show that whiskers always grow from surface grains with shallow grain boundaries. A typical example of the cross section of a whisker root is shown in reference [23]. The grain boundaries exhibit angles to the film normal, which is different from typical Sn grains in the films.

The nucleation process of whisker grains with shallow grain boundaries are debated. There is still controversy whether the whiskers grow from newly recrystallized grains or pre-existing grains. Since surface grains are potential whiskers, understanding the underlying mechanisms for surface grain formation can help predict whisker sites and thus, is of key importance for whisker study. Here, two possible mechanisms, grain boundary migration and grain nucleation, to create shallow grain boundaries are considered in the following sections.

2.1.2 Driving forces for whisker growth

It is well accepted that whisker growth is a stress relaxation mechanism in the thin films. The stress in the thin films comes from many different sources, such as residual stress from plating process, oxidation process, mechanical deformation and a mismatch of thermal expansion coefficients between Sn film and the substrate [6]. Cu_5Sn_5 IMC (intermetallic compound) formation at the Sn film/Cu substrate interface is one of the most important stress sources for spontaneous whisker growth. Since the diffusion of Cu atoms into Sn is much faster than that of Sn atoms into Cu, the intermetallics tend to grow in the Sn film rather than the substrate, resulting in a compressive stress in the Sn film [24–26]. The oxide layer on the top of Sn film effectively prevents the diffusion of atoms to the surface, thus, surpressing the relaxation of the stress.

Besides global stress from these sources, the local stress also plays an important part in the driving relaxation in the this film. Since $\beta-$Sn is a highly anisotropic material, the mismatch of the elasticity tensor and thermal expansion coefficients in

polycrystalline can not be neglected. The local hetergeneous stress distribution and microstructure of the film lead to multiple stress relaxation mechanisms rather than a single static process.

The other responses to relax stress except for whisker growth include: grain boundary sliding, cracks, extrusions, intrusions, grain boundary grooves, twins, recrystallization and grain growth [27]. The particular mechanisms dominating the stress relaxation process in the thin film depend on various factors. The factors include film thickness, global and local crystallographic texture, composition, microstructure, the substrate material, temperature and mechanical loading conditions and previous strain history.

In this work, two possible models for shallow grain boundary formation are discussed and simulated. In section 2.2, single crystal plasticity model is presented and calibration for Sn is discussed. In section 2.3, a phase field grain boundary migration model is developed to simulate the motion of grain boundary. In section 2.3.2, a deformation induced subgrain nucleation model is presented. 2d and 3d Simulations of single crystal, bicrystal and polycrystal are performed. The grain rotation for different orientations is shown and the stochastic analysis is performed.

2.2 Material Model

Sn has a body-centered-tetragonal crystal structure with highly anisotropic material properties. The yield stress of Sn is relatively low and therefore, plasticity plays a significant role even at small strains during deformation. In this section, a single crystal plasticity model is presented and calibrated to describe the plastic behavior of Sn. The models are implemented in Multiphysics Object Oriented Simulation Environment (MOOSE) [28] and are used to carry out all the simulations in this paper.

The conservation of momentum [29, 30] with the corresponding boundary conditions are:

$$\begin{aligned} \nabla \cdot \boldsymbol{\sigma} &= \rho \frac{\partial^2 \boldsymbol{u}}{\partial^2 t} \qquad in\ \Omega, \\ \boldsymbol{u} &= \boldsymbol{g} \qquad on\ \Gamma_g, \\ \boldsymbol{\sigma} \cdot \boldsymbol{n} &= \boldsymbol{t} \qquad on\ \Gamma_t, \end{aligned} \tag{2.1}$$

where $\boldsymbol{\sigma}$ is the Cauchy stress tensor, $\boldsymbol{u}$ is the displacement vector and ρ is the material density in the domain Ω. $\boldsymbol{g}$ and $\boldsymbol{t}$ are the prescribed displacement and traction on the boundary. The Cauchy stress tensor is related to the 2^{nd} Piola-Kirchhoff stress tensor as

$$\boldsymbol{\sigma} = \frac{1}{\det \boldsymbol{F}^e} \boldsymbol{F}^e \cdot \boldsymbol{S} \cdot \boldsymbol{F}^e \tag{2.2}$$

with $\boldsymbol{S} = \boldsymbol{C} \cdot \boldsymbol{E}^e$, where $\boldsymbol{E}^e = \frac{1}{2}\left(\boldsymbol{F}^{eT}\boldsymbol{F}^e - \boldsymbol{I}\right)$ is the Lagrange elastic strain, and $\boldsymbol{C}$ is the elasticity tensor.

2.2.1 Single Crystal Plasticity

In finite deformation, the deformation gradient, $\boldsymbol{F}$, is decomposed into its elastic, $\boldsymbol{F}^e$, and plastic, $\boldsymbol{F}^p$, parts as:

$$\boldsymbol{F} = \boldsymbol{F}^e \cdot \boldsymbol{F}^p \tag{2.3}$$

The elastic deformation gradient $\boldsymbol{F}^e$ represents the reversible material responses including rotation and stretching. The plastic deformation gradient $\boldsymbol{F}^p$ represents the irreversible response of material due to shearing. The rate of the plastic deformation gradient can be expressed as

$$\dot{\boldsymbol{F}}^p = \boldsymbol{L}^p \cdot \boldsymbol{F}^p \tag{2.4}$$

where $\boldsymbol{L}^p$ is the plastic part of the velocity gradient and it is represented by the sum of the slip rates, $\dot{\gamma^\alpha}$, over all the slip systems:

$$\boldsymbol{L}^p = \sum_{\alpha=1}^{N} \dot{\gamma}^\alpha \boldsymbol{m}^\alpha \otimes \boldsymbol{s}^\alpha \tag{2.5}$$

where N represents the total number of slip systems, $\boldsymbol{s}^\alpha$ is the unit vector in the slip direction, $\boldsymbol{m}^\alpha$ is the unit vector normal to slip plane in the slip system α and $\otimes$ is the

second order tensor product. The Schmid tensor, $\boldsymbol{m}^{\alpha} \otimes \boldsymbol{s}^{\alpha}$ projects the amounts of slip on slip system α on the reference configuration. The evolution of the slip on each slip plane follows a power-law flow rule as a function of the critical resolved shear stress τ_c^{α} and the resolved shear stress τ^{α}:

$$\dot{\gamma^{\alpha}} = \dot{\gamma_0} \left| \frac{\tau^{\alpha}}{\tau_c^{\alpha}} \right|^n sign\left(\tau^{\alpha}\right) \tag{2.6}$$

where $\dot{\gamma_0}$ is a reference strain rate and n is the strain rate slip sensitivity parameter. The sign function $sign()$ gives values +1 or -1, depending on the sign of resolved shear stress. A hardening law is used to represent the increase of slip resistance due to dislocations accumulation on all slip systems, known as latent hardening:

$$\dot{\tau_c^{\alpha}} = \sum_{1}^{N} h_{\alpha\beta} \left| \dot{\gamma^{\beta}} \right|, \tag{2.7}$$

with an initial threshold stress $\tau^{\alpha}(t=0) = \tau_0^{\alpha}$, and a hardening matrix of the form:

$$h_{\alpha\beta} = q_{\alpha\beta} \left[h_0 \left(1 - \frac{\tau_c^{\beta}}{\tau_s} \right)^a \right] \tag{2.8}$$

where $h_{\alpha\beta}$ is the hardening matrix, h_0, a and τ_s are slip hardening parameters. h_0 is the initial hardening rate and τ_s is the saturated slip resistance. The parameter $q_{\alpha\beta}$ is the latent hardening ratio, that specifies the ratio of the hardening between the second slip system β to that of the primary slip system α [31]. The value of $q_{\alpha\beta}$ is taken as

$$q_{\alpha\beta} = \begin{cases} 1.0 & \text{if } \alpha, \beta \text{ are coplanar} \\ 1.4 & \text{otherwise} \end{cases} \tag{2.9}$$

2.2.2 Calibration for Sn

Sn has a BCT crystal structure with lattice parameter $a = b = 583.18\ pm$ and $c = 318.19\ pm$ [32], shown in Figure 2.1. There are 32 possible slip systems reported in the literature [33–35], listed in Table 2.1 and shown in Figure 2.2. The slip systems in the table are ordered according to the slip resistance, τ_0, from low to high. The elastic constants of Sn are reported in Table 2.2.

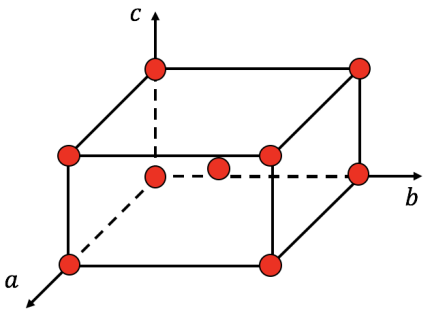

Figure 2.1. Crystal structure of β-Sn.

Table 2.1. Slips systems for Sn. [33–35]

Number	Slip system	Multiplicity	τ_0[MPa]
1	$\{100\} < 001 >$	2	20
2	$\{110\} < 001 >$	2	20
3	$\{100\} < 010 >$	2	20
4	$\{110\} < 1\bar{1}1 > /2$	4	22
5	$\{110\} < 1\bar{1}0 >$	2	22
6	$\{100\} < 011 >$	4	22
7	$\{001\} < 010 >$	2	25
8	$\{001\} < 110 >$	2	25
9	$\{011\} < 01\bar{1} >$	4	25
10	$\{211\} < 01\bar{1} >$	8	25

Table 2.2. Elastic constants (GPa) of Sn. [33–35]

C_{11}	C_{22}	C_{33}	C_{44}	C_{55}	C_{66}	C_{12}	C_{23}	C_{13}
72.3	72.3	88.4	22.0	22.0	24.0	59.4	35.8	35.8

The work by Bieler [33–35] is used here to calibrate the single crystal plasticity model in Equation 2.6. The parameters $n = 2.5$ and $\dot{\gamma}_0 = 0.00025s^{-1}$ are chosen

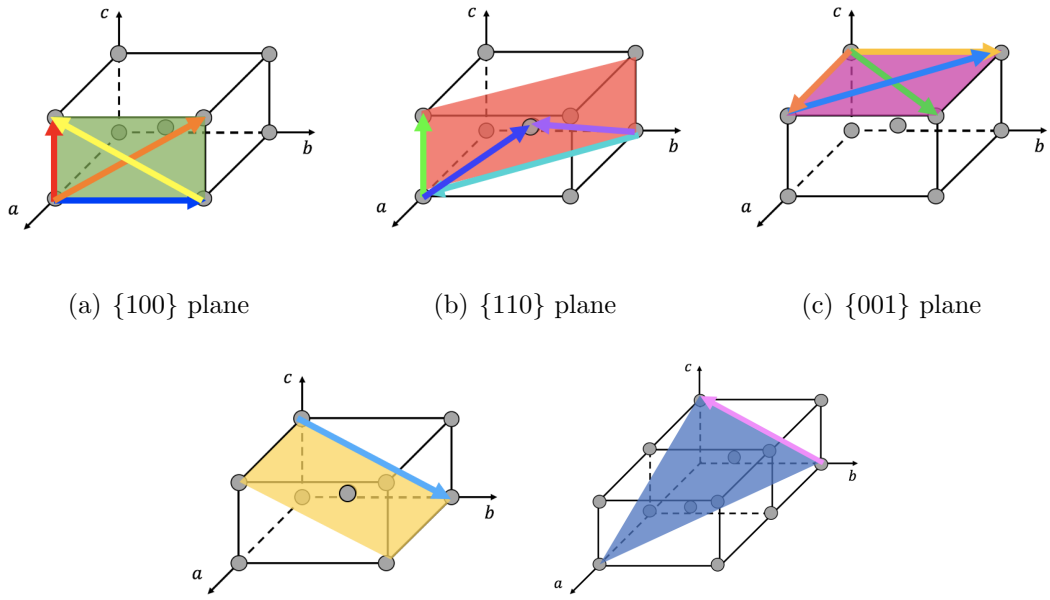

(a) {100} plane (b) {110} plane (c) {001} plane

(d) {011} plane (e) {211} plane

Figure 2.2. Slip systems of Sn.

by fitting the stress-strain curves reported in Bieler′s work [33]. These values are reasonable compared to copper [29, 36]. The values of the other parameters in the model are listed in Table 2.3. The stress-strain curves using these parameters are compared to Bieler's results [33] in Figure 2.3 with the crystal orientation and loading axis indicated in the figure. The yield stress calculated from this model also fits with the experimental data reported by Duzgun *et al.* [37] and Tucker *et al.* [38].

Table 2.3. Material parameters used in crystal plasticity for Sn. [33–35]

$\tau_s(MPa)$	$h_0(MPa)$	a	n	$\dot{\gamma}_0(s^{-1})$
30	80	2.0	2.5	0.00025

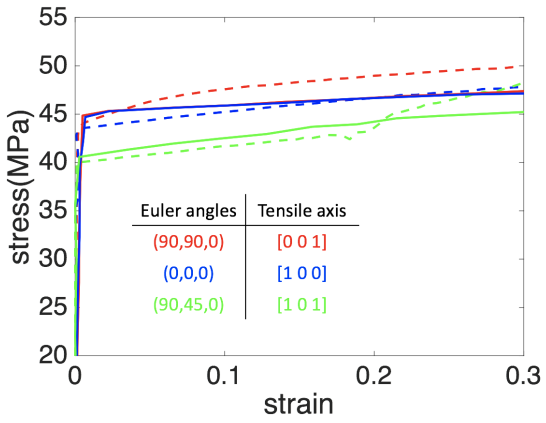

Figure 2.3. Strain-stress curves using the model presented above. The plasticity parameters for solid lines are reported in Table 2.3. The dashed lines are extracted from Bieler's work [33]. The Bunge Euler angles and the tensile directions are specified in the legend.

2.2.3 Capability of Model

The single crystal plasticity shown in this section is capable of describing comprehensive material behaviors. In the experiments, a strong rate-dependent behavior of Sn is observed [38, 39]. In Figure 2.4, different strain rates, 0.01 s^{-1}, 0.005 s^{-1} and 0.001 s^{-1}, are applied to a single crystal. The yield stress increases with the strain rate. When incremental strain is applied, the incremental deformation gradient, $\dot{\boldsymbol{F}}$, is calculated and the stress tensor, $\boldsymbol{\sigma}$, is updated. So the material response is dependent on the loading path, which is the strain rate.

In Figure 2.5, cyclic loading is applied to a single crystal. The initial compressive strength is lower than the initial tensile strength, which can be explained by Bauschinger effect. After two cycles, the material is hardened.

These simulations show the capability of the single crystal plasticity model. It is able to describe the strain rate hardening, cyclic hardening as well as latent hardening. Using this model, the plastic behavior of Sn can be captured and the evolution of microstructure can be predicted.

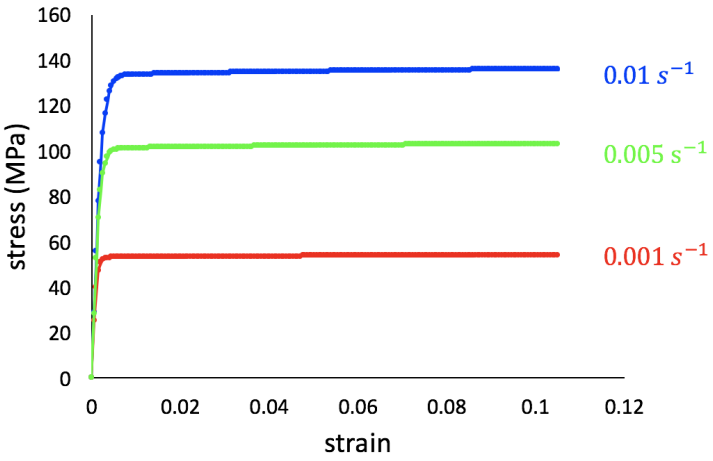

Figure 2.4. Strain-stress curves using the single crystal plasticity model. The applied strain rate is indicated in the figure.

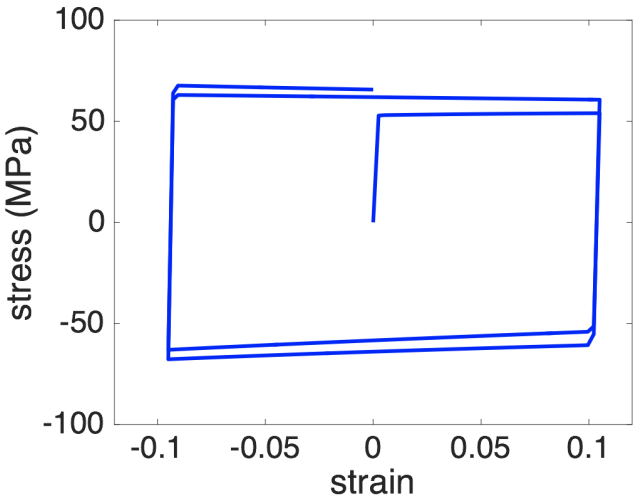

Figure 2.5. Strain-stress curves for cyclic loading.

2.3 Shallow grain formation simulations

The whisker growth process is closely related with the grain boundary structure. Sn grains in the as-deposited thin films usually form columnar structures. The grains

extend to the bottom of the films with relatively vertical grain boundaries [6, 24]. However, observations from extensive experiments show that whiskers always grow from surface grains with shallow grain boundaries [22, 23].

The origin of these surface grains are debated. The experimental results by Chason *et al.* [7, 40] show that whiskers grow from pre-existing grains. The transition from vertical to shallow grain boundary is a boundary migration process and the orientation of the whisker grains do not change. Therefore, a strain induced grain boundary migration model is proposed to explain for shallow grain formation.

Another possible mechanism proposed to nucleate shallow grains is recrystallization [9, 20, 24, 41, 42]. Recrystallization is the rotation of the lattice, following by the formation of new grain boundaries. The nucleated new grain with oblique boundary can be potential whiskers grains.

In this section two different mechanisms are explored, grain boundary migration and recrystallization. Finite element simulations are carried out to studied the two possible mechanisms for shallow grain formation.

2.3.1 Grain boundary migration

Figure 2.6 is a schematic diagram that represents the grain boundary motion process to form a shallow grain. The as-deposited Sn film structure contains columnar grains as shown in Figure 2.6 (a). In Figure 2.6 (b), residual or thermo-mechanical stresses will make the grain boundary move to reduce the strain energy while the grain boundary is pinned on the surface due to the attachment to the oxide layer and the bottom due to the substrate. When the grain boundaries coalesce, shallow grains are formed in Figure 2.6(c). However, Chason *et al.* [7] demonstrated that larges stresses than the one expected during thin film relaxation are needed to nucleated these shallow grains. To study this process a phase field model is presented and used to simulate grain boundary migration.

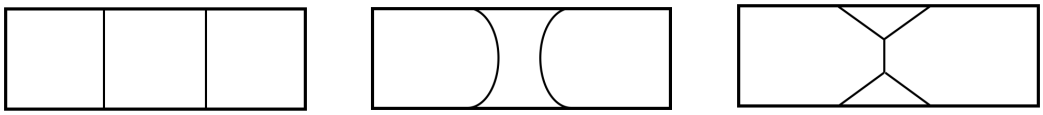

(a) Initial grain structures (b) Grain boundary migration (c) Shallow grain formation

Figure 2.6. Schematic diagram of the grain boundary migration model.

In the phase field model each grain is represented by a phase field parameter η [1, 36, 43] The parameter η_a is equal to 1 inside the grain a and 0 outside. Figure 2.7 is a representation showing the values of two phase field parameters η_1 and η_2 in two neighbouring grains.

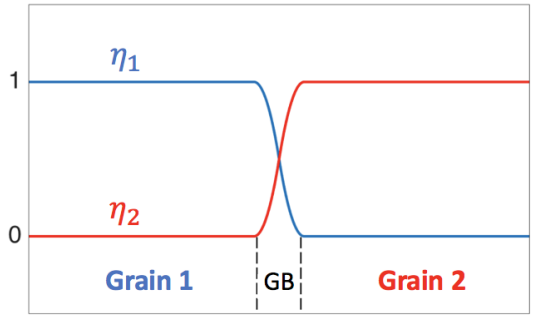

Figure 2.7. A schematic profile of phase field parameters of two neighboring grains. The blue line represents the phase field parameter value for grain 1 and the red line represents grain 2.

Time dependent Ginzburg-Landau equations are solved to calculate the evolution of the non-conserved order parameters η_a [43] by minimization of the free energy:

$$\frac{\partial \eta_a}{\partial t} = -L\frac{\delta \Psi}{\delta \eta_a}, \ a = 1 \ to \ N \tag{2.10}$$

where t is time and L is related to the grain boundary mobility. The total free energy Ψ includes the grain boundary energy, the elastic energy and plastic dissipation [43–45] and it can be expressed as

$$\Psi(\boldsymbol{\eta}, \boldsymbol{F}^e, \boldsymbol{F}^p) = \int_V \left(f_{bulk} + f_{grad} + \psi^e(\boldsymbol{F}^e) + \psi^p(\boldsymbol{F}^p)\right) dV \tag{2.11}$$

where $\boldsymbol{\eta}$ contains all the phase fields $\boldsymbol{\eta} = (\eta_1, \eta_2, \eta_3, ...)$, V is the volume of the whole system, N is the total number of grains and κ_a is the energy gradient coefficient. Each terms will be explained in detail in the following.

The first two terms are the functional of the phase field parameters η and their gradients. The homogeneous bulk free energy density f_{bulk} follows the model proposed by Moelans *et al.* [1]:

$$f_{bulk} = \mu \left(\sum_a^N \left(\frac{\eta_a^4}{4} - \frac{\eta_a^2}{2} \right) + \frac{3}{2} \sum_{a=1}^N \sum_{b \neq a}^N \eta_a^2 \eta_b^2 + \frac{1}{4} \right) \tag{2.12}$$

where μ is a parameter related to the grain boundary energy and width. The value of γ is chosen to be 1.5 according to Moelans *et al.* [1]. From the definition in Equation 2.12 the value of f_{bulk} is always 0 inside each grain and is only non-zero in the grain boundaries.

The second term calculates the gradients of the phase field parameters. It controls the width of the grain boundaries and is defined as:

$$f_{grad} = \sum_a^N \frac{\kappa}{2} (\nabla \eta_a)^2 \tag{2.13}$$

The coefficient κ_a is calculated from the grain boudnary energy and width, which is strictly positive. In the grain boundary where the gradients are non-zero, this term would attribute to the increase of the total energy. The integration of the first two terms accounts for the total energy due to the presence of grain boundary in a system.

The elastic energy density ψ^e is

$$\psi^e = \frac{1}{2} \boldsymbol{E}^e : \boldsymbol{C} : \boldsymbol{E}^e \tag{2.14}$$

where $\boldsymbol{C}$ is the fourth-order elasticity tensor and $\boldsymbol{E}^e$ is the elastic strain.

The plastic energy density ψ^p can be written as [36]

$$\psi^p = A\left(\sum_{\alpha}\sum_{\beta} a_{\alpha\beta}\left|\gamma^{\alpha}\gamma^{\beta}\right|\right)^{3/4} \tag{2.15}$$

Here, $a_{\alpha\beta}$ is an interaction coefficient associated with the dislocations on each slip system, and the value is taken to be the same as $q_{\alpha\beta}$. γ^{α} is the slip strain of slip system α defined in Equation 2.6. A is a parameter related with heat dissipation during plastic work, the value of which depends upon specific materials. By fitting to experimental data [36], A is inversely proportional to the the average slip strain.

$$A = \frac{1}{k \cdot \bar{\gamma}}\text{MPa} \tag{2.16}$$

where k is a coefficient taken as 7.2 following [36]. The average slip strain $\bar{\gamma}$ over all the slip systems is $\bar{\gamma} = \frac{1}{N}\sum_{\alpha}\gamma^{\alpha}$.

An interpolation function $h(\eta_a)$ is used to calculate the elastic and plastic energy density at any point of the domain including the grain boundaries.

$$h(\eta_a) = \frac{1}{2}\left(1 + \sin\left(\pi\left(\eta_a - 0.5\right)\right)\right) \tag{2.17}$$

Here, the value of $h(\eta_a)$ is 0 when $\eta_a = 0$ and 1 when $\eta_a = 1$. Using Equation 2.17 the elastic energy density ψ^e in the grain boundaries can be calculated as a weighted average of the elastic energy density within neighboring grains.

$$\psi^e = \frac{\sum_a^N h(\eta_a)\,\psi_a^e}{\sum_a^N h(\eta_a)} \tag{2.18}$$

and its partial derivative with respect to the phase field parameter η_a is

$$\frac{\partial\psi^e}{\partial\eta_a} = h'(\eta_a)\,\frac{{\psi^e}_a - \psi^e}{\sum_a^N h(\eta_a)} \tag{2.19}$$

Similar to the elastic energy density, the derivative of the plastic energy density ψ^p with respect to the phase field parameter η_a is

$$\frac{\partial\psi^p}{\partial\eta_a} = h'(\eta_a)\,\frac{{\psi^p}_a - \psi^p}{\sum_a^N h(\eta_a)} \tag{2.20}$$

The three parameters used in Allen-Cahn equation, L, κ, μ are related to three grain boundary properties: the grain boundary mobility M_{GB}, the grain boundary energy γ_{GB} and the interfacial width l_{GB} [1] as follows:

$$\begin{aligned} L &= \frac{4}{3}\frac{M_{GB}}{l_{GB}} \\ \kappa &= \frac{3}{4}\gamma_{GB} l_{GB} \\ \mu &= 6\frac{\gamma_{GB}}{l_{GB}} \end{aligned} \tag{2.21}$$

The upper bound of the grain boundary energy γ_{GB} can be estimated from the unstable stacking fault energy [46] of Sn which is in the range 0.1 to 0.4 J/m^2 [47]. The grain boundary energy reported by Chason *et al.* is 1 to 100 mJ/m^2. So here its value is taken to be 0.1 J/m^2. The grain boundary mobility, M_{gb}, grain boundary energy, γ_{gb}, and grain boundary width, l_{gb}, used in the simulations are approximated values, and are listed in Table 2.4. The grain boundary evolution is predicted by solving simultaneously Equation 2.1 with the plasticity model in Equations 2.5, 2.6, and 2.7, and the system in Equation 2.10.

Table 2.4. Grain boundary properties used in the simulations.

M_{GB} $(m^4/(Js))$	γ_{GB} (J/m^2)	l_{GB} (um)
2×10^{-8}	0.1	50

The evolution of three columnar grains is simulated to study grain boundary migration using 2D plane strain condition. A schematic figure of the simulation geometry and boundary conditions is shown in Figure 2.8 (a). The bottom surface is fixed in the vertical direction and the left boundary is fixed in the horizontal direction. A compressive displacement is applied to the right boundary at strain rate of $0.001s^{-1}$. The grain boundaries are pinned on the top surface and the bottom. Material properties of Sn used in the simulations are listed from Table 2.1 to Table 2.4. Different grain orientations are assigned to each grain and the inverse pole figure (IPF) coloring is used to represent the orientations. The grain width is $w = 3.5\mu m$ and three

different film thickness are used, $l_1 = 2\ \mu m$, $l_2 = 3.5\ \mu m$, and $l_3 = 5\ \mu m$. The grain boundaries are indicated in red from (b) to (d).

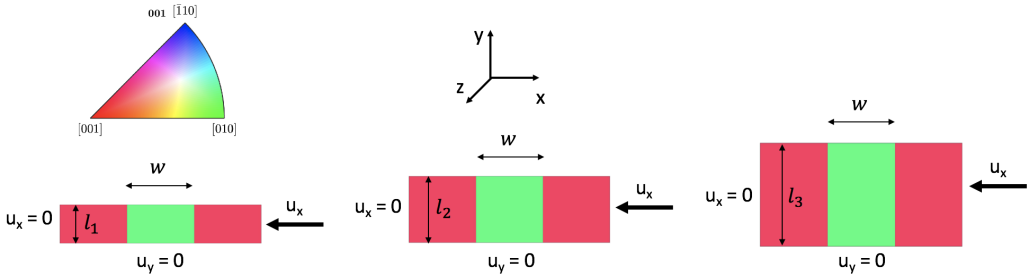

(a) Initial configuration

(b) 6 % strain without plasticity

(c) 10 % strain without plasticity

(d) 10 % strain with plasticity

Figure 2.8. Grain boundary migration simulations. The amount of applied strain is indicated in the figure.

In Figure 2.8 (b) and (c) where the plasticity is not considered in the simulations, the only way to minimized the energy in the material is by grain boundary migration. Under this condition, the stress in the film reaches 4 GPa when the applied strain is 6%. As is shown in the figures, when the material is compressed, the two nearby

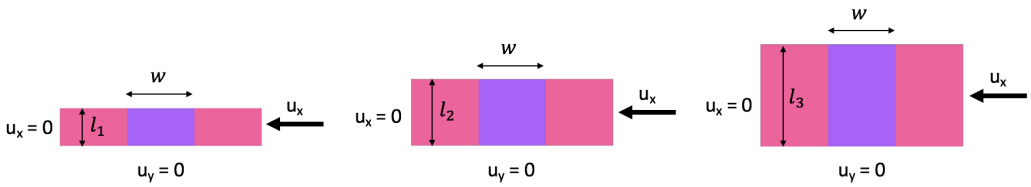

(a) Initial configuration

(b) 6 % strain without plasticity

(c) 10 % strain without plasticity

(d) 10 % strain with plasticity

Figure 2.9. Grain boundary migration simulations. The amount of applied strain is indicated in the figure.

boundaries move closer and coalesce due to the large strain energy. Then they become shallow grain boundaries and surface grains are formed.

In Figure 2.8 (d) where crystal plasticity is considered, the grain boundaries hardly move and no shallow grain boundary is formed after applying 10% of strain. The reason is that the plastic behavior of Sn greatly helps the stress relaxation in the material, and thus the strain energy in the material is very low. Since the grain boundaries are pinned at the surface and the bottom, the strain energy is not sufficient for the creation of the boundary curvature. The same behavior is observed for different

grain orientations and different film thickness, see Figure 2.9. Simulation results show that the strain driven grain boundary migration is not likely to happen in Sn thin film.

In the experiments by Chason *et al.* [7], the average grain size is around $3\mu m$, which is comparable to our simulation. The compressive stress in the thin film is reported to be 20 MPa. However, using a bulk material nucleation model, the stress required for nucleation is within 142 MPa to 45 GPa, which is much higher than the yield stress of Sn. Taking plasticity into consideration, it is unlikely to nucleate these shallow grains by grain boundary migration.

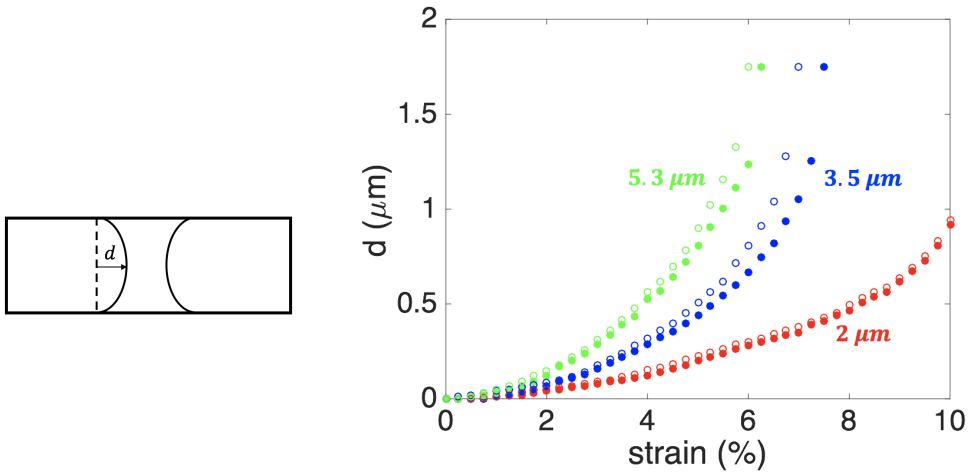

(a) (b)

Figure 2.10. (a) A schematic figure of grain boundary migration distance. (b) Grain boundary migration distance d vs applied strain. The solid and hollow circles represent two elastic simulations with different grain orientations, see Figure 2.8 and Figure 2.9.

Figure 2.10 shows the grain boundary migration distance as a function of the applied strain. The hollow circles represent the elastic simulations in Figure 2.8 and the solid circles represent the elastic simulations in Figure 2.9. The plot compares the grain boundary migration distances for three different film thickness. When the film is thicker, there is less curvature needed for the boundary to coalesce, and thus less

strain energy needed to move the grain boundary. For different grain orientations, the energy difference between two nearby grains are different, so the migration velocities can differ. This indicates that the grain boundary migration and the microstructure evolution are greatly influenced by the film texture.

2.3.2 Deformation induced subgrain nucleation

During deformation, the grains of a polycrystal develop heterogeneous deformation patterns with local variations of the stress and strain fields. These heterogenous fields are of key importance in microstructural evolution, such as grain growth and recrystallization [48], as well as in strain hardening, Hall-Petch effect and inelastic recovery [46, 49]. When polycrystalline metals are strained the crystallographic slip varies from grain to grain and causes local lattice rotations within a grain. These changes of lattice orientation may develop to maintain the compatibility of the deformation with neighboring grains and are accommodated by geometrically necessary dislocations (GND). These dislocation structures inside the original grain form internal grain boundaries leading to new smaller grains or subgrains. The lattice rotation or GND can be used to identify the new grains. Both quantities are measured by the elastic and plastic deformation gradients as follows.

In the continuum framework, total deformation gradient $\boldsymbol{F}$ has to be compatible, while $\boldsymbol{F}^e$ and $\boldsymbol{F}^p$ may not necessarily be compatible. The incompatibility in the lattice comes from the dislocations. Nye's dislocation tensor measures the incompatibility of the plastic part of the deformation gradient, and it is related to the dislocation distribution. The connection between the deformation fields and dislocation structures is established by Nye's dislocation tensor [50, 51]:

$$\boldsymbol{\alpha} = curl \boldsymbol{F}^p \tag{2.22}$$

Other equivalent defect measurements have been used. For example, Cermelli and Gurtin [52] define the GND density tensor as

$$\boldsymbol{\alpha} = \frac{\boldsymbol{F}^p}{\det(\boldsymbol{F}^p)} curl \boldsymbol{F}^p = \det(\boldsymbol{F}^e)\boldsymbol{F}^{e-1} curl \boldsymbol{F}^{e-1} \tag{2.23}$$

where the last equality is obtained imposing the compatibility of $\boldsymbol{F}$.

In finite deformation, the total deformation gradient $\boldsymbol{F}$ can be decomposed into an elastic part and a plastic part. The elastic part of the deformation gradient can be further decomposed into a rotation tensor $\boldsymbol{R}^e$, and the stretch tensor, $\boldsymbol{U}^e$. Therefore, the rotation of the lattice can be obtained from the elastic deformation gradient using polar decomposition:

$$\boldsymbol{F}^e = \boldsymbol{R}^e \boldsymbol{U}^e \tag{2.24}$$

The rotation tensor can be written as a function of the rotation angle, θ, and the rotation axis $\boldsymbol{w}$ using Rodrigues rotation formula:

$$\boldsymbol{R}^e{}_{ij} = \cos\theta \delta_{ij} + w_i w_j (1 - \cos\theta) + \epsilon_{ikj} w_k \sin\theta \tag{2.25}$$

where δ_{ij} is the Kronecker delta and ϵ_{ikj} is the permutation tensor.

The lattice rotation angle θ can be calculated from [53]

$$\boldsymbol{R}^e - \boldsymbol{R}^{eT} = 2\sin\theta \begin{bmatrix} 0 & -w_3 & w_2 \\ w_3 & 0 & -w_1 \\ -w_2 & w_1 & 0 \end{bmatrix} \tag{2.26}$$

The low angle rotation (θ below 2 degrees) are associated with GND, and higher values with subgrain and new grain boundaries [54–57]. Here, the formation of new subgrain structures are identified as the regions with lattice rotation larger than 3°.

2.3.3 Single grain simulations

As an example of the effect of the crystal orientation on the formation of subgrains, the deformation of a single grain with different orientations is analyzed. A compressive displacement is applied on one boundary with a strain rate $0.001s^{-1}$ while the other

three boundaries are fixed, see Figure 2.11. Plane stress condition is applied. Different orientations are created by rotating an angle α along the [110] direction.

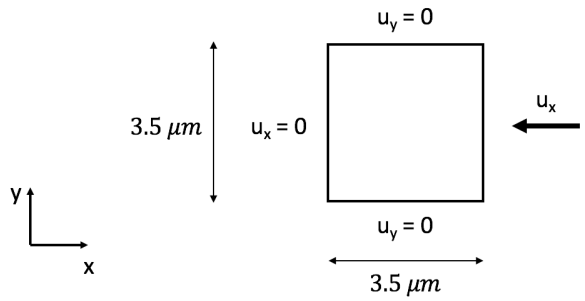

Figure 2.11. A schematic figure of single crystal lattice rotation simulation.

Figure 2.12 shows lattice rotation in the single crystals after applying 10% strain. A common representation of rotation, Rodrigues vector $\boldsymbol{\lambda}$ is shown in black and is defined as

$$\boldsymbol{\lambda} = \tan\left(\frac{\theta}{2}\right)\boldsymbol{w} \tag{2.27}$$

where the vector direction is the rotation axis $\boldsymbol{w}$ and the length of the vector is characterized by the rotation angle θ. The Rodrigues vector field indicates the rotation axis and the amount of rotation. The largest rotation occurs at the boundaries and subgrain stuctures are created. The subgrains are defined as the area where the rotation angle is larger than 3°.

In Figure 2.13, the subgrain fraction is plotted as a function of α. For 2d simulations on x-y plane, the rotation along [110] direction is symmetric along 90 degrees, as observed in the plot.

2.3.4 Bicrystal simulations

To better study the subgrain structures formation, bicrystal simulations are performed with random grain orientations. The grain size is $3.5\mu m \times 3.5\mu m$. Figure 2.14 is a schematic figure of a bicrystal under plane strain condition. The bottom bound-

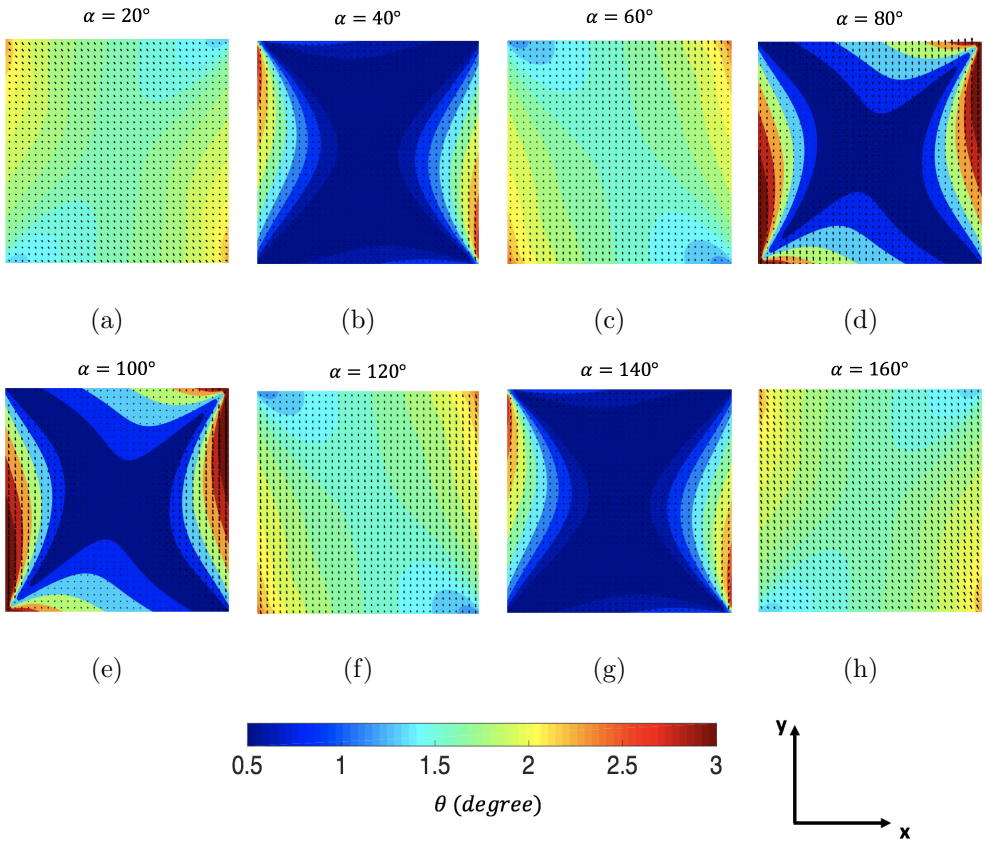

Figure 2.12. Lattice rotation of single grains after 10% compressive strain. The Rodrigues vector field $\boldsymbol{\lambda}$ is indicated on the contour plot. α indicates the rotation around the [110] direction.

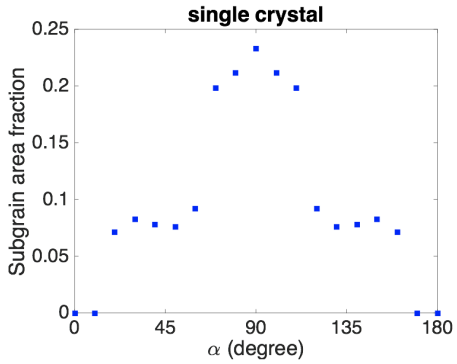

Figure 2.13. Subgrain area as a function of the rotation α along [110] direction.

ary is fixed in the vertical direction and the left boundary is fixed in the horizontal direction. A compressive displacement is applied to the right boundary with a strain rate $0.001s^{-1}$.

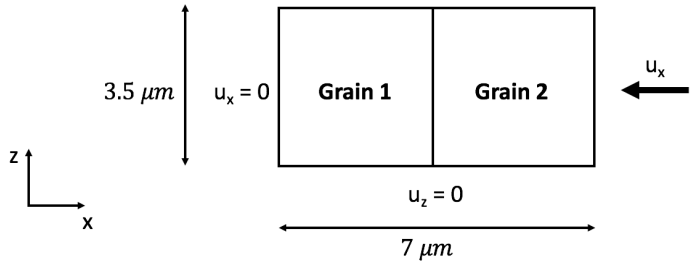

Figure 2.14. A schematic figure of bicrystal lattice rotation simulation.

In Figure 2.15, the orientations of the grains are assigned randomly. The contour plots show the rotation angles θ after applying 10% strain. From the figure, subgrain structures are likely to form at the region near the grain boundary.

To study the factors affecting the subgrain formation, misorientation of the grain boundary is calculated and the subgrain area fraction is plotted as a function as the misorientation. In Figure 2.16 (a), it is clear that as when the misorientation angle increases, the subgrain structure is more likely to form and its area is larger. However, a large grain misorientation does not necessarily lead to subgrain nucleation, which means that the formation of subgrains may also depend on other factors such as loading direction. Given the same misorientation, the mismatch between two crystals can be different due to the anisotropy of Sn. In general, there is a positive correlation between grain rotation and misorientation, and the effects of anisotropy should not be neglected. In Figure 2.16 (b), the distribution of the lattice rotation angles θ is ploted for applied strain 6%, 8% and 10%. The average rotation angles are indicated on the x axis as $\bar{\theta}_{6\%}$, $\bar{\theta}_{8\%}$ and $\bar{\theta}_{10\%}$, respectively. From the plot, when more deformation is applied, there is an increase in the average rotation angle as well as the subgrain area, which is defined as the region with more than 3° rotation.

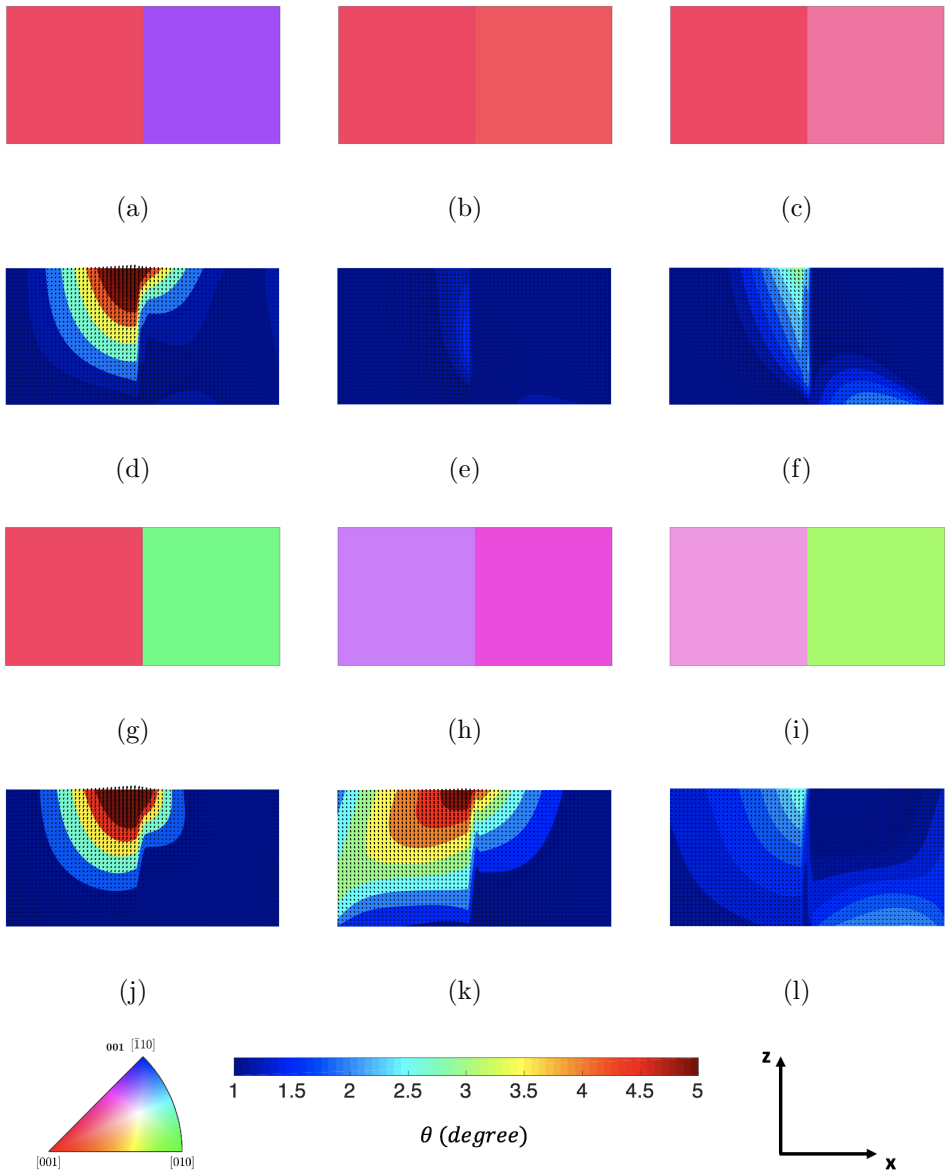

Figure 2.15. Bicrystal simulations. The inverse pole figure (IPF) coloring is used to represent the orientations. The Rodrigues vector field $\boldsymbol{\lambda}$ is indicated on the contour plots.

Figure 2.17 shows 3d bicrystal simulations. The grain size is 3.5 μm. The left boundary is fixed in x direction, the back boundary is fixed in y direction and the bottom boundary is fixed in z direction. A compressive displacement is applied to

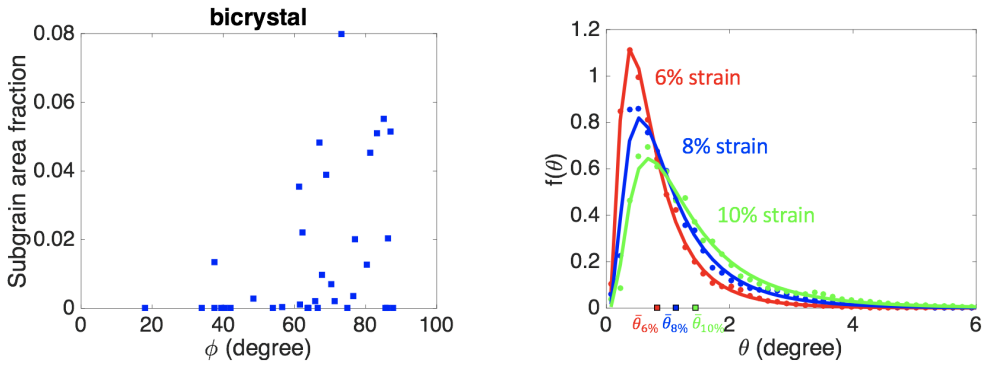

(a) (b)

Figure 2.16. 2D simulations. (a) Subgrain structure area vs misorientation at 10% applied strain. (b) Rotation angle distribution.

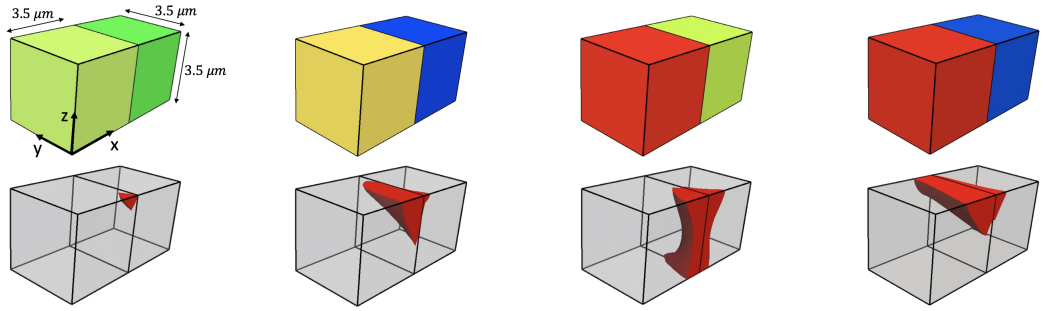

(a) (b) (c) (d)

Figure 2.17. 3D bicrystals simulations with subgrains (in red) formed after a 10% compressive strain is applied.

the right boundary with a strain rate $0.001s^{-1}$. The grain orientations are assigned randomly and represented by the IPF color.

In 3d simulations, the subgrain is defined as the region where the rotation angle is larger than 3° and is indicated in red. It is observed that the subgrains appear at the grain boundaries and near the free surfaces. In most cases, the nucleated subgrain structures have shallow boundaries and in some cases, they extend through the thickness of the thin film, see Figure 2.17 (c).

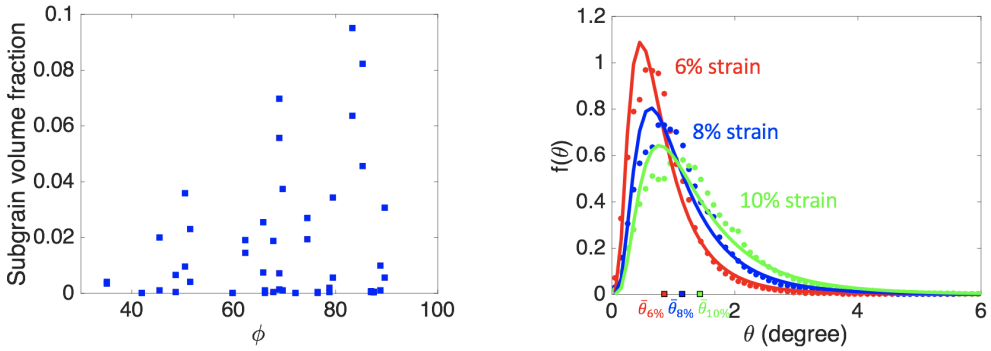

(a) (b)

Figure 2.18. 3D simulations. (a) Subgrain structure volume vs misorientation at 10% applied strain. (b) Rotation angle distribution.

In Figure 2.18 (a), the subgrain volume fraction is plotted as a function of grain boundary misorientation and the rotation angle distribution is plotted in (b). Comparing to Figure 2.16, similar conclusions can be drawn and the positive correlation between grain rotation and grain boundary misorientation can be extended from 2d to 3d.

2.3.5 Polycrystal simulations

Figure 2.19 is a schematic figure of 3d polycrystal simulation. The simulation domain is $15\mu m * 15\mu m * 3\mu m$ with 25 grains. The average grain size is around $3.5\mu m$. The random grain orientations are assigned to each grain. The bottom boundary is fixed in the vertical direction, the left boundary is fixed in the horizontal direction and the back boundary is fixed in the out-of-plane direction. A compressive displacement is applied with a strain rate $0.001s^{-1}$ at the right boundary.

Figures 2.20 (a-d) show the top view of the thin film with random grain orientations indicated by the IPF colors. Subgrains start forming when the applied strain reaches approximately 3%. The subgrains are depicted in red in Figures 2.20 (e-h) when the thin film is strained by 10%. In all the cases, subgrains form close to grain

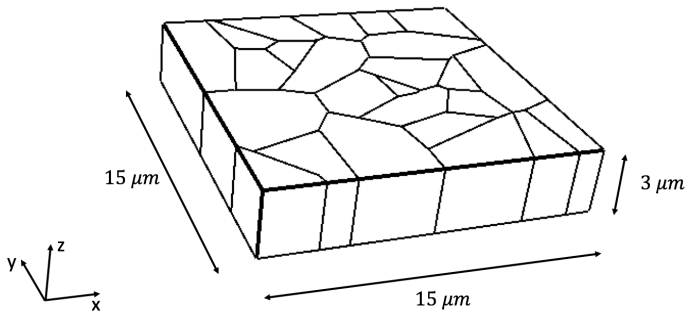

Figure 2.19. Geometry used in polycrystal simulations.

boundaries. However, not all grains contain newly formed subgrain structures. The different initial grain orientations in Figures 2.20 (a-d) affect the location and size of subgrains in Figures 2.20 (e-h).

The density of GND can be calculated directly from the gradients of the slip strains. In particular, the density of edge and screw dislocations can be estimated as:

$$\rho_{edge} = \sum_{\alpha=1}^{N} \mid \frac{1}{b^{\alpha}} \boldsymbol{s}^{\alpha} \cdot \nabla \gamma^{\alpha} \mid \quad \text{and} \quad \rho_{screw} = \sum_{\alpha=1}^{N} \mid \frac{1}{b^{\alpha}} \boldsymbol{l}^{\alpha} \cdot \nabla \gamma^{\alpha} \mid \tag{2.28}$$

where $\boldsymbol{l}^{\alpha} = \boldsymbol{m}^{\alpha} \times \boldsymbol{s}^{\alpha}$ and b^{α} is the length of the Burgers vector in the slip plane α. In Figures 2.20 (i-l) the density of edge GND and (m-p) screw GND are plotted after the film is strained by 10%. Because edge dislocations are related to tilt boundaries, larger densities of edge dislocations are observed in regions where subgrains is formed due to lattice rotation.

Figure 2.21 contains 3D views of the evolution of subgrains structures obtained in the simulations using the orientations presented in Figure 2.20(c). When the film is strained by 6% new subgrains form on the top surface close to grain boundaries. As more strain is applied the subgrain structures grow and new ones are nucleated.

To compare with the experiments conducted by Pei *et al.* [58], a domain with the grains oriented with the [001] and [010] directions perpendicular to the thin film surface is generated, see Figure 2.22 (a). Unfortunately, the other orientation information is not reported by the authors and therefore, Euler angles $[0, 0, 0]$ and

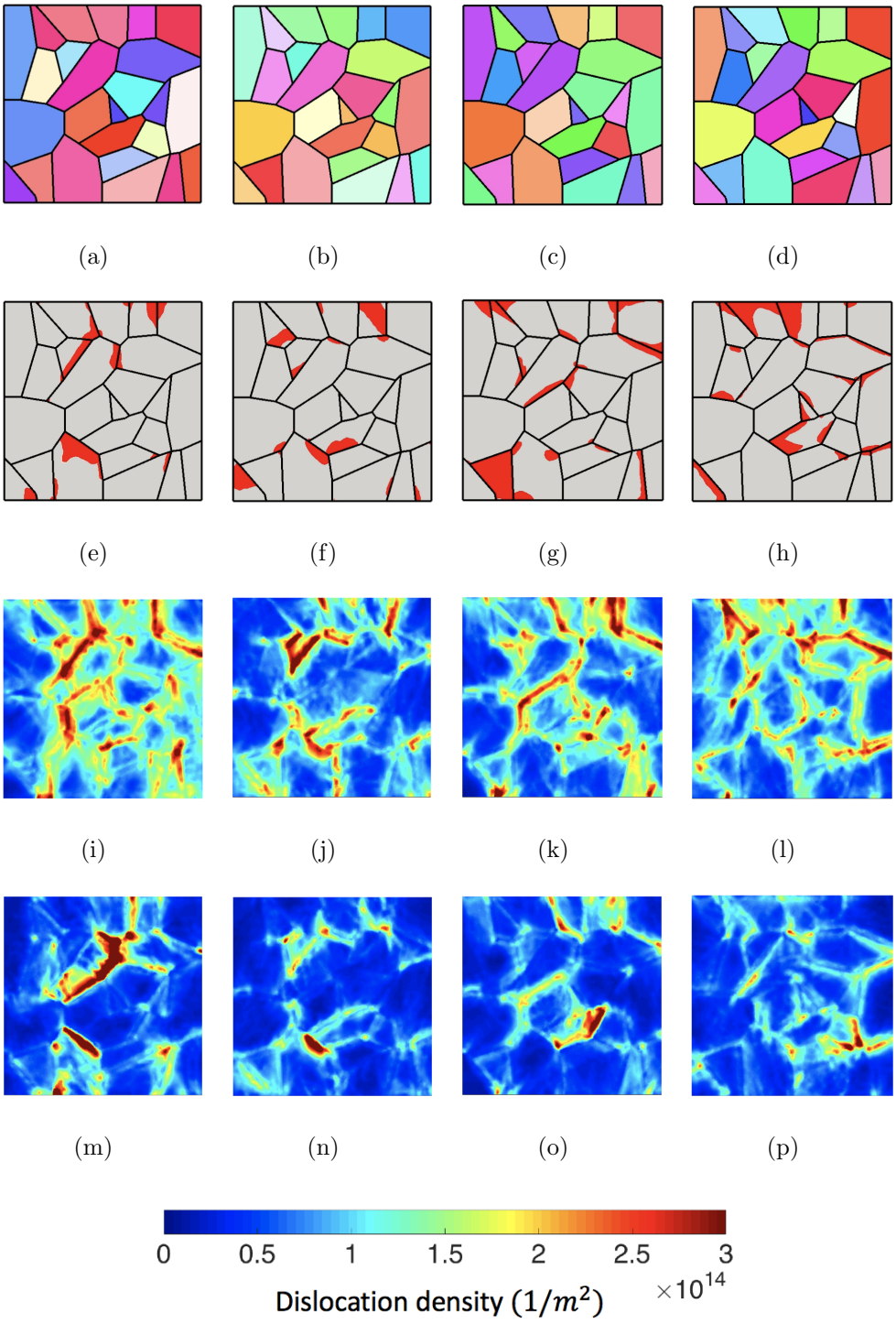

Figure 2.20. Top view of Sn thin films. (a-d) Grain orientations are represented by the IPF color. (e-h) Subgrains (in red) formed after 10% strain is applied. (i-l) Edge dislocation density and (m-p) screw dislocation density at the surface.

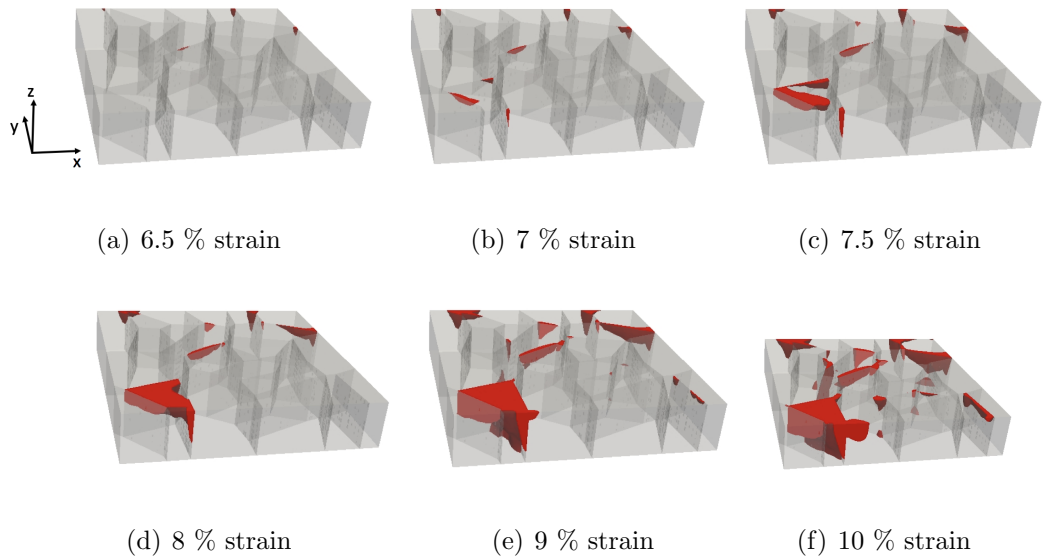

(a) 6.5 % strain (b) 7 % strain (c) 7.5 % strain

(d) 8 % strain (e) 9 % strain (f) 10 % strain

Figure 2.21. Process of subgrain structure formation with increasing strain.

$[90°, 90°, 0]$ are assigned to the grains in the simulation. For comparison, another microstructure, shown in Figure 2.22 (d), with grain orientations near [001] and [010] was also simulated.

In agreement with the experimental results, most subgrains form in the [001] oriented grains in regions neighboring [010] grains. However, some of these subgrains are not shallow and extend through the thickness of the thin film, as shown in Figures 2.22 (b-c). The subgrains are less columnar when the orientations are slightly different in Figures 2.22 (e-f). It is important to notice that the amount of strain in the simulations is much larger that the one in the experiments. Furthermore, other relaxation mechanisms, such as whisker growth and grain boundary sliding, that may reduce the stress and stop the growth of subgrains are not included in the simulations.

To understand a possible correlation between subgrain structures and grain orientation, contour plots of the edge and screw dislocation densities, components of the elastic strain, and the strain energy density are presented in Figure 2.23. In agreement with the results in Figure 2.20, there is a strong correlation between the

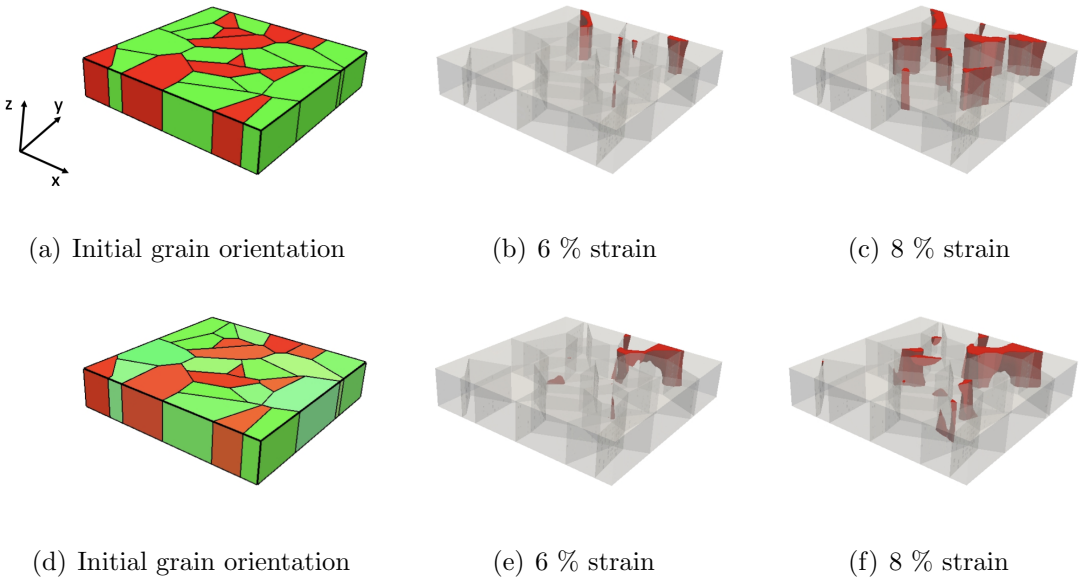

(a) Initial grain orientation (b) 6 % strain (c) 8 % strain

(d) Initial grain orientation (e) 6 % strain (f) 8 % strain

Figure 2.22. Evolution of the subgrain structures in Sn thin films with grains oriented in the [001] and [010] directions (a-c) and near [001] and [010] directions (d-f).

location of subgrains and edge dislocation density at the surface of the thin film in Figures 2.23 (b) and (c).

During loading, the thin film is compressed in the x direction and expands in the y and z directions. For [001] oriented grains the in plane elastic tensor components are $C_{11} = C_{22} = 72.3$ GPa. When the grain is oriented with the [010] direction perpendicular to the surface, the the elastic strain tensor component in the x direction is $C_{33} = 88.4$ GPa, see Table 2.2. Therefore, grains oriented in the [001] direction have larger in plane strain components (E^e_{xx} and E^e_{yy}) than grains oriented in the [010] direction. The strain energy density is also larger for [001] grains, see Figures 2.23 (e), (f), and (h). Due to the anisotropy of the elastic constants the shear strain component E^e_{xy}, presented in Figure 2.23 (g) is larger in the grain boundaries that are shared by [010] and [001] oriented grains. The other strain components, not shown in Figure 2.23 remain almost homogeneous in all the grains.

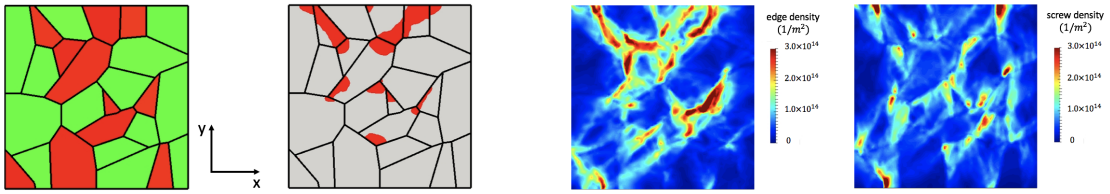

(a) Initial grain orientation (b) Subgrain structures (c) Edge dislocation density (d) Screw dislocation density

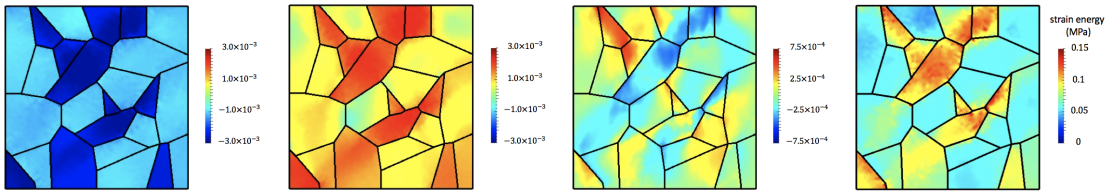

(e) E^e_{xx} (f) E^e_{yy} (g) E^e_{xy} (h) Strain energy density

Figure 2.23. Top view of Sn thin films with grains oriented in [001] and [010] directions. (a) Initial grain orientation, (b) subgrain structures (in red) after 10% strain in the x direction, (c) edge dislocation density, (d) screw dislocation density, (e) E^e_{xx}, (f)E^e_{yy}, (g) E^e_{xy} and (h) strain energy.

In agreement with the results in Figure 2.20, there is a strong correlation between the location of the subgrains and high edge dislocation density. It can also bee seen in Figure 2.23 (g) that larger values of in plane shear strain appear in the same regions.

2.4 Summary

It is accepted that whiskers growth is a process of atom diffusion driven by the stress gradients in the film [7,23,24,59]. However, it is not clear under what conditions whisker grain will nucleate and how it nucleate under mechanical loading. Cross sectional measurements of the microstructure usually show shallow grains at the root of the whiskers [7, 23, 60]. Based upon this observation, two possible mechanisms for

nucleation of surface grains are investigated using finite element simulations: grain boundary migration and subgrain formation by lattice rotation.

In the simulations shown in Figure 2.9 and Figure 2.9, the stress needed to move the grain boundary and form a shallow grain by boundary migration is 2 to 3 orders of magnitude larger than the stress observed in Sn thin films in the experiments. Previous efforts arrived to the same conclusion using a nucleation model [7]. Therefore, the grain boundary migration is not the main mechanism by which shallow grains form in Sn films.

Under deformation, the anisotropy of Sn results in highly localized strain in the regions near grain boundaries in the polyscrstals. The dislocations generated and accumulated in these regions subdivide the grains into subgrains by rotating the lattice with respect to the original grain [55, 56, 61]. To take into account of all these deformation mechanisms, a finite element model that included finite deformation and elasto-plastic anisotropy is used to simulate the mechanical responses of polycrystalline thin films, including the formation of subgrains due to lattice rotation. The new subgrains are identified as regions where the lattice rotation is larger than 3°.

Grain geometry in Figure 2.19 is generated and various textures are created by assigning random initial grain orientations. In all the simulations, subgrains form close to the surface of the thin film. A special case in which most grains are oriented in the directions [001] and [010] normal to the film surface shows subgrain nucleation in the grains oriented in the [001] direction which is in agreement with the experiments [58]. However, the subgrains extend through the thickness of the film. Small variations of the [001] and [010] orientations render more shallow grains. It is important to notice that other stress relaxation mechanisms, such as grain boundary sliding and whisker growth, that would prevent further growth of the subgrains are not included in the current simulations.

The only correlation with texture is that subgrains form in grains oriented such that their in plane strain components and consequently their strain energy density are larger in agreement with previous results [62]. It is clear that lattice rotation is

the result of the large elasto-plastic anisotropy of Sn and its relatively low yield stress. This phenomenon may be exacerbated at temperatures above room temperature with a more pronounced plastic deformation due to the reduction of the yield stress and the large anisotropy of the thermal expansion coefficients of Sn. In summary, these simulations show that lattice rotation induced by deformation may be an important contributing mechanism to nucleate shallow grains in Sn thin films that could become potential sites for whisker growth.

3. RELIABILITY STUDY OF SAC SOLDERS

3.1 Introduction

In electronic industry, the packaging technology has been significantly developed. In recent years, the demand for the miniaturization of electronics generates big concerns on the safety of the package. The reliability and the performance of the package is greatly dependent on the interconnecting materials. For environmental concerns, the usage of Pb-free solders emphasize the importance on the interfaical reactions and metallurgical evolution in the solder system. The most widely used solder system is SAC (Sn-Ag-Cu), while the employment of other metals such as Ni, Au also influence component metallizations and the solder performance [63]. The study of the Cu/Sn alloy system focused on the IMC formation and growth during the solder operation. The interfacial reaction between Cu and Sn under operational temperature results in two types of IMCs: Cu_6Sn_5 (η) and Cu_3Sn (ϵ). It is reported from various experimental studies that the failure of the solder joints is mostly dominated by the IMC layers [64–67] and yet the finite element simulations conducted so far are not able to model the IMC morphology and the voids inside. The objectives of this chapter is to provide a more accurate model to depict the fracture behavior and predict the strength of the solder joints.

3.1.1 Fracture of IMC

Experiments by Wang *et al.* [68] showed that the formation of Cu_6Sn_5 and Cu_3Sn layers at the interface between Cu and Sn and following growth of Cu_3Sn at the expense of Cu_6Sn_5. Tu *et al.* and Liu *et al.* [69, 70] studied the morphology and the orientation of Cu_6Sn_5 phase after thermal reflow process. The SEM and EBSD results showed that Cu_6Sn_5 grains are scalloped shaped and each 'scallop' is a single crystal.

Cu_3Sn grains are usually long and thin and columnar shaped [68]. The Cu_3Sn grain width is much smaller than the Cu_6Sn_5 grains.

In a solder joint, Sn and Cu are ductile while the interface IMCs are brittle. In the literature, the fracture property of Cu_6Sn_5 and Cu_3Sn are well studied and the fracture toughness for the bulk and thin film are reported [71]. Extensive experiments are performed to study the fracture behavior in the solder balls. Lee *et al.* [72] performed ball pull and ball shear tests in a series of solder balls and studied the failure modes on the fracture surfaces. The results showed that in Cu/Sn solders the only failure mode was brittle fracture which happened in the IMC layers. This observation agreed with the tensile experiments by Dutta *et al.* [73] that the cracks propagated through the IMCs. The later experiments [64, 74] found that the fracture location was dependent on the thickness of the IMC layers. When the Cu_3Sn layer is thin, the fracture takes place at the interface between the Cu_3Sn and the Cu_6Sn_5 layers. As the Cu_3Sn layer becomes thicker, the intergranular fracture of the Cu_3Sn layer begins to be dominant.

The effects of the IMC thickness also include the solder strength. In the experiments by Zhang *et al.* [66], the fracture strength of the solders was plotted as a function of the IMC thickness. At low stran rates, the fracture strength dropped from 110 MPa to 40 MPa as the IMC grew from 2 μm thick to 11 μm thick. Qin *et al.* [67] performed thermal aging experiment and results showed the thickness of IMC increased and the strength of the solder decreased during the aging.

Finite element simulations were performed to model the fracture process in the solders balls [73, 75, 76]. However, the modeling scale of these FEM simulations is too large to resolve for the IMC morphology and microstructure, and thus they not able to capture the detailed fracture behavior. In this chapter, the fracture behavior of Cu/Sn solder is studied in detail using a phase field damage model and simulations are presented to show the crack propagation process and the strength of the solder.

3.1.2 Void Nucleation Under Electromigration

In integrated circuit, the current density can reach up to 10^5 A/cm^2 [12] due the miniaturization of electronics. The shrinkage of size intensifies the problem of electromigration which is generally accepted as the main reason for void nucleation in the solder joints. The motion of the electron is caused by the direct electric current and can diffuse the atoms. The accumulating effect of the atom diffusion is the void formation and joint failure.

The electromigration experiments by Chang *et al.* [77,78] showed the void formation process in the solder bumps under current density ranging from 10^3 A/cm^2 to 10^4 A/cm^2. In the experiments by Ross *et al.* [79], the average void density ranged from 0 to 0.4 N/μm^2 and the average size ranged from 0 to 0.2 μm^2, depending upon the purity of the Cu substrate. The nucleated voids were observed mostly in the Cu_3Sn layer and near the interface between Cu_3Sn and Cu. Same observations were reported in Laurila *et al.* [63] and Luo *et al.* [80] when the materials were under thermal annealing and thermal aging.

In this work, the phase field damage model is applied to simulate the crack propagation with initial voids in the Cu/Sn system. The IMC morphology and microstructure are considered and effect of the IMC layer thickness are investigated.

3.2 Models

3.2.1 Plasticity model

When the solder bumps is under tensile or shear loading, the brittle IMCs tend to break while Cu and Sn exhibit plastic deformation. Sn is an anisotropic material with a body-centered tetragonal structure. The yield stress of Sn is dependent on its grain orientation, ranging from 40 MPa to 50 MPa [14,33,38]. In the following simulations, for simplicity the grain orientation of Sn is not considered and a perfect plasticity model is used with the yield stress 40 MPa. In the SAC solders, the oxygen-free-high

conductivity (OFHC) Cu is usually used for its excellent electrical conductivity and chemical purity. Here, the yield stress is taken to be 50 MPa [81, 82].

3.2.2 Damage Model

The phase field damage model is an approach describing the damage evolution by energy minimization in the system. The total energy in the material is consist of two part, the strain energy W_e and the fracture energy W_f:

$$W(\boldsymbol{\epsilon}, c) = W_e(\boldsymbol{\epsilon}, c) + W_f(c) \tag{3.1}$$

where $\boldsymbol{\epsilon}$ is the strain tensor and the variable c is a phase field damage parameter ranging from 0 to 1. $c = 0$ represents the undamaged material and $c = 1$ represents completely damaged material. Ω is the domain containing a crack.

According to Griffiths criterion, the fracture energy W_f is

$$W_f = \int_\Gamma G_c d\Gamma \tag{3.2}$$

where G_c is the surface energy for brittle materials and Γ represents the crack surface. In phase field method, the crack surface Γ can be approximated by diffuse delta function $\gamma(c)$ [3, 83, 84]:

$$d\Gamma(c, \nabla c) = \gamma(c, \nabla c) dV = \left(\frac{1}{2l_0} c^2 + \frac{l_0}{2} |\nabla c|^2 \right) dV \tag{3.3}$$

Here, l_0 is a length scale which defines the width of the damaged area [85–87]. Using the Equation 3.3, the fracture energy can be expressed as

$$W_f = \int_\Omega G_c \left(\frac{1}{2l_0} c^2 + \frac{l_0}{2} |\nabla c|^2 \right) dV \tag{3.4}$$

The strain energy in the domain is

$$W_e = \int_\Omega a(\boldsymbol{\epsilon}, c) dV \tag{3.5}$$

where $a(\boldsymbol{\epsilon}, c)$ is the strain energy density. In the damaged regions, the stiffness of the material is degraded and the strain energy density can be decomposed into two parts:

$$a(\boldsymbol{\epsilon}, c) = \left[(1 - c)^2 \right] a^+(\boldsymbol{\epsilon}) + a^-(\boldsymbol{\epsilon}) \tag{3.6}$$

where $a^+(\boldsymbol{\epsilon})$ is the part contributing to the damage and $a^-(\boldsymbol{\epsilon})$ is the part not affected by the damage.

For isotropic materials, one of the decomposition proposed [86, 87] for the strain energy density is:

$$a^+(\boldsymbol{\epsilon}) = \frac{\lambda}{2}\langle \mathrm{tr}(\boldsymbol{\epsilon})\rangle^2 + \mu \mathrm{tr}\left(\left(\boldsymbol{\epsilon}^+\right)^2\right) \tag{3.7}$$

$$a^-(\boldsymbol{\epsilon}) = \frac{\lambda}{2}\left(\mathrm{tr}(\boldsymbol{\epsilon}) - \langle \mathrm{tr}(\boldsymbol{\epsilon})\rangle\right)^2 + \mu \mathrm{tr}\left(\left(\boldsymbol{\epsilon}^-\right)^2\right) \tag{3.8}$$

where λ and μ are the Lamé constants and $\langle x\rangle$ is defined as

$$\langle x\rangle = \begin{cases} x & \text{for } x > 0 \\ 0 & \text{for } x \leq 0 \end{cases} \tag{3.9}$$

$\boldsymbol{\epsilon}^+$ and $\boldsymbol{\epsilon}^-$ are defined as

$$\boldsymbol{\epsilon}^+ = \begin{bmatrix} \langle \epsilon_1\rangle & 0 & 0 \\ 0 & \langle \epsilon_2\rangle & 0 \\ 0 & 0 & \langle \epsilon_3\rangle \end{bmatrix} \tag{3.10}$$

and

$$\boldsymbol{\epsilon}^- = \begin{bmatrix} \epsilon_1 - \langle \epsilon_1\rangle & 0 & 0 \\ 0 & \epsilon_2 - \langle \epsilon_2\rangle & 0 \\ 0 & 0 & \epsilon_3 - \langle \epsilon_3\rangle \end{bmatrix} \tag{3.11}$$

where ϵ_1, ϵ_2 and ϵ_3 are principal strains. Equation 3.6 to Equation 3.11 ensure that damage only evolve due to the positive principal strains or simple shearing. The rate of the fracture dissipation needs to be positive to guarantee that damage is irreversible:

$$\dot{W}_f = \int_\Omega G_c \dot{\gamma}(c, \nabla c) dV = \int_\Omega G_c \delta_c \gamma \cdot \dot{c} dV \ \geq 0 \tag{3.12}$$

This leads to the conditions $\delta_c\gamma \geq 0$ and $\dot{c} \geq 0$, where $\delta_c\gamma = \partial_c\gamma - \nabla \cdot \partial_{\nabla c}\gamma$ is the functional derivative.

To couple the damage field and the deformation field, a Lagrangian is defined as:

$$L\left(\dot{\boldsymbol{u}}, \boldsymbol{\epsilon}, c\right) = K\left(\dot{\boldsymbol{u}}\right) - W_e\left(\boldsymbol{\epsilon}, c\right) - W_f(c) \tag{3.13}$$

where $K\left(\dot{\boldsymbol{u}}\right)$ is the kinetic energy:

$$K\left(\dot{\boldsymbol{u}}\right) = \int_\Omega \frac{1}{2}\rho |\dot{\boldsymbol{u}}|^2 dV \tag{3.14}$$

Here, ρ is the material density and $\dot{\boldsymbol{u}}$ is the velocity vector. The Euler-Lagrange

$$-\frac{\partial W_e\left(\boldsymbol{\epsilon}, c\right)}{\partial \boldsymbol{u}}=\frac{d}{dt}\frac{\partial K\left(\dot{\boldsymbol{u}}\right)}{\partial \dot{\boldsymbol{u}}} \tag{3.15}$$

leads to the conservation of momentum:

$$\nabla \cdot \boldsymbol{\sigma}=\rho\frac{\partial^2 \boldsymbol{u}}{\partial^2 t} \tag{3.16}$$

where the stress tensor $\boldsymbol{\sigma}$ is calculated from the strain energy density:

$$\boldsymbol{\sigma}=\frac{\partial a\left(\boldsymbol{\epsilon}, c\right)}{\partial \boldsymbol{\epsilon}}=\left[(1-c)^2\right]\frac{\partial a^{+}\left(\boldsymbol{\epsilon}\right)}{\partial \boldsymbol{\epsilon}}+\frac{\partial a^{-}\left(\boldsymbol{\epsilon}\right)}{\partial \boldsymbol{\epsilon}} \tag{3.17}$$

For the damage field, the Euler-Lagrange equation is as follows

$$-\frac{\partial W_e\left(\boldsymbol{\epsilon}, c\right)}{\partial c}-\frac{\partial W_f\left(c\right)}{\partial c}=0 \tag{3.18}$$

Equation 3.4 - 3.8, together with Equation 3.18 can lead to

$$2(1-c)a^{+}\left(\boldsymbol{\epsilon}\right)=G_c\left(\frac{c}{l_0}-l_0\Delta c\right) \tag{3.19}$$

A time-dependent form of Equation 3.19 is used here for the damage evolution [88]:

$$\dot{c}=\frac{1}{\eta}\left\langle l_0\Delta c+2(1-c)\frac{\partial a^{+}\left(\boldsymbol{\epsilon}\right)}{G_c}-\frac{c}{l_0}\right\rangle \tag{3.20}$$

where η controls the system relaxation.

Equation 3.16 and Equation 3.20 are implemented and solved numerically in a finite element software MOOSE (Multiphysics Object-Oriented Simulation Environment) [28]. All the following simulations are carried out using MOOSE framework.

3.3 Results

The extensive experiments have found that the fracture of the Cu/Sn solder joints is dominated by the interface fracture. [64, 65, 72, 73, 89]. In this section, the fracture behavior in the Cu/Sn interface is modeled to study the effect of the IMC thickness on the solder strength.

3.3.1 Elastic simulations

2D finite element simulations are performed under plane strain condition. Figure 3.1 shows the geometry of the simulation domain and the boundary conditions. The left and the right boundary are fixed in the x direction and the bottom is fixed in the y direction. A tensile loading is applied in the y direction on the top. The domain contains four phases including Cu, Cu_3Sn, Cu_6Sn_5 and Sn. Each phase is represented by a different color. In Figure 3.1 (a), the thickness of Cu_3Sn layer is 2 μm with waviness of 0.5 μm and in (b), the thickness is 5 μm with the same waviness.

The domain size is 20 μm$*$15 μm.The element size is 0.1 μm is the interface between Cu_3Sn and Cu_6Sn_5 layers and 0.15 μm elsewhere. The total element number in the two geometries are 32414 and 35228, respectively. The length scale parameter l_0 is chosen to be 0.6 μm, which is 4 times the element size in the IMCs.

The material properties used in the simulations are list in Table 3.1. All the materials are assumed to be isotropic and elastic. The plasticity of Cu and Sn are not included here. The surface energy G_c is calculated from the fracture toughness K_{IC} reported in the literature [90–92] using the relation $G_c = K_{IC}^2/E'$ where $E' = E$ for plane stress condition and $E' = E/(1-v^2)$ for plane strain condition [83]. The fracture toughness in the interface is within the range 2 J/m^2 to 20 J/m^2 according to the reference [89]. In the following simulations, the interface G_c is chosen to be 10 J/m^2 while the other properties used for the interface are the same as Cu_3Sn.

In many experiments [63, 79, 80], voids are observed in the Cu_3Sn layer due to the applied current or thermal processing. The average void density is reported within 0 to 0.4 N/μm^2 [79] and the equivalent diameter of most voids is around 0.2-0.4 μm [94]. The location of the nucleated voids is mostly in the Cu_3Sn layer and near the interface between Cu and Cu_3Sn. The existence of voids in brittle Cu_3Sn layer in general affects the damage nucleation and evolution. In the follosing simulations, three different void densities are assigned to the Cu_3Sn layer, 0.05 N/μm^2, 0.125

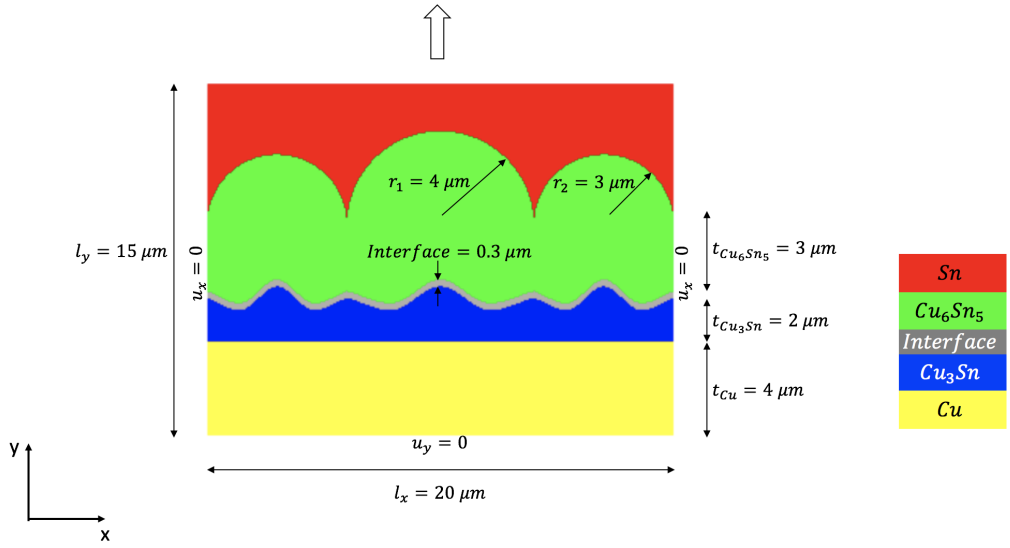

(a) Thin Cu_3Sn layer

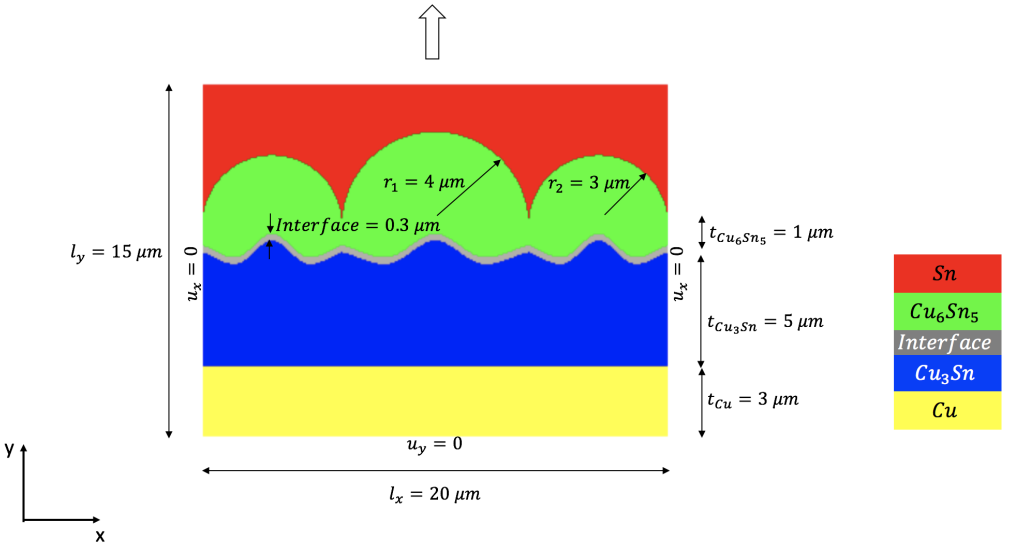

(b) Thick Cu_3Sn layer

Figure 3.1. Geometry of (a) thin Cu_3Sn layer and (b) thick Cu_3Sn layer.

N/μm^2 and 0.25 N/μm^2, to study the influence of initial void density. The average void size is 0.36*0.36 μm^2 for all cases

The void evolution at the Cu/Sn interface with thin Cu_3Sn layer is shown in Figure 3.2. When the initial void density is 0.05 N/μm^2, it is clear that the fracture starts

Table 3.1. Material properties used in the simulations. [71, 90–93]

	Young's modulus	Poissons ratio	Density	Surface energy
	E (GPa)	v	ρ (g/cm^3)	G_c (J/m^2)
Sn	50	0.36	7.3	4000
Cu_6Sn_5	96.9	0.309	8.45	19
IMC interface	123.2	0.319	9.14	10
Cu_3Sn	123.2	0.319	9.14	22
Cu	117	0.34	8.96	9000

at the interface between Cu_3Sn and Cu_6Sn_5 layers at 1% of applied strain. Then the entire interface is fractured. For larger void density, the initial voids first grow and coalesce with the neighbouring voids. As the increasing applied strain, the voids evolve into cracks and propagate along the interface, see Figure 3.3. The reason is that the interface is weaker than the IMCs due to the lower surface energy and it is easier for the interface to break. This result matches with the experimental results reported in Lee *et al.* [64] that the fracture happens near the interface between the two IMCs.

For thick Cu_3Sn layer, the void evolution follows the same trend for all three different void densities, as is shown in Figure 3.4. The crack grows along the voids which are mostly at the bottom of the Cu_3Sn layer and away from the interface. So the intergranular fracture within the Cu_3Sn layer dominates the failure pattern. Same result is observed in the experiments [64].

The effect of the Cu_3Sn thickness on the strength of the solders can be studied by the stress strain curves in Figure 3.5. For the same void density, fracture happens earlier at the solder joints with the thicker Cu_3Sn, i.e., for the void density 0.125 N/μm^2, in thick Cu_3Sn layer the critical stress for the fracture to start is around 0.6 GPa when the applied strain is around 0.6% while the critical stress in thin Cu_3Sn layer is almost 0.8 GPa with 0.8% applied strain. In the work by Qin *et al.* [67], it is

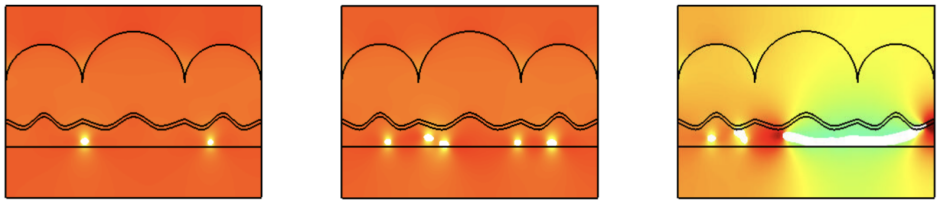

(a) 0.7% applied strain

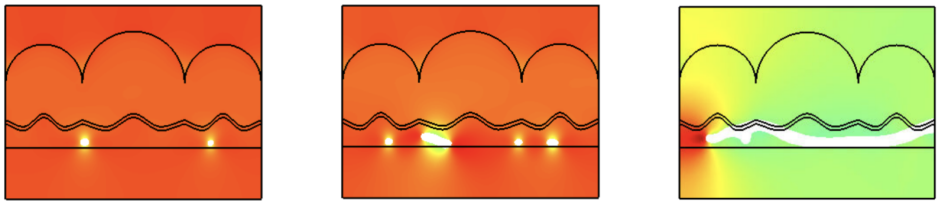

(b) 0.8% applied strain

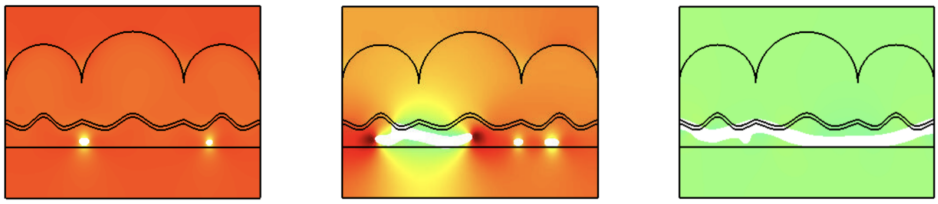

(c) 0.9% applied strain

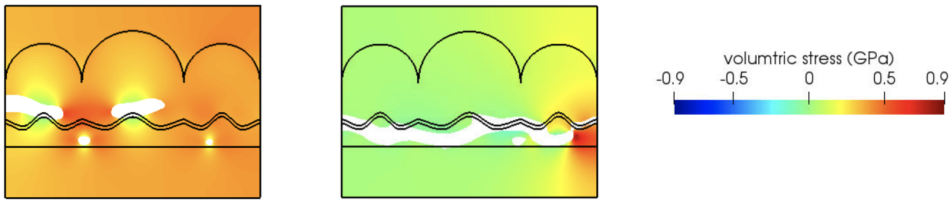

(d) 1.0% applied strain

Figure 3.2. Fracture evolution at the Cu/Sn interface with thin Cu_3Sn layer. The void densities are 0.05 N/μm^2, 0.125 N/μm^2 and 0.25 N/μm^2 from left to right, respectively.

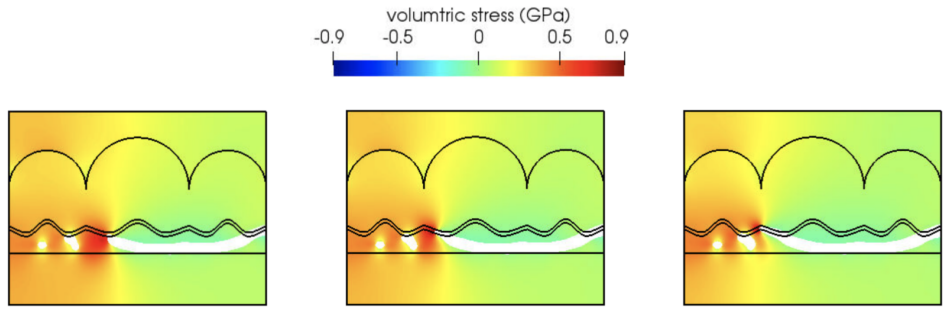

Figure 3.3. Crack evolution at the Cu/Sn interface with void density 0.25 N/μm^2.

reported that the thickness of IMCs increases during thermal aging while the tensile strength of the solder joints shows a decrease, which agrees with the simulation results. In addition to the IMC thickness, the thermal processing also contributes to the void nucleation [79, 80]. It is another reason why the longer thermal processing causes low strength. In the simulations, it is shown that the higher the void density, the easier for the solder to break, i.e., for thick Cu_3Sn layer, the critical stress to initiate fracture drops from 0.8 GPa to 0.4 GPa when the void density increases from 0.05 N/μm^2 to 0.25 N/μm^2. However, the stress observed in the experiments is one magnitude smaller than the stress shown in the simulations. The reason accounts for this large difference is that the plasticity of Sn and Cu is not included here. The simulations with plasticity are presented in the following.

3.3.2 Plastic simulations

The above simulation reuslts show the capacity of the phase field damage model. To further model the plasticity behavior of Cu and Sn, the perfect plasticity model described in 3.2 is used. The same geometries and boundary conditions shown in Figure 3.1 are used. The material properties are listed in Table 3.2.

The fracture evolution at Cu/Sn interface when Cu and Sn plasticity is coupled is presented in Figure 3.6 and Figure 3.7. Similar fracture behavior is observed as

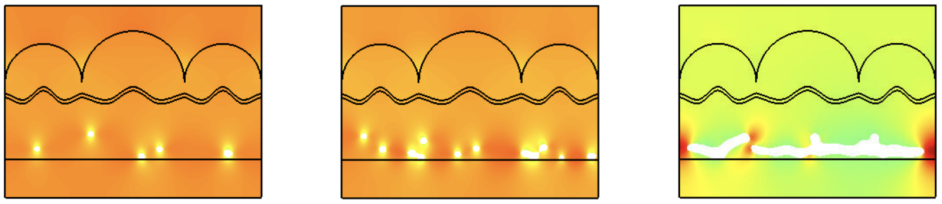

(a) 0.5% applied strain

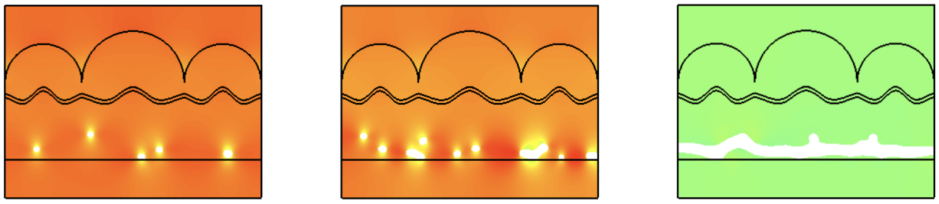

(b) 0.6% applied strain

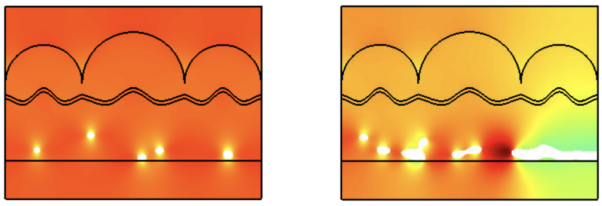

(c) 0.7% applied strain

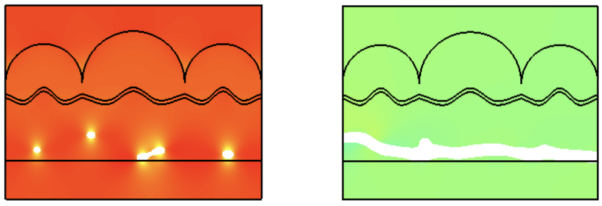

(d) 0.8% applied strain

(e) 1.0% applied strain

Figure 3.4. Fracture evolution at the Cu/Sn interface with thick Cu_3Sn layer. The void densities are 0.05 N/μm^2, 0.125 N/μm^2 and 0.25 N/μm^2 from left to right, respectively.

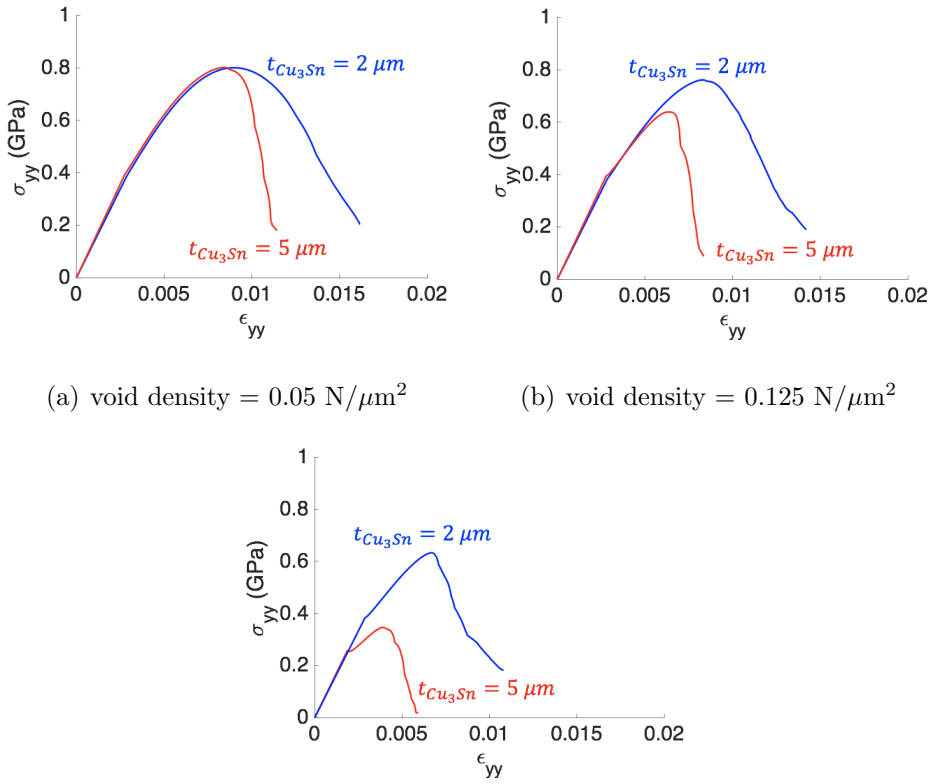

(a) void density = 0.05 N/μm^2

(b) void density = 0.125 N/μm^2

(c) void density = 0.25 N/μm^2

Figure 3.5. Stress strain curve comparison for different Cu_3Sn thickness.

Table 3.2. Material properties used in the simulations with plasticity. [14, 71, 81, 82, 90, 93]

	Young's modulus	Poissons ratio	Density	Yield Stress	Surface energy
	E (GPa)	ν	ρ (g/cm^3)	σ_Y (MPa)	G_c (J/m^2)
Sn	50	0.36	7.3	40	/
Cu_6Sn_5	96.9	0.309	8.45	/	19
IMC interface	123.2	0.319	9.14	/	10
Cu_3Sn	123.2	0.319	9.14	/	22
Cu	117	0.34	8.96	50	/

Figure 3.2 and Figure 3.4. When the Cu_3Sn layer is thin, the crack propagates along the IMC interface. In the simulations with thick Cu_3Sn layer, the damage initiates at the IMC interface when the void density is low while the damage grows from the initial voids when the void density is high. The fracture location shifts from the IMC interface to Cu_3Sn as the thickness of Cu_3Sn layer increases, which is the same as the experimental results in Zhang *et al.* [66].

The stress strain curves in Figure 3.8 show the effects on plasticity of Cu and Sn. When the plastic behavior is considered, the fracture stress decreases from about 800 MPa to about 25 MPa, which is the same magnitude as the experimental results [67]. For low void densities, the fracture stress is the same for two geometries because the fracture starts at the IMC interface, see Figure 3.8 (a) and (b). When the void density is high, a decrease of 4 MPa in fracture stress is observed in Figure 3.8 (c) for thicker Cu_3Sn layer.

3.3.3 Plastic simulations with Cu_3Sn grain boundary

While the above plastic simulations do provide a realistic prediction of fracture strength, the reason for the fracture location shift needs to be studied further. In the experiments by Lee *et al.* [64], TEM images show the structure evolution of the Cu_3Sn layer during the thermal aging, which may explains the shifting of fracture location. In Figure 3.9, two geometries are shown to capture Cu_3Sn grain morphology.

In the initial stage of thermal aging experiments on solders joints, large, micro-sized, scalloped shaped Cu_6Sn_5 grains are formed, followed by the nucleation of a layer of elongated Cu_3Sn grains, with grain width up to a few hundreds nm [64,68,70]. The cross sectional microstructure is represented in Figure 3.9 (a). This geometry contains 3 Cu_6Sn_5 grains and 24 Cu_3Sn grains with average grain width 0.8 μm. The thickness of Cu_3Sn layer is 2 μm with waviness of 0.5 μm.

During thermal aging, the thickness of the IMCs layer increases [66, 67]. In the experiments of Cu-Sn-Cu sandwhich-like samples, it is observed that Cu_3Sn layer

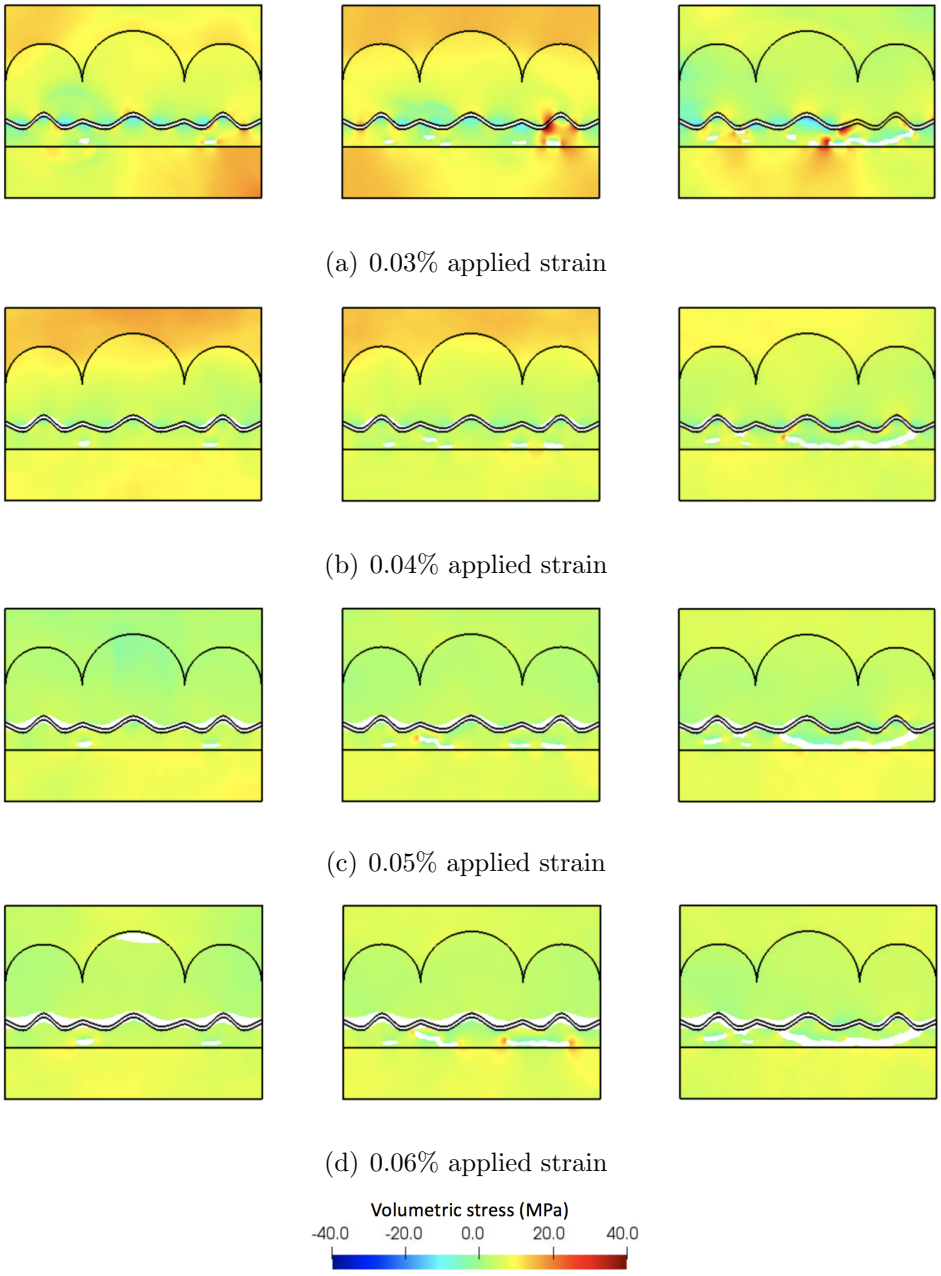

(a) 0.03% applied strain

(b) 0.04% applied strain

(c) 0.05% applied strain

(d) 0.06% applied strain

Figure 3.6. Fracture evolution at the Cu/Sn interface with thin Cu_3Sn layer. The void densities are 0.05 N/μm^2, 0.125 N/μm^2 and 0.25 N/μm^2 from left to right, respectively. The plasticity of Cu and Sn are coupled.

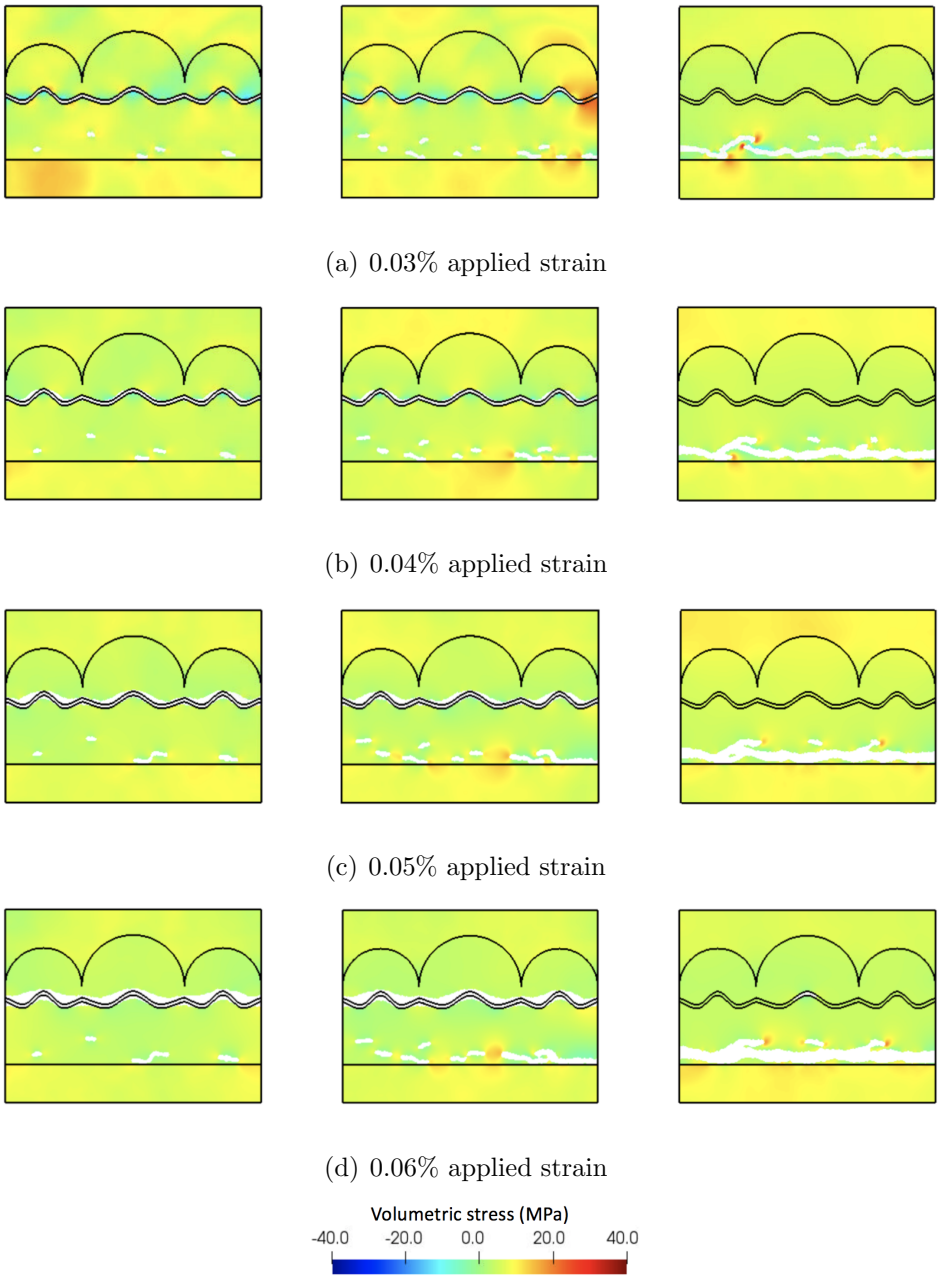

(a) 0.03% applied strain

(b) 0.04% applied strain

(c) 0.05% applied strain

(d) 0.06% applied strain

Figure 3.7. Fracture evolution at the Cu/Sn interface with thick Cu_3Sn layer. The void densities are 0.05 N/μm^2, 0.125 N/μm^2 and 0.25 N/μm^2 from left to right, respectively. The plasticity of Cu and Sn are coupled.

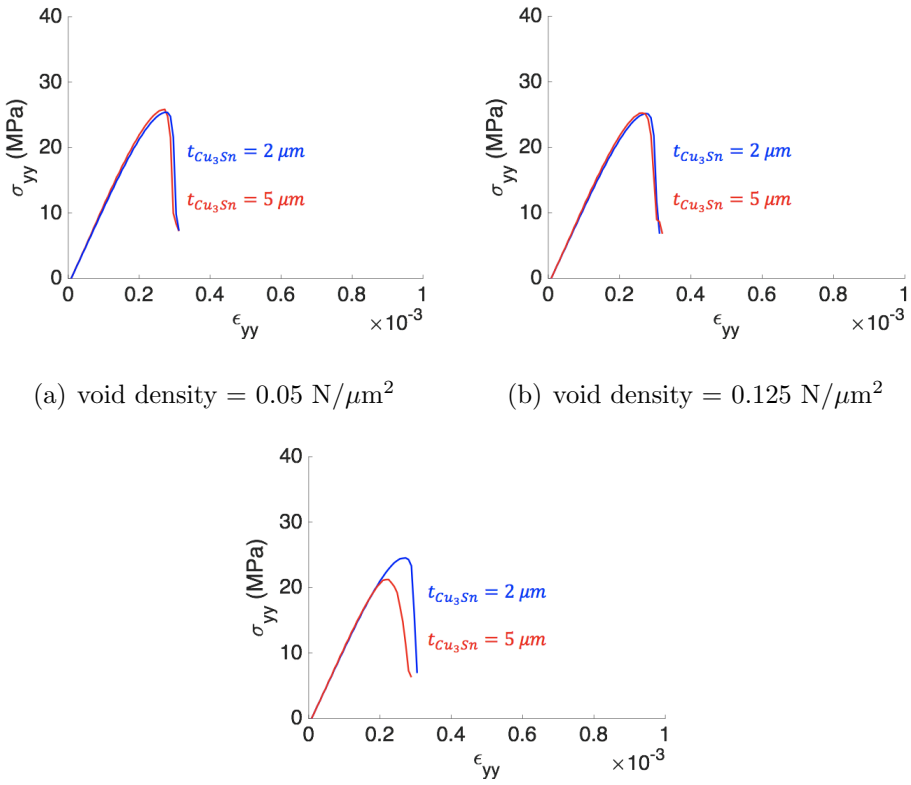

(a) void density = 0.05 N/μm^2

(b) void density = 0.125 N/μm^2

(c) void density = 0.25 N/μm^2

Figure 3.8. Stress strain curve comparison for different Cu_3Sn thickness. The plasticity of Cu and Sn are coupled.

grow at the expense of the previously formed Cu_6Sn_5 layer [64, 68, 69, 95–97]. The TEM images show that nucleation of new Cu_3Sn grains during the solid state thermal aging and the single-stack structure becomes a multi-stack structure [64, 98]. The geometry of the solders under longer thermal aging time is shown in Figure 3.9 (b). The thickness of Cu_3Sn layer is 5 μm with the same waviness and number of grains is 78.

In the geometries in Figure 3.9, the element size is 0.04 μm in Cu_3Sn grains, grain boundaries and the interface between Cu_3Sn and Cu_6Sn_5. The average element size is 0.14 μm in the Cu_6Sn_5 layer and 0.3 μm elsewhere. The total element number in the simulation geometries are 60404 and 122151, respectively. The length scale

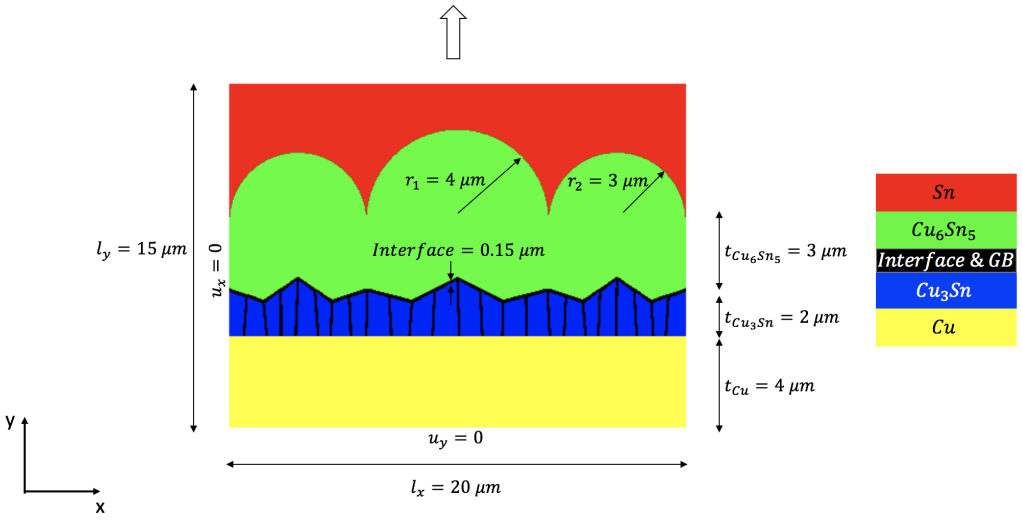

(a) Thin Cu_3Sn layer

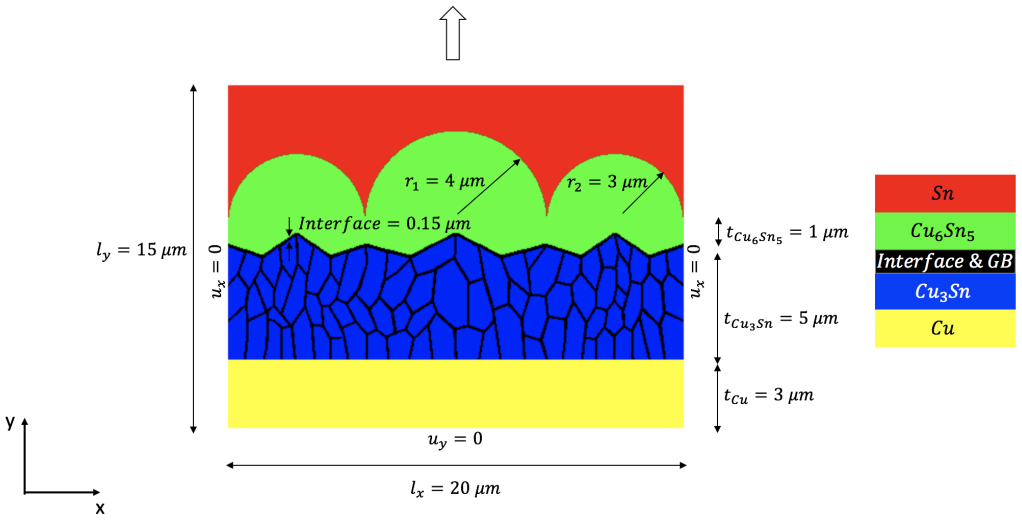

(b) Thick Cu_3Sn layer

Figure 3.9. Geometries with Cu_3Sn grain boundaries.

parameter l_0 is chosen to be 0.16 μm, which is 4 times the element size in Cu_3Sn grains and grain boundaries.

The material properties are listed in Table 3.3. The properties of Cu_3Sn grain boundary are the same as the Cu_3Sn grains except the surface energy is taken to be 5 J/m^2.

Table 3.3. Material properties used in the simulations with grain boundaries. [14, 71, 81, 82, 90, 93]

	Young's modulus	Poissons ratio	Density	Yield Stress	Surface energy
	E (GPa)	ν	ρ (g/cm^3)	σ_Y (MPa)	G_c (J/m^2)
Sn	50	0.36	7.3	40	/
Cu_6Sn_5	96.9	0.309	8.45	/	19
IMC interface	123.2	0.319	9.14	/	10
Cu_3Sn	123.2	0.319	9.14	/	30
Cu_3Sn grain boundary	123.2	0.319	9.14	/	5
Cu	117	0.34	8.96	50	/

Similar to the above simulations, three different initial void densities are used, 0.05 N/μm^2, 0.125 N/μm^2 and 0.25 N/μm^2. The simulation without initial voids are also studied. The average void size is 0.2*0.2 μm^2 for all cases and the distribution of the initial voids is shown in Figure 3.10.

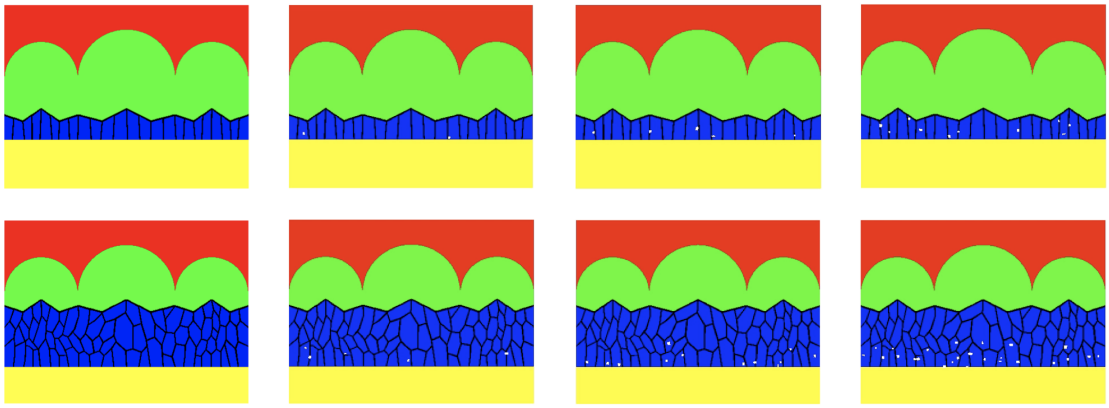

(a) no initial voids (b) void density 0.05 N/μm^2 (c) void density 0.125 N/μm^2 (d) void density 0.25 N/μm^2

Figure 3.10. Initial void distribution. The initial voids are indicated in white.

The crack evolution at the Cu/Sn interface with thin Cu_3Sn layer is shown in Figure 3.11 and the volumetric stress evolution is shown in Figure 3.12. When applying a tensile loading to the domain, the cracks first nucleate at the Cu_3Sn grain boundaries because the value of surface energy G_c in the grain boundary is half of the IMC interface. Since the Cu_3Sn layer is a single-stack structure with columnar grains, the grain boundary cracks grow vertically and extend into the IMC interface. As the applied strain is increased, the crack keeps propagating horizontally along the IMC interface and the entire domain breaks. In this case, the presence of Cu_3Sn grain boundaries does not have a significant influence the crack propagation comparing to Figure 3.6.

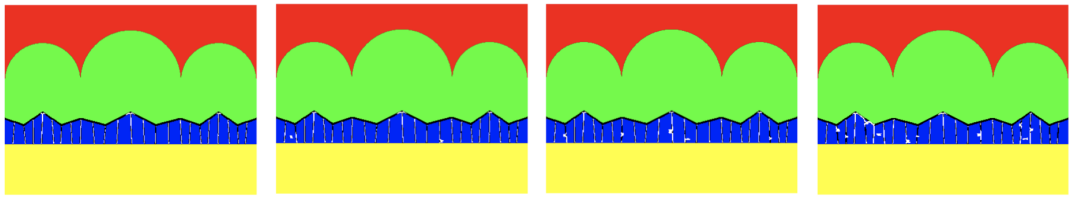

(a) 0.027% applied strain

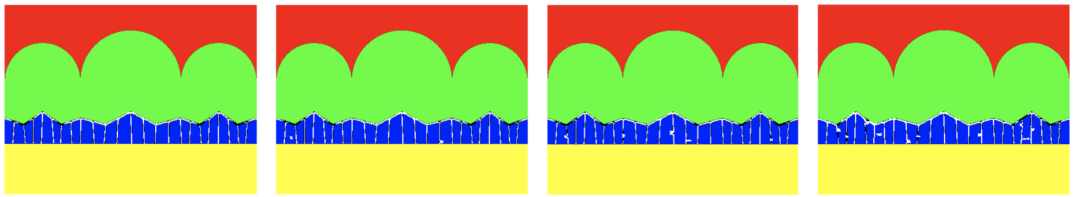

(b) 0.029% applied strain

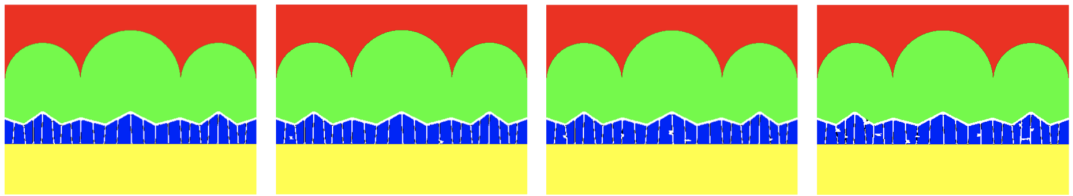

(c) 0.031% applied strain

Figure 3.11. Fracture evolution at the Cu/Sn interface. The Cu_3Sn layer is 2 μm. The void densities are 0, 0.05 N/μm^2, 0.125 N/μm^2 and 0.25 N/μm^2 from left to right, respectively.

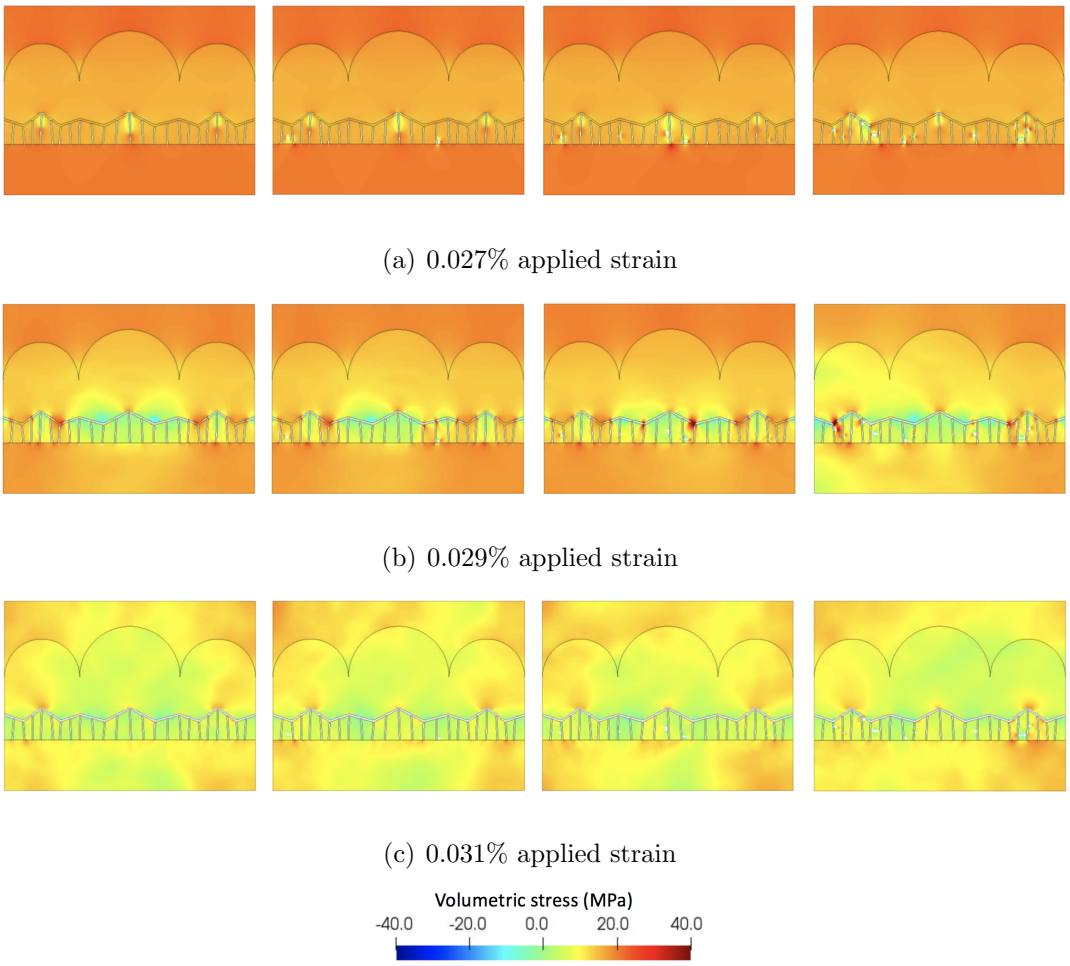

(a) 0.027% applied strain

(b) 0.029% applied strain

(c) 0.031% applied strain

Figure 3.12. Volumetric stress evolution at the Cu/Sn interface. The Cu_3Sn layer is 2 μm. The void densities are 0, 0.05 N/μm^2, 0.125 N/μm^2 and 0.25 N/μm^2 from left to right, respectively.

For the geometry with a thick Cu_3Sn layer, the crack evolution is shown in Figure 3.13 and the volumetric stress evolution is shown in Figure 3.14. Similar to Figure 3.11, the cracks also initiate at the grain boundaries. In this geometry, the Cu_3Sn layer is now a multi-stack structure with both vertical and horizontal grain boundaries. When under a tensile loading in the y direction, the cracks prefer to grow horizontally within the grain boundaries before extending to the IMC interface. Same result is reported in the literature [64] that intergranular fracture of Cu_3Sn grains is observed when the solder ball is under 1000 hour thermal aging and a thick Cu_3Sn layer is

formed. This results reveal the importance of Cu_3Sn grain structure on the fracture evolution in Cu/Sn solders.

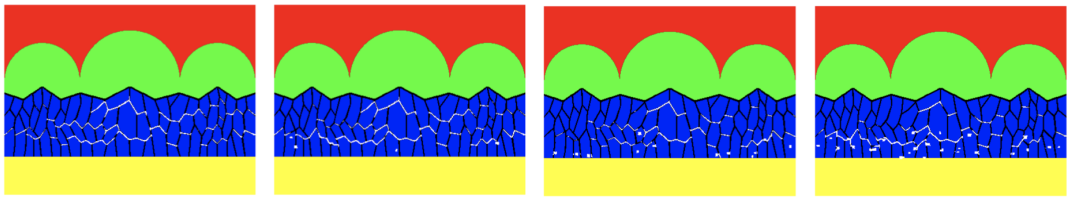

(a) 0.022% applied strain

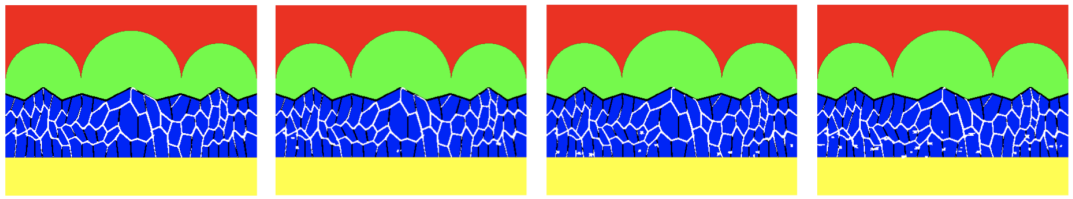

(b) 0.03% applied strain

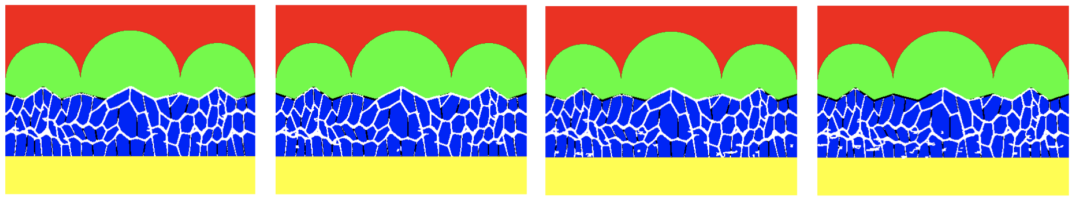

(c) 0.04% applied strain

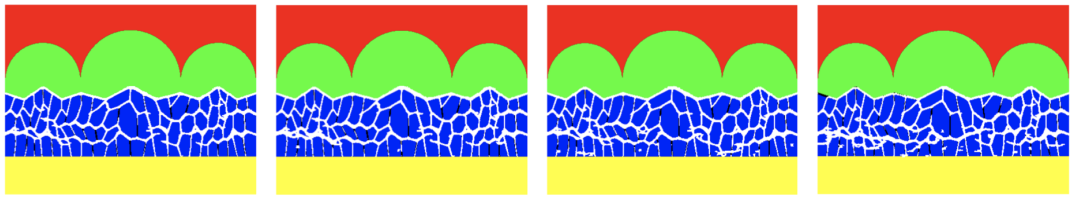

(d) 0.048% applied strain

Figure 3.13. Fracture evolution at the Cu/Sn interface. The Cu_3Sn layer is 5 μm. The void densities are 0, 0.05 N/μm^2, 0.125 N/μm^2 and 0.25 N/μm^2 from left to right, respectively.

The effect of the Cu_3Sn thickness on the strength of the solders can be studied by the stress strain curves in Figure 3.15. The stress strain curves are extracted from

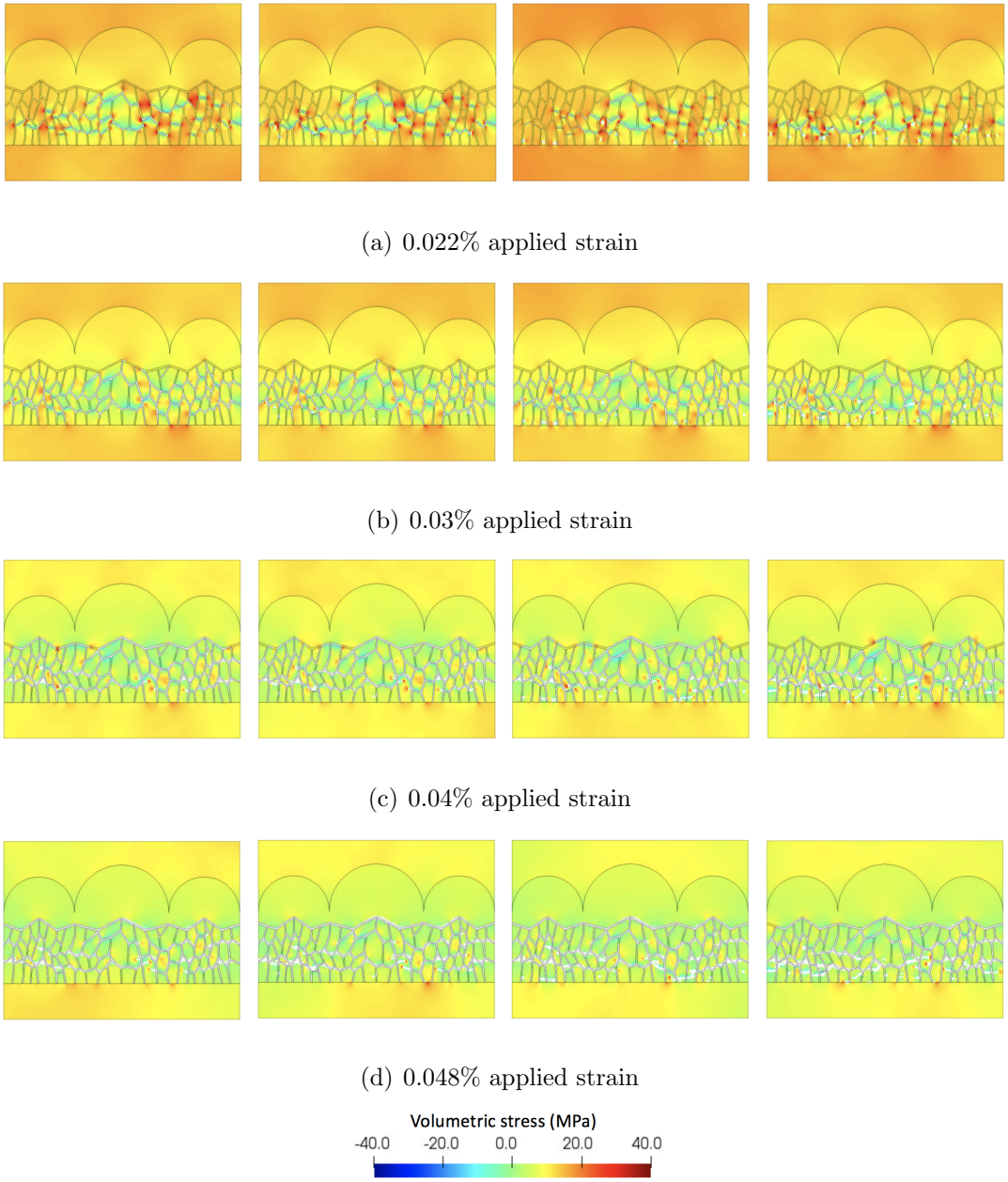

(a) 0.022% applied strain

(b) 0.03% applied strain

(c) 0.04% applied strain

(d) 0.048% applied strain

Figure 3.14. Volumetric stress evolution at the Cu/Sn interface. The Cu_3Sn layer is 5 μm. The void densities are 0, 0.05 N/μm^2, 0.125 N/μm^2 and 0.25 N/μm^2 from left to right, respectively.

the simulations without initial voids. The figure shows the fracture stress decreases with the thickness of the Cu_3Sn layer. The same trend is reported in many literatures [66, 67, 99]. The critical stress for the crack to nucleate is around 25 MPa and the reported fracture stress from the experiments is around 30-40 MPa [67]. The difference may due to the size of the simulation domain and texture of the IMCs.

Figure 3.16 presents the stress strain curves for the simulations with different initial void densities. In both cases, the void density doesn't appear to have a significant effect on the fracture behavior. This is due to the large value of surface energy G_c in the Cu_3Sn grains compared to the grain boundary and the IMC interface, which results in the nucleation and propagation of the cracks before growth of the initial voids.

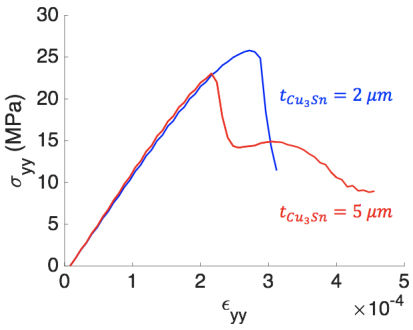

(a)

Figure 3.15. Stress strain curve comparison for different Cu_3Sn thickness.

3.4 Summary

The reliability of the Cu/Sn solders is studied in this chapter using the phase field damage model. The model is able to describe the fracture evolution in the material by energy minimization and the driving force for the fracture is the mechanical loading.

2D finite element simulations are performed under plane strain condition and the effects of IMC thickness and void density are investigated. Three different void

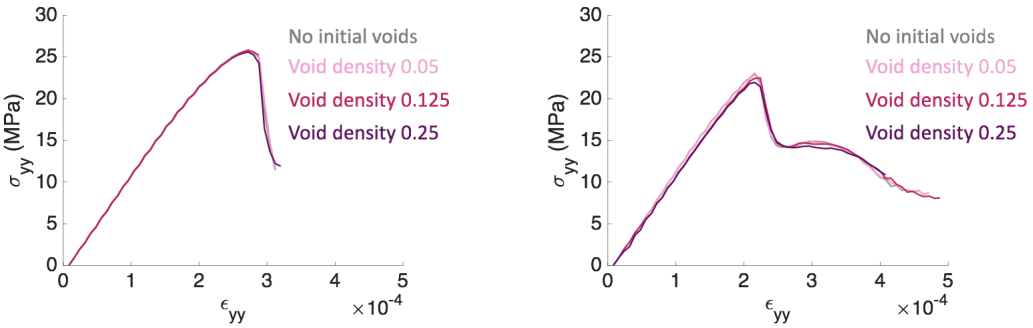

(a) Thin Cu_3Sn layer

(b) Thick Cu_3Sn layer

Figure 3.16. Stress strain curve comparison for different void densities.

densities are assigned in the simulations and the result show that solder joints with higher void density tend to have lower strength. The fracture occurs at different locations depending on the Cu_3Sn thickness. For thin Cu_3Sn layer, the fracture is observed at the interface between the two IMCs while for thick Cu_3Sn layer, the crack propagates along Cu_3Sn grain boundary. The increasing thickness of Cu_3Sn layer results in a decrease in the solder strength. These results agree with the experiments [64, 100].

In summary, the phase field damage model used in this chapter is able to predict the fracture behavior of the Cu/Sn solder joints. The reliability and the performance of the solders can be improved by restricting the growth of the IMCs and the nucleation of the voids.

4. STACKING FAULT STRENGTHENING OF ALLOYS

Note part of this chapter is reproduced from "Effects of the Stacking Fault Energy Fluctuations on the Strengthening of Alloys"in Acta Materialia, 164, pp. 1-11 [101].

4.1 Introduction

Predictive models of flow, strengthening, ductility, fatigue, and other macroscopic quantities are fundamental to advance the design of alloys by selecting the composition required to achieve a specific purpose. Therefore, it is of key importance to understand how lattice distortion, elastic modulus misfit, and stacking fault or chemical misfit contribute to strengthening of alloys. There are multiple theories [102–105] and simulations [106–109] for alloys and super alloys that focus on strengthening due to impenetrable solutes. The theoretical work of Hirch and Kelly [110], on the other hand, focuses on the strengthening of alloys due to the presence of solutes with lower stacking fault energy.

High entropy alloys (HEAs) are solid-solution alloys with five or more combined elements in nearly equiatomic concentrations. The name derives from the concept that entropy of mixing is responsible for stabilizing the phases in a many components system. Other names are also used for these alloys, including, multicomponent concentrated solid solution alloy and multi-principal element alloy [111]. These materials exhibit superior functional properties, including thermal, electric, corrosion and oxidation resistance as well as improved mechanical properties. For example, at room temperature, the yield strength for the BCC $AlCoCrFeNiTi_x$ alloy system is about 3 GPa and in a temperature ranging from 4.2 K to 300 K, $Al_{0.5}CoCrCuFeNi$ can reach 30% plastic strain [112–116]. Most models and simulations of HEAs focus on

the effects of lattice distortion, but there are recent approaches that also include the chemical misfit [107, 116–119].

Molecular dynamics simulations of the FCC HEA $Co_{30}Fe_{16.67}Ni_{36.67}Ti_{16.67}$ by Rao *et al.* [120] show that the value of the stacking fault energy depends locally on the composition and it is lower than that in pure FCC materials. The structure of edge and screw $a/2\langle 110\rangle$ dislocations obtained in these simulations shows variations of the stacking fault width along the dislocation line. Molecular dynamics simulations also show that the critical stress to move a dislocation in $Co_{30}Fe_{16.67}Ni_{36.67}Ti_{16.67}$ is increased by approximately one order of magnitude with respect to pure Ni [120]. Rao *et al.* find a similar range of yield stress to that measured in the Cantor alloy CrMnFeCoNi [114]. Experiments in CrMnFeCoNi show large variability in the stacking fault width in agreement with atomistic simulations [121]. Recent simulations of FCC HEAs predict negative values of stacking fault energies that indicate the metastability of the material [122, 123].

Curtin *et al.* [117, 118, 124–126] derive an atomistic based model to predict the critical strength of HEAs. In this theory, strengthening is the result of local fluctuations which impede the motion of dislocations. The flow stress at zero temperature obtained by Curtin *et al.* is:

$$\tau_c = \frac{\pi}{2}\frac{\Delta E_b}{bL_c w_c} \tag{4.1}$$

where ΔE_b is an energy barrier, L_c is the length of a dislocation segment fluctuation in the direction of the dislocation line, w_c is the amplitude of the dislocation bowing, and b is the magnitude of the Burgers vector.

In this work, dislocation dynamics simulations are used to predict the effect of the stacking fault variability on the strengthening of Ni-based alloys. To this end, the evolution of partial dislocations is simulated with a phase field dislocation model (PFDM) for FCC metals [4, 5] in which the stacking fault energy is varied locally to qualitatively represent the energy landscapes of HEAs. Relevant stacking fault strengthening models are reviewed in Section 4.2. The PFDM is derived in Section 4.3 with emphasis on the incorporation of the gamma-surface [127]. Several examples

that highlight the capabilities of PFDM are described in Section 4.4. The examples include, the dependency of the yield stress on the stacking fault energy in Section 4.4.1, the decorrelation of partial dislocations in the presence of impenetrable particles in Section 4.4.2, and the strengthening of alloys with penetrable particles which have different stacking fault energy values in Section 4.4.3. In Section 4.5, PFDM simulations of the evolution of partial dislocations in a stacking fault energy landscape with local fluctuations are used to model the response of HEAs. In particular, the yield stress dependency on these fluctuations is predicted and compared with a theoretical strengthening model.

The simulations predict a range of behaviors in agreement with observation, including: a yield stress increase with decreasing stacking fault energy; decorrelation of the leading and trailing partial dislocations when extended dislocations interact with impenetrable obstacles [128, 129]; strengthening in alloys with penetrable particles which have different stacking fault energy values [110, 130]. Finally, the evolution of partial dislocations in stacking fault energy landscapes with local fluctuations predicts an increase of the yield stress. Furthermore, along with the strengthening characteristics of the system, the simulations also predict a maximum of the yield stress when the size of the regions where different values of stacking fault energy are assigned, approaches the size of the average equilibrium stacking fault width in the alloy.

4.2 Stacking fault strengthening

Extended dislocations can lower their energy by being in regions with lower stacking fault energy. Therefore, an external stress needs to be applied to move a dislocation from a region with stacking fault energy γ_1, to another with larger stacking fault energy γ_2. This critical stress is calculated here, following the work of Hirsch and Kelly [110]. The forces on each partial dislocation due to an external stress $\boldsymbol{\sigma}$,

the elastic interaction with the other partial dislocation, and the stacking fault are in equilibrium, therefore:

$$\begin{aligned} \frac{K}{R_{12}} + \gamma_1 + \boldsymbol{\sigma} \cdot \boldsymbol{b_1} \cdot \boldsymbol{n} = 0, \\ -\frac{K}{R_{12}} - \gamma_2 + \boldsymbol{\sigma} \cdot \boldsymbol{b_2} \cdot \boldsymbol{n} = 0. \end{aligned} \tag{4.2}$$

where R_{12} is the distance between the two dislocations, $\boldsymbol{b_1}$ and $\boldsymbol{b_2}$ are the Burgers vectors of the partial dislocations, $\boldsymbol{n}$ is the normal of the slip plane, and

$$K = \frac{\mu b_1^2 (2-\nu)}{8\pi(1-\nu)} \left(1 - \frac{2\nu cos2\theta}{2-\nu}\right) \tag{4.3}$$

where θ is the angle between the Burgers vector of the full dislocation $\boldsymbol{b} = \boldsymbol{b_1} + \boldsymbol{b_2}$ and the dislocation line direction, μ is the shear modulus, and ν is the Poisson's ratio. In Equation 4.2, it is assumed that the boundary between the two regions is straight and parallel to the full dislocation line.

Adding the two Equations 4.2 and noting that $(\boldsymbol{b_1} + \boldsymbol{b_2})^T \cdot \boldsymbol{\sigma} \cdot \boldsymbol{n} = \tau b$, where τ is the resolved shear stress for the full dislocation, the critical resolved shear stress to move the extended dislocation is [110, 130]:

$$\tau_\gamma = \frac{\gamma_2 - \gamma_1}{b}. \tag{4.4}$$

Equation 4.4 indicates that strengthening is expected only if $\gamma_2 > \gamma_1$. The equilibrium distance between the two dislocations can also be obtained from Equation 4.2 as:

$$R_{12} = \frac{2K}{(\gamma_1 + \gamma_2) + \boldsymbol{\sigma} \cdot (\boldsymbol{b_2} - \boldsymbol{b_1}) \cdot \boldsymbol{n}} \tag{4.5}$$

4.2.1 Stacking fault strengthening in alloys

In alloys containing precipitates with lower stacking fault energy than the matrix, extended dislocations would reduce their energy by being in the precipitates. This results in an increase on the critical stress needed to make dislocations glide. A theory of stacking fault strengthening in alloys was developed by Hirsch and Kelly [110] extending Suzuki's work [130] for extended dislocations gliding in a matrix with

intrinsic stacking fault energy, γ_m, and circular particles with intrinsic stacking fault energy, γ_p, with $\gamma_m > \gamma_p$.

The critical stress needed to move an extended dislocation from the particle is derived with the help of the precipitation strengthening here and it agrees with the results of Hirsch and Kelly [110]. Under an externally applied stress, dislocations bow out between the solutes and in equilibrium the line tension, T, balances the maximum force, F_{max}, that an obstacle can sustain. At zero-temperature the increase in the critical stress needed to overcome the obstacles is [102]:

$$\Delta\tau_c = \left(\frac{2T}{bL}\right)\beta_c \tag{4.6}$$

where L is the effective distance between precipitates and

$$\beta_c = \frac{F_{max}}{2T}. \tag{4.7}$$

Note that in Equation 4.6, $\Delta\tau_c$ is the increment of the yield stress compared to the yield stress of the matrix without the precipitates. In this model, strengthening is the result of dislocations being pinned by precipitates. This mechanism is generally divided into two categories: strong and weak pinning [102]. The strong-pinning or Friedel's theory [103, 131, 132] treats the solutes as localized point obstacles that pin the dislocations. The zero-temperature critical stress at which the dislocations are able to overcome the point obstacles [102] with Friedel's theory is:

$$\Delta\tau^F = \left(\frac{2T}{b}\right)\beta_c^{\frac{3}{2}}c^{\frac{1}{2}}, \tag{4.8}$$

where c is the number of obstacles per unit area. In the weak-pinning or Labusch's theory [104, 133, 134] a characteristic length scale, w, within which solutes interact with dislocations is added. The zero-temperature critical stress for this model is:

$$\Delta\tau^L = C\left(\frac{2T}{b}\right)\beta_c^{\frac{4}{3}}(wc^2)^{\frac{1}{3}}. \tag{4.9}$$

where C is a factor of order one that depends on the kind of interaction between the obstacles and the dislocations [104, 105]. The force on the dislocation due to the difference between the stacking fault in the matrix and in the solutes is:

$$F_{max} = \Delta\gamma L_d, \tag{4.10}$$

where L_d is the length of the dislocation inside the particle at the critical breaking condition. The value of L_d depends on the stacking fault energy, the size of the particle, r, and the stacking fault width of the dislocation inside the particle,

$$R_p = \frac{K}{\gamma_p} \tag{4.11}$$

The analytical estimates of L_d derived by Hirsch and Kelly [110] for different regimes are used here. When $r > R_p$,

$$L_d = \sqrt{\frac{Kr}{\bar{\gamma}}}, \tag{4.12}$$

where $\bar{\gamma} = 0.5(\gamma_p + \gamma_m)$, and for $r < R_p$,

$$L_d = 2r, \tag{4.13}$$

It is important to notice that the regime transition at R_p is dominated not only by the particle size but also by $K/\bar{\gamma}$. Furthermore, comparing Equations 4.12 and 4.13 it is clear that the strengthening of larger particles scales with $r^{1/2}$ reducing the effective strengthening mechanism compared to smaller particles. Replacing Equations 4.10, 4.12, and 4.13 in Equation 4.8, the critical stress for Friedel's statistics is:

$$\Delta\tau^F = \begin{cases} \frac{2Tr^{3/2}c^{1/2}}{b^{5/2}} \left(\frac{\Delta\gamma b}{T}\right)^{3/2} & \text{if } r \leq R_e \\ \frac{2Tr^{3/4}c^{1/2}}{b^{7/4}} \left(\frac{\Delta\gamma}{2T}\sqrt{\frac{Kb}{\bar{\gamma}}}\right)^{3/2} & \text{if } r \geq R_e \end{cases} \tag{4.14}$$

Similarly, the critical stress for Labusch's statistics can be obtained replacing Equations 4.10 , 4.12, and 4.13 in Equation 4.9

$$\Delta\tau^L = \begin{cases} C\frac{2Tr^{5/3}c^{2/3}}{b^{7/3}} \left(\frac{\Delta\gamma b}{T}\right)^{4/3} & \text{if } r \leq R_e \\ C\frac{2Tc^{2/3}r}{b^{5/3}} \left(\frac{\Delta\gamma}{2T}\sqrt{\frac{Kb}{\bar{\gamma}}}\right)^{4/3} & \text{if } r \geq R_e \end{cases} \tag{4.15}$$

where $w = r$ is used in Equation 4.15.

Figure 4.1 shows the dependency of the increment of the yield stress on the size of the particles with $f = \pi r^2 c = 0.1$, $T = \alpha\mu b^2$, $\alpha = 0.12$, $\Delta\gamma = 135.52$ mJ/m^2, $b = 0.25$ nm, $C = 1$, and $\theta = \frac{\pi}{2}$ in Equation 4.3. The dashed lines indicate that Equations

4.14 and 4.15 are not valid when r approaches R_p but a maximum is expected when the particle size is close to R_p.

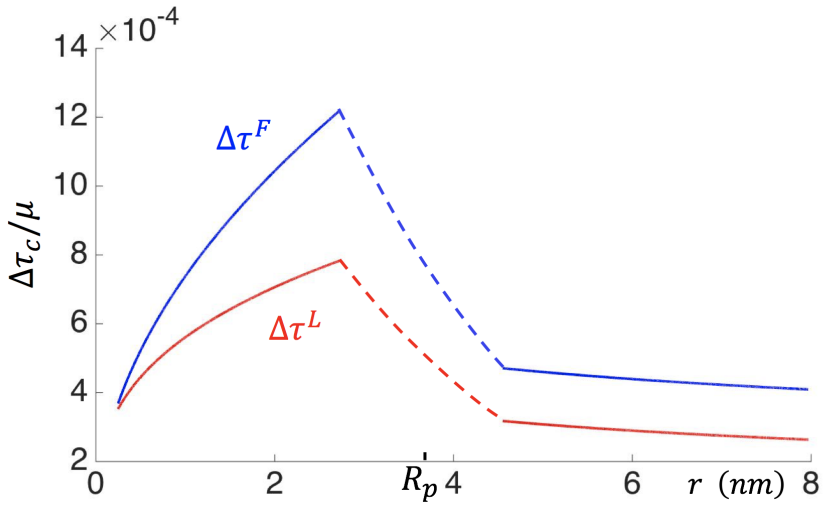

Figure 4.1. Critical stress increment due to the presence of precipitates using Equations 4.14 to 4.15.

4.3 Phase field dislocations model

In the PFDM, a displacement in a slip system in FCC materials can be described by the sum scalar phase field variables $\xi^{\alpha}(\boldsymbol{x})$ as:

$$\boldsymbol{\Delta}(\boldsymbol{x}) = b\sum_{\alpha=1}^{3}\xi^{\alpha}(\boldsymbol{x})\boldsymbol{s}^{\alpha}. \tag{4.16}$$

where $\boldsymbol{s_1} = \sqrt{2}/2[0\bar{1}1]$, $\boldsymbol{s_2} = \sqrt{2}/2[10\bar{1}]$, and $\boldsymbol{s_3} = \sqrt{2}/2[\bar{1}10]$ are the directions of the three Burgers vectors in the slip plane (111).

For example, the displacement of the atoms in the stacking fault area shown as Region 2 in Figure 4.2 can be expressed as:

$$\boldsymbol{\Delta}_2 = \boldsymbol{b}_p^1 = \frac{\sqrt{2}b}{6}[2\bar{1}\bar{1}] = \frac{\sqrt{2}b}{6}\boldsymbol{s}_2 - \frac{\sqrt{2}b}{6}\boldsymbol{s}_3 \tag{4.17}$$

Likewise, the displacement in Region 3 in Figure 4.2 is the sum of the the two Shockley partials:

$$\boldsymbol{\Delta}_3 = \boldsymbol{b}_p^1 + \boldsymbol{b}_p^2 = \frac{\sqrt{2}b}{6}[2\bar{1}\bar{1}] + \frac{\sqrt{2}b}{6}[1\bar{2}1] = b\boldsymbol{s}_1 \tag{4.18}$$

which corresponds to $\xi^1 = 1$ and $\xi^2 = \xi^3 = 0$ in Equation 4.16. Integer values of the phase field variables, see Equation 4.18, indicate that the crystal remains with perfect crystalline structure.

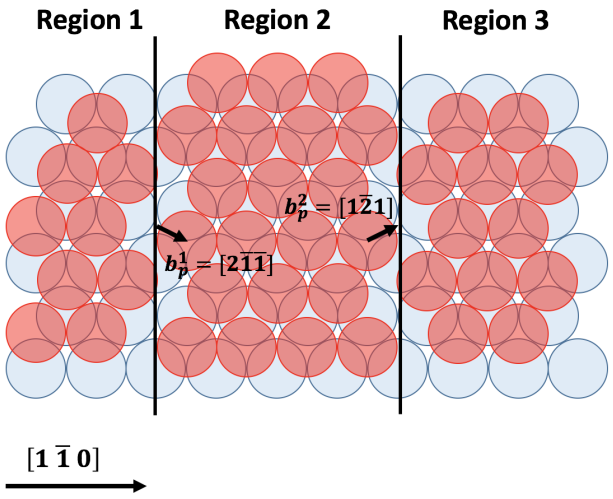

Figure 4.2. Sketch of a stacking fault region in FCC crystals. The black lines are the leading and trailing partial dislocations. The arrows indicate the direction of the Shockley partials. The blue atoms are the A layer and the red atoms are the B layer in the FCC stacking sequence.

To identify stacking fault regions the projection of the displacement on a Burgers vector direction can be used. For example, Hunter *et al.* [4] utilized the projection of the displacement on the Burgers vector of a perfect dislocation, $\boldsymbol{s}_1$, which results in:

$$\boldsymbol{\Delta}_2 \cdot \boldsymbol{s}_1 = \frac{b}{6}[2\bar{1}\bar{1}] \cdot [1\bar{1}0] = 0.5b \tag{4.19}$$

Cao *et al.* [5] used the projection of the displacement on one of the partial dislocation Burgers vector:

$$\boldsymbol{\Delta}_2 \cdot \boldsymbol{b}_p^2 = \frac{b^2}{6\sqrt{3}}[2\bar{1}\bar{1}] \cdot [1\bar{2}1] = 0.289b \tag{4.20}$$

and

$$\boldsymbol{\Delta}_2 \cdot \boldsymbol{b}_p^1 = \frac{b^2}{6\sqrt{3}}[2\bar{1}\bar{1}] \cdot [2\bar{1}\bar{1}] = 0.578b. \tag{4.21}$$

4.3.1 Dislocation energies

The evolution of the phase field variables introduced in Equation 4.16 follows from the minimization of the total energy of the dislocation ensemble [5, 135]. This energy is composed of the strain energy, E^e, and the misfit energy, E^m, that accounts for the formation of stacking faults through the introduction of the parametrization of the gamma-surface [4, 136] and it is described in the following sections.

Strain energy

The plastic distortion β_{ij}^p can be written in terms of the phase field variables as

$$\beta_{ij}^p(\mathbf{x}) = \frac{1}{d}\sum_{\alpha=1}^{N} b^\alpha \xi^\alpha(\mathbf{x}) m_i^\alpha s_j^\alpha \tag{4.22}$$

where N is the total number of slip systems, d is the distance between slip planes, and $\boldsymbol{m}^\alpha$ is the normal to the slip plane α. The total distortion can be obtained using the elastic Green's function G_{ij} [13, 51] as

$$\beta_{ij}(\boldsymbol{x}) = -G_{ik,l} \star (C_{klmn}\beta_{mn}^p(\boldsymbol{x}))_{,j} \tag{4.23}$$

where C_{klmn} is the tensor of elastic constants and $(\star)$ represents the convolution operator. The strain energy can be calculated as

$$E^e = \frac{1}{2}\int_\Omega C_{ijkl}(\epsilon_{ij} - \epsilon_{ij}^p)(\epsilon_{kl} - \epsilon_{kl}^p) d^3x \tag{4.24}$$

where Ω is the domain, the strain $\epsilon_{ij} = sym(\beta_{ij})$ is the symmetric part of the distortion, and $\epsilon_{ij}^p = sym(\beta_{ij}^p)$ is the plastic strain. To express the strain energy in terms of the plastic strain only, the total strain can be obtained from Equation 4.23 as

$$\epsilon_{ij}(\mathbf{x}) = \fint \hat{G}_{jk}(\mathbf{k}) k_i k_l C_{klmn} \hat{\epsilon^p}_{mn}(\mathbf{k}) e^{i\mathbf{k}\cdot\mathbf{x}} \frac{d^3\mathbf{k}}{(2\pi)^3} + \bar{\epsilon^p}_{ij} + \epsilon_{ij}^{bc} \tag{4.25}$$

where the symbol ˆ denotes the Fourier transform of a function, k_i are the wave vectors, the symbol $\oint$ is the principal value of the integral, and the average plastic strain is

$$\bar{\epsilon^p}_{ij} = \frac{1}{\Omega}\int_{\Omega} \epsilon^p_{ij} d^3x \tag{4.26}$$

The last term in Equation 4.25 is determined by the boundary conditions [5]. If the average strain $\bar{\epsilon}_{ij}$ is controlled:

$$\epsilon^{bc}_{ij} = \bar{\epsilon}_{ij} - \bar{\epsilon^p}_{ij} \tag{4.27}$$

while in the stress controlled case

$$\epsilon^{bc}_{ij} = S_{ijkl}\sigma^{ap}_{ij}. \tag{4.28}$$

Inserting Equation 4.25 in Equation 4.24, the strain energy is obtained as a function of plastic strain for the strain controlled case:

$$E^e = \oint \frac{1}{2}\hat{A}_{mnuv}(\mathbf{k})\hat{\epsilon}^p_{mn}(\mathbf{k})\hat{\epsilon}^{p*}_{uv}(\mathbf{k})\frac{d^3k}{(2\pi)^3} - \bar{\epsilon}_{ij}\int_{\Omega} C_{ijkl}\epsilon^p_{kl}(\boldsymbol{x})d^3x + \frac{V}{2}C_{ijkl}\bar{\epsilon}_{ij}\bar{\epsilon}_{kl} \tag{4.29}$$

where the symbol $*$ denotes the complex conjugate, and

$$\hat{A}_{mnuv}(\mathbf{k}) = C_{mnuv} - C_{kluv}C_{ijmn}\hat{G}_{ki}k_jk_l. \tag{4.30}$$

The strain energy for the stress controlled case can be obtained by inserting Equation 4.25 in Equation 4.24 and adding a term $-V\sigma^{ap}_{ij}\bar{\epsilon^p}_{ij}$ representing the relaxation of the elastic energy during stress controlled condition. The elastic energy for the stress controlled case results:

$$E^e = \oint \frac{1}{2}\hat{A}_{mnuv}(\mathbf{k})\hat{\epsilon}^p_{mn}(\mathbf{k})\hat{\epsilon}^{p*}_{uv}(\mathbf{k})\frac{d^3k}{(2\pi)^3} - \frac{V}{2}S_{ijkl}\sigma^{ap}_{ij}\sigma^{ap}_{kl} - \sigma^{ap}_{ij}\bar{\epsilon^p}_{ij}. \tag{4.31}$$

Misfit energy

The gamma-surface is the energy per unit area that dislocations experience when the crystal is subjected to a shear displacement [127]. Figure 4.3 shows this energy density as a function of the displacement in the $[1\bar{1}0]$ direction for Nickel [136].

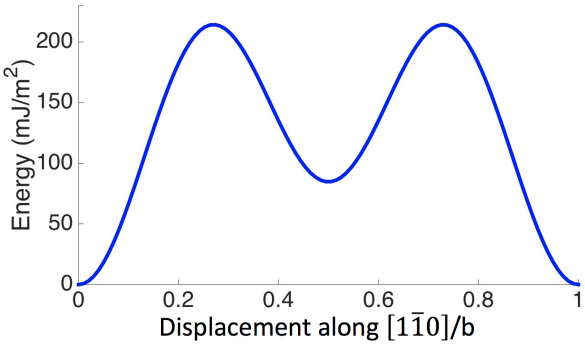

Figure 4.3. Stacking fault energy profile in the direction [1$\bar{1}$0].

The incorporation of the gamma-surface in the PFDM [4, 136] makes it possible to predict the equilibrium stacking fault width of several FCC metals [4], the nucleation of partial dislocations in nanocrystalline materials [5], and twinning [137] in good agreement with atomistic simulations and experiments. The gamma-surface is introduced as the integral over the slip planes of the energy per unit area obtained from atomistic simulations [4]:

$$E^m = \sum_{\alpha=1}^{N} \int_{S_\alpha} \phi[\boldsymbol{\xi}] d^2x, \tag{4.32}$$

where the integral is over the slip planes S_α. A representation as a 2D Fourier series in terms of the displacement on the slip planes proposed by Schoeck [138] is used in the PFDM approach [4]:

$$\begin{aligned}
\phi(\xi^1,\xi^2,\xi^3) =& \{c_0 + c_1[\cos 2\pi(\xi^1-\xi^2) + \cos 2\pi(\xi^2-\xi^3) + \cos 2\pi(\xi^3-\xi^1)] \\
&+ c_2[\cos 2\pi(2\xi^1-\xi^2-\xi^3) + \cos 2\pi(2\xi^2-\xi^3-\xi^1) + \cos 2\pi(2\xi^3-\xi^1-\xi^2)] \\
&+ c_3[\cos 4\pi(\xi^1-\xi^2) + \cos 4\pi(\xi^2-\xi^3) + \cos 4\pi(\xi^3-\xi^1)] \\
&+ c_4[\cos 4\pi(3\xi^1-\xi^2-2\xi^3) + \cos 4\pi(3\xi^1-2\xi^3-\xi^3) + \cos 4\pi(3\xi^2-\xi^3-2\xi^1) \\
&+ \cos 4\pi(3\xi^2-2\xi^3-\xi^1) + \cos 4\pi(3\xi^3-\xi^1-2\xi^2) + \cos 4\pi(3\xi^3-2\xi^1-\xi^2)] \\
&+ a_1[\sin 2\pi(\xi^1-\xi^2) + \sin 2\pi(\xi^2-\xi^3) + \sin 2\pi(\xi^3-\xi^1)] \\
&+ a_3[\sin 4\pi(\xi^1-\xi^2) + \sin 4\pi(\xi^2-\xi^3) + \sin 4\pi(\xi^3-\xi^1)]\}.
\end{aligned} \tag{4.33}$$

The material-dependent coefficients, $c_0, c_1, c_2, c_3, c_4, a_1, a_3$, are determined by fitting this approximation to the gamma-surface obtained by atomistic simulations. The values of these coefficients for Nickel are listed in Table 4.1 [4].

Table 4.1. Coefficients (mJ/m^2) used in Equation 4.33 to parametrize the gamma-surface for Nickel [4].

Material	c_0	c_1	c_2	c_3	c_4	a_1	a_3
Ni	410.0	-52.0	-120.6	35.2	0.6	-66.2	-75.3

A simplified form of the expression in Equation 4.33 can be written as an explicit function of the intrinsic stacking fault energy, γ, and the unstable stacking fault energy, γ_u, [4, 136, 139, 140]:

$$\phi(\xi) = \gamma \sin^2(\pi\xi) + (\gamma_u - \gamma/2) \sin^2(2\pi\xi). \tag{4.34}$$

The advantage of this simplification is that depends directly on γ and γ_u, but the limitation is that Equation 4.34 can be used only for displacements represented with a single phase field.

Energy minimization

The equilibrium configuration of the a dislocation ensemble is obtained from the minimization of the total energy. This results in a system of α coupled equations for the phase field variables of the form:

$$\frac{\delta E^e[\boldsymbol{\xi}(\mathbf{x})] + E^m[\boldsymbol{\xi}(\mathbf{x})]}{\delta \xi^\alpha(\mathbf{x})} = 0 \tag{4.35}$$

Materials parameters for Ni, listed in Table 4.2 are used in all the simulations unless otherwise noted.

Table 4.2. Material parameters for Nickel [136, 141].

μ (GPa)	ν	b (nm)	$\gamma(\mathrm{mJ/m^2})$	$\gamma_u(\mathrm{mJ/m^2})$
75.0	0.33	0.249	84.7	211.7

4.4 Examples

In this section several examples of the behavior of extended dislocations are presented to illustrate the capabilities of the PFDM. The dependency of the yield stress on the stacking fault energy and the interaction of extended dislocations with obstacles are studied. The elastic constants used in the simulations are listed in Table 4.2, while different values of the unstable and intrinsic stacking fault energies are chosen for each simulation.

4.4.1 Yield stress and stacking fault width calculation

Atomistic and dislocation dynamics simulations show that the equilibrium stacking fault width depends on the intrinsic and the unstable stacking fault energies [4, 142]. Therefore, both quantities influence the structure of the dislocation and the response of the material. To study the effect of the stacking fault energies on the yield stress PFDM simulations are performed in which an extended edge dislocation is placed in a domain with the dimension $512b \times 256b \times 32b$. Different values of unstable and intrinsic stacking fault energies are assigned to the domain. The yield stress is defined as the minimum externally applied stress needed for the dislocation to glide. Figure 4.4 shows the predicted yield stress as a function of the difference between the unstable and intrinsic stacking fault energies. The arrow indicates the value of yield stress predicted with the values in Table 4.2 for Nickel. There is a linear relationship between the yield stress, τ_c, and the difference between the unstable and intrinsic stacking fault energies. Table 4.3 contains selected values of yield stress and the equilibrium stacking fault width obtained with the PFDM simulations. From the

table, the stacking fault width R_e decreases with respect to the intrinsic stacking fault energy, which is in agreement with Equation 4.11.

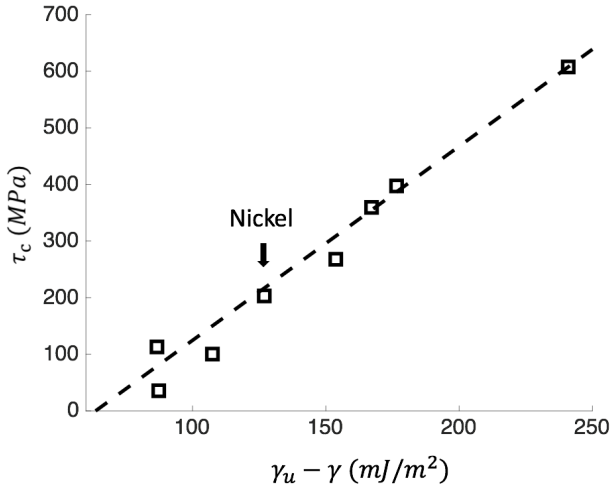

Figure 4.4. Simulated yield stress τ_c versus $\gamma_u - \gamma$.

Table 4.3. Calculated critical stress for a uniform distribution of stacking fault energy with $\gamma_u = 211.7$ mJ/m^2. The error in R_e is the grid size.

γ (mJ/m^2)	τ_c (MPa)	R_e (nm)
35.0	400	5.2± 0.25
72.0	235	3.0± 0.25
84.7	220	2.6± 0.25
127.1	145	1.7± 0.25

4.4.2 Solute strengthening in alloys

In the presence of impenetrable particles, dislocations bend to enter the regions between two neighboring particles. A decorrelated motion of the partial dislocations is observed in these channels, and as a result the stacking fault width changes as the

two partial dislocations move [108, 128, 129]. The response of an extended dislocation interacting with an array of impenetrable circular particles under the applied stress in different directions is studied in this section.

The evolution of an extended edge dislocation with full Burgers vector in the direction [110] is shown in Figures 4.5, 4.6, and 4.7. The Burgers vectors of the decorrelated partial dislocations are indicated in the Figure 4.2. The projection of the applied stress on the slip plane is indicated in each configuration and the stacking fault is shown in green. The radius of the particles is 11.2 nm and the distance between two neighbouring particles is 9.6 nm. The elastic constants and the stacking fault energy used in the simulations are listed in Table 4.2.

In Figure 4.5, the applied stress is in the same direction as the Burgers vector of the extend dislocation. The magnitude of the stress resolved on both the leading and trailing dislocations are the same. The extended dislocation bends in the channels between two neighbouring particles and when the applied stress is sufficient enough the dislocation overcomes the particles leaving behind loops.

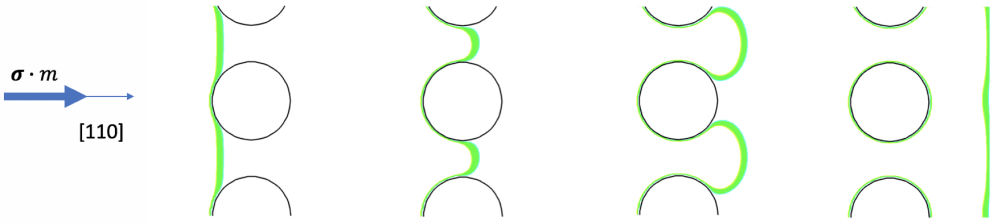

Figure 4.5. PFDM simulation showing an extended dislocation interacting with impenetrable particles. The resolved shear stress is the same on both partial dislocations.

Figure 4.6 shows the evolution of the dislocation when the projection of the applied stress on the slip plane forms a 60^o angle with the [110] direction. Under this condition, the resolved shear stress is zero for the leading partial. Therefore, the leading partial blocks the movement of the trailing partial and the stacking fault width decreases.

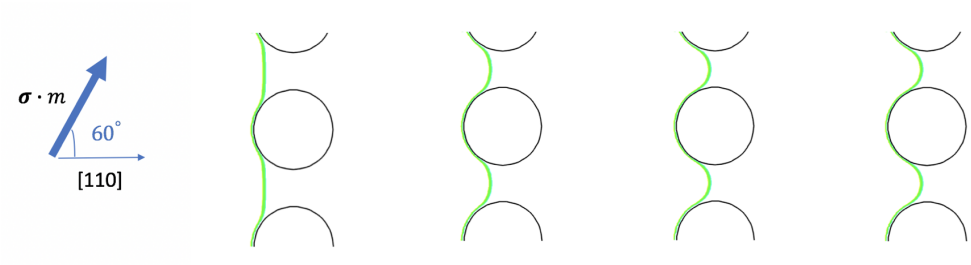

Figure 4.6. PFDM simulation showing an extended dislocation interacting with impenetrable particles. The resolved shear stress is zero for the leading partial.

In Figure 4.7 the resolved shear stress on the trailing dislocation is zero. The increase in the stacking fault width is evident in the figure. This decorrelation mechanism was observed in super alloys [128, 129, 139] and it is of key importance to understand deformation twinning [106, 108] and strengthening that cannot be explained without taking into account partial dislocations [107, 109].

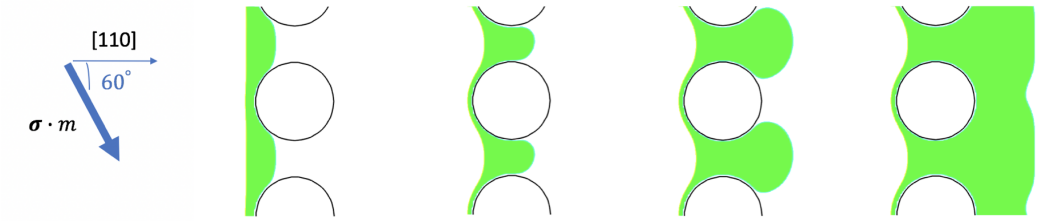

Figure 4.7. PFDM simulation showing an extended dislocation interacting with impenetrable particles. The resolved shear stress is zero for the trailing partial.

4.4.3 Stacking fault strengthening in alloys

PFDM simulations of an extended edge dislocation moving through an array of particles are performed in a $512b \times 256b \times 32b$ domain. The material properties of Nickel listed in Table 4.2 are used in the matrix. The elastic constants of Ni are also

used in the particles, while the effects of different values of the stacking fault energy are studied. The intrinsic stacking fault energy γ_p and the unstable stacking fault energy γ_p^u in the particles are listed in Table 4.4. The radius of the particles is 28.2 nm and the distance between two particles is 9.9 nm. In all the cases, the projection of the applied stress on the slip plane is in the direction [110].

Table 4.4. Stacking fault energy in the particles in the simulations.

	Case 1	Case 2	Case 3	Case 4
γ_p (mJ/m^2)	43.9	175.4	84.7	84.7
γ_p^u (mJ/m^2)	211.7	211.7	105.8	423.4

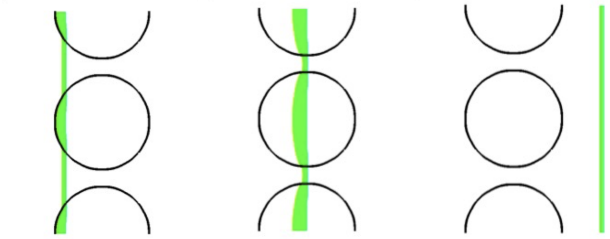

(a) Case 1

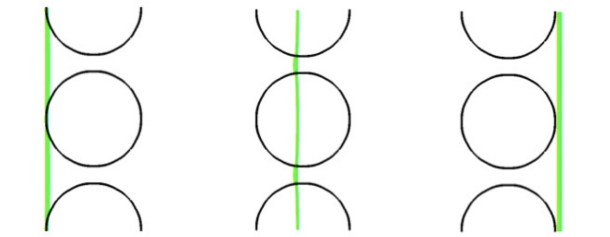

(b) Case 2

Figure 4.8. An extended dislocation passing through an array of particles with (a) lower and (b) higher intrinsic stacking fault energy than the matrix.

Figure 4.8 (a) shows the evolution of the dislocations when the intrinsic stacking fault energy in the particles is 43.9 mJ/m^2 which is lower than the matrix. The

leading partial remains straight, while the trailing partial curves inside the particle producing a larger stacking fault width. The applied stress required to move the extended dislocation away from the particles needs to be increased. The simulation for Case 2 is shown in Figure 4.8 (b). The intrinsic stacking fault energy in the particles is larger than the matrix. The stacking fault width is smaller inside the particles and no strengthening is observed which is in agreement with Equations 4.14 and 4.15 for $r > R_p$.

In Cases 3 and 4, γ_p^u is modified with respect to the unstable stacking fault energy of the matrix. When the unstable stacking fault energy is reduced in Case 3 in Figure 4.4.3 (a), the dislocation segments inside the particles advance ahead of the segments in the matrix and no strengthening is observed. For Case 4, shown in Figure 4.4.3 (b), the dislocation bows out and leaves loops inside the particles that shrink and disappear to reduce the energy. The stress required to move the extended dislocation is greatly increased.

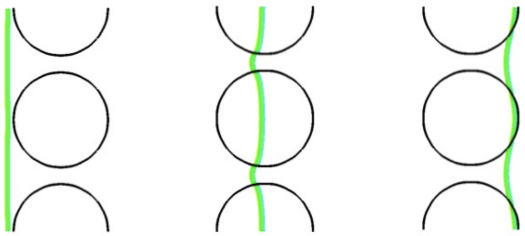

(a) Case 3

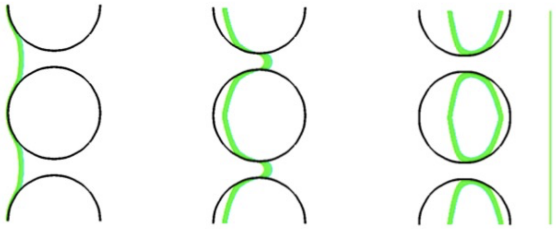

(b) Case 4

Figure 4.9. An extended dislocation passing through an array of particles with (a) lower and (b) higher unstable stacking fault energy than the matrix.

Several simulations with the geometry shown in Figure 4.8 are performed with different intrinsic stacking fault energies in the particles. The critical resolved shear stress is calculated as the minimum applied stress needed to overcome the particles. The increase of the critical stress, $\Delta\tau_c$, as a function of the stacking fault energy difference in particle and the matrix, $\Delta\gamma = \gamma_m - \gamma_p$, is shown in Figure 4.10. For comparison the critical stress obtained using Friedel and Labusch statistics for large particles, Equations 4.14 and 4.15, are also included, with $\alpha = 0.07$, $f = 0.28$, and $\theta = \frac{\pi}{2}$. Note that the critical stress for $\Delta\gamma = 0$ corresponds to the case with no particles and that no strengthening is predicted if $\Delta\gamma \leq 0$ in agreement with Equations 4.14 and 4.15.

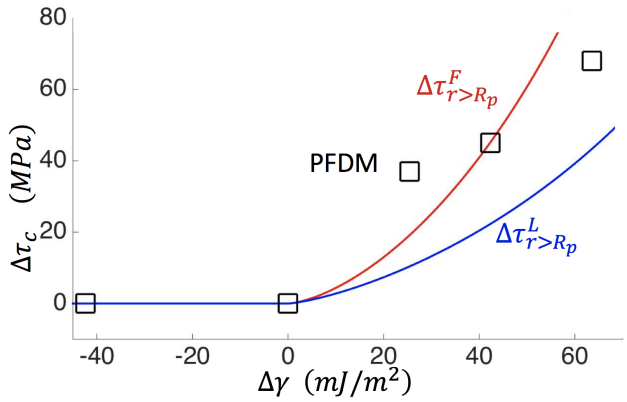

(a)

Figure 4.10. Simulated critical stress for particles in a matrix with different intrinsic stacking fault energy as a function of $\Delta\gamma = \gamma_m - \gamma_p$. Analytical solutions using Friedel's and Labusch's models are also included.

4.5 Stacking fault strengthening in HEAs

Atomistic simulations of HEAs show that the stacking fault energy varies locally with the local composition of the alloy [117, 120, 121]. The effects of these local variations on the core structure of the dislocations and on the critical resolved shear

stress are studied in this section. To isolate the result of the chemical misfit, the lattice misfit is not included in the simulations.

In the PFDD simulations, different values of the intrinsic stacking fault energy are assigned randomly to regions on the slip plane, while all other material properties are the same. The regions are defined using a Voronoi tessellation algorithm with average region size ranging from 0.5 nm to 12.0 nm. Two examples are shown in Figure 4.11. This range is chosen following the concentration fluctuations observed in the experiments [143] and the range of characteristic lengths from 0.4 nm to 12.0 nm used in Curtin's model.

The values of the intrinsic stacking fault energy assigned to each region are chosen from uniform distributions with standard deviation, $\sigma_\gamma = \frac{\gamma^{max}-\gamma^{min}}{2\sqrt{3}}$, support $[\gamma^{min}, \gamma^{max}]$, and average $\bar{\gamma} = \frac{\gamma^{max}+\gamma^{min}}{2}$. The average value $\bar{\gamma}$ is chosen from values reported by Varvenne *et al.* [118] for the Ni-Co-Fe-Cr-Mn family of high entropy alloys, in the range of 20 mJ/m^2 to 100 mJ/m^2.

Two straight extended dislocations with Burgers vectors in the [110] direction are placed on the slip plane, as shown in Figure 4.11. Under no applied stress, each dislocation splits into two partials, the stacking fault region is shown in grey in Figure 4.11 for $\bar{\gamma} = 35.0$ mJ/m^2 and $d = 5.8$ nm, and for $\bar{\gamma} = 72.0$ mJ/m^2 and $d = 3.2$ nm.

The critical stress is defined as the minimum applied stress at which the extended dislocations glide. This critical stress is calculated for different distributions of stacking fault energy landscapes similar to Figure 4.11.

Figure 4.12 shows the critical stress increment, $\Delta\tau_c$, as a function of the stacking fault region size for $\bar{\gamma} = 35.0$ mJ/m^2, 84.7 mJ/m^2, and 127.1 mJ/m^2 with $\sigma_\gamma = 12$ mJ/m^2. For each data point, three realizations are performed to eliminate the possible errors. Each critical stress shown in the figure is calculated as the average value from three realizations. The critical stress increment, $\Delta\tau_c$, is calculated with respect to the critical stress obtained with a constant stacking fault energy equal to $\bar{\gamma}$. These values are listed in Table 4.3 and shown in Figure 4.4.

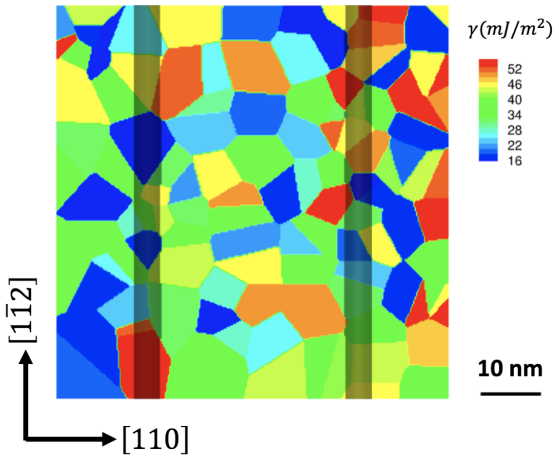

(a) $d = 5.8$ nm

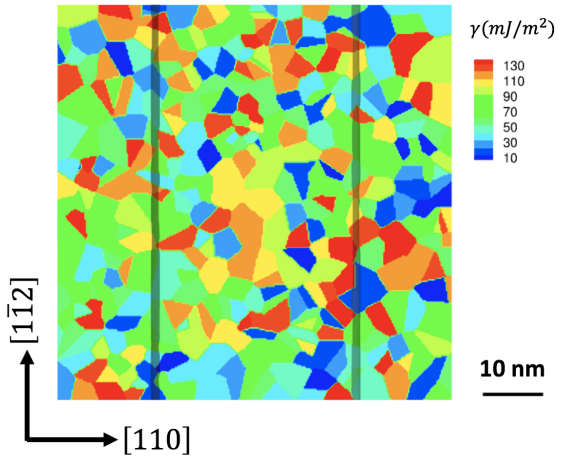

(b) $d = 3.2$ nm

Figure 4.11. Two extended dislocations in a random stacking fault landscape with (a) $d = 5.8$ nm and $\bar{\gamma} = 35.0$ mJ/m^2, (b) $d = 3.2$ nm and $\bar{\gamma} = 72.0$ mJ/m^2.

It is shown in Figure 4.12 that $\Delta\tau_c$ has a maximum in the region 2.0 nm $\leq d \leq$ 4.0 nm for $\bar{\gamma} = 127.0$ mJ/m^2; 2.0 nm $\leq d \leq$ 6.0 nm for $\bar{\gamma} = 84.7$ mJ/m^2; and 4.0 nm $\leq d \leq$ 8.0 nm for $\bar{\gamma} = 35.0$ mJ/m^2. This behavior is similar to the stacking fault strengthening model for alloys presented in Figure 4.1, in which the strengthening

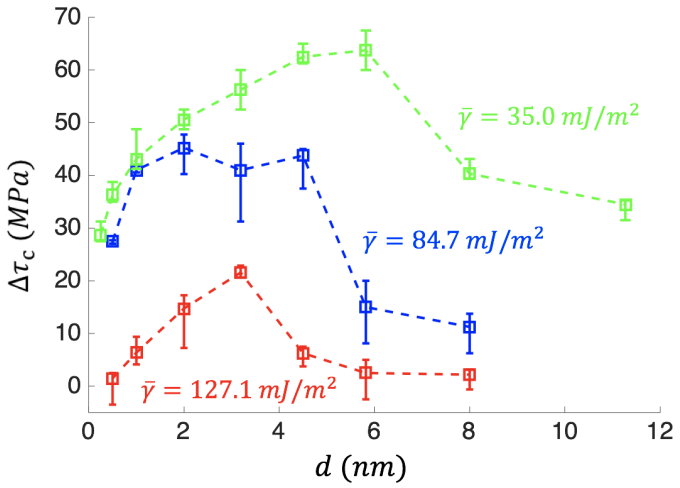

Figure 4.12. $\Delta\tau_c$ versus stacking fault region size d. The stacking fault energies are chosen randomly from uniform distributions with standard deviation $\sigma_\gamma = 12.0$ mJ/m^2.

reaches a maximum when the particle size approaches the stacking fault width inside the particles.

In the current simulations this response can be explained following the solid solution hardening model presented in Section 4.2.1 and assuming that the region size d scales with the radius of the particles r, the particle concentration $c = 1/d^2$, $\Delta\gamma = \gamma^{max} - \gamma^{min}$, and replacing R_p with $\bar{R}_e$ in Equations 4.14 and 4.15. This leads to a critical stress increment for Friedel's statistics:

$$\Delta\tau^F = \begin{cases} \frac{2T}{b}\left(\frac{\Delta\gamma}{T}\right)^{3/2} d^{1/2} & \text{if } d < \bar{R}_e \\ \frac{2T}{b}\left(\frac{\Delta\gamma}{2T}\sqrt{\frac{K}{\bar{\gamma}}}\right)^{3/2} d^{-1/4} & \text{if } d > \bar{R}_e \end{cases} \tag{4.36}$$

and similarly, the critical stress for Labusch's statistics is:

$$\Delta\tau^L = \begin{cases} \frac{2T}{b}\left(\frac{\Delta\gamma}{T}\right)^{4/3} d^{1/3} & \text{if } d < \bar{R}_e \\ 2Tb\left(\frac{\Delta\gamma}{2T}\sqrt{\frac{Kb}{\bar{\gamma}}}\right)^{4/3} d^{-1/3} & \text{if } d > \bar{R}_e \end{cases} \tag{4.37}$$

In equations 4.36 and 4.37 the critical stress increases with the region size when $d < \bar{R}_e$ and decreases for $d > \bar{R}_e$ in agreement with the simulation results in Figure 4.12.

Finally, all the simulations are compiled in Figure 4.13 which presents the critical stress as a function of the difference between γ_u and $\bar{\gamma}$. The dashed line is the yield stress calculated with a constant value of the stacking fault energy and it is extracted from Figure 4.4. The largest increase in the yield stress, shown as solid symbols, is obtained for region sizes $d \sim \bar{R}_e$. A maximum increase of up to 40% on the yield stress is observed for the largest standard deviation σ_γ studied here.

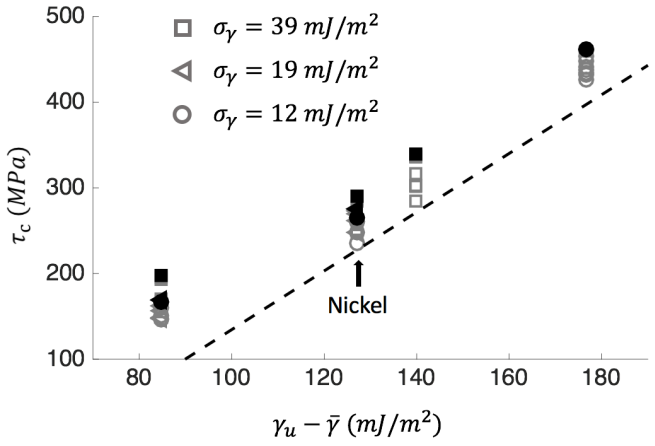

Figure 4.13. Simulated yield stress τ_c versus $\gamma_u - \bar{\gamma}$. The dashed line correspond to a constant value of stacking fault energy.

4.6 Summary and concluding remarks

The theoretical model and dislocation dynamics simulations explored in this chapter show that the yield stress can be increased by local fluctuations of the stacking fault energy. The theoretical strengthening model extends the work of Hirsch and Kelly [110] from circular precipitates to include the local variations of the stacking fault energy on the slip plane. This model predicts a maximum in the strength when

the average size of the stacking fault regions, d, is close to the average equilibrium stacking fault width, $\bar{R}_e$.

The critical stress to move two partial dislocations is predicted with PFDM simulations with several distributions of stacking fault energy that replicate the stacking fault energy landscape found in atomistic simulations of HEAs [117,120,121]. A parametric study of Ni-based HEAs is performed with the average stacking fault energy ranging from 35 mJ/m^2 to 127 mJ/m^2 while leaving all the other material parameters fixed to the values reported in Table 4.2.

The simulations show maximum strengthening for $d \sim \bar{R}_e$, in agreement with the theoretical model in Equations 4.36 and 4.37. The increase of the critical stress is calculated with respect to the value obtained with a simulation with constant stacking fault energy over the slip plane, see dashed line in Figure 4.13. Increasing the variability of the stacking fault energy distribution further increases the critical stress. Furthermore, reducing the value of the average stacking fault energy increases the value of the critical stress as shown in Figures 4.12 and 4.13. Atomistic simulations that also include lattice misfit predict an increase of up to one order of magnitude with respect to the critical resolved shear stress of pure Ni [120]. This confirms that the contributions of the chemical fluctuations are smaller than the lattice misfit in agreement with previous studies [118]. However, its effect cannot be neglected.

The structure of extended dislocations is studied with the PFDM. The simulations capture similar features observed in atomistic simulations and experiments of extended dislocations [117, 120, 121] including core size variations of up to 50% along the dislocation line. Atomistic simulations that also include the lattice misfit of the precipitates and thermal fluctuations predict variations of up to 3 factors for the core spread [120].

In particular, the simulations presented here show that extended dislocations bend to remain in zones with lower stacking fault energy. These low stacking fault energy regions pin the dislocations resulting in an increase of the critical stress. The simulations also show that extended dislocations do not present waviness if the size of the

regions is smaller than $\bar{R}_e$. Therefore, the strengthening is limited for $d < \bar{R}_e$. As expected the fluctuations of the core spread are only observed when $d > \bar{R}_e$ due to the competition between the line tension and the stacking fault energy. For $d \leq \bar{R}_e$ the line tension contribution is larger than the stacking fault energy change and therefore, partial dislocations remain straight.

The results presented here give insight information to the design of HEAs with improved strength at zero temperature by tailoring the stacking fault energy. In particular, the yield stress increases when:

- the local fluctuations of the stacking fault energy have the same characteristic length as the average equilibrium stacking fault width.
- the average stacking fault energy is reduced.
- the fluctuations of the stacking fault energy are increased.

5. SUMMARY

In this work, the crystalline materials are studied using a phase field method including the mechanical properties, the deformation mechanisms and the fracture behavior. Phase field method is able to model the evolution of the microstructure of the crystalline materials by energy minimization.

In Chapter 2, two mechanisms for Sn whisker grain formation are studied using a phase field approach. The single crystal plasticity model for Sn is presented and the material parameters are obtained by fitting to the experiments. Grain boundary migration simulations are performed and the results show that the strain energy in the material is not sufficient to form surface grain due the plastic dissipation. Grain rotation simulations are preformed using random orientations and subgrain nucleation is observed. A polycrystal thin film is simulated using grain orientations [010] and [001] and the subgrains formed are mostly in [001] direction, which is in agreement with the experiments [58]. The elastic strains, dislocation densities and the strain energy density is plotted and it is shown that the location of subgrain structures is related to high strain energy density.

In Chapter 3, the reliability of the Cu/Sn solder joints is studied by a phase field fracture model. Extensive experiments show that brittle IMCs, Cu_6Sn_5 and Cu_3Sn, form at the interface between Cu and Sn in solder joints. The electric current and the thermal processing can result in the growth of the IMCs and the nucleation of the voids. 2D finite element simulations are performed to model the fracture behavior at Cu/Sn interface. Geometries with two different Cu_3Sn thickness are created and three different initial void densities are assigned to the Cu_3Sn layer. The simulation results show that fracture occurs at interface between Cu_6Sn_5 and Cu_3Sn when the Cu_3Sn is thin and within Cu_3Sn layer when it is thick. It agrees with the experimental observations by Lee *et al.* [64]. The strength of the solder joints shows a decrease

as the increase of the Cu_3Sn thickness while the influence of the void density is not significant. To improve the reliability and the performance of Cu/Sn solders, the growth of the IMCs needs to be restricted.

In Chapter 4, the strength of the Ni-based alloys are studied using a phase field dislocation method. In incorporation of the gamma-surface, a full dislocation split into two partial dislocations. The decorrelation of dislocations is modeled at the presence of an array of impenetrable and penetrable particles with different stacking fault energies. To model the microstructure of the high entropy alloys, different values of intrinsic stacking fault energy are assigned to regions the size of which ranges from 0.5 nm to 12 nm. The strength of the alloys is obtained by applying a shear stress to move the dislocation on the slip plane. The local fluctuation of the stacking fault energy can strengthen the material and a strong size dependency is observed. The maximum strengthening can be attained when the average region size is the same as the equilibrium stacking fault width.

REFERENCES

REFERENCES

[1] N. Moelans, B. Blanpain, and P. Wollants. Quantitative analysis of grain boundary properties in a generalized phase field model for grain growth in anisotropic systems. *Phys. Rev. B*, 78:024113, Jul 2008.

[2] C. Miehe, F. Welschinger, and M. Hofacker. Thermodynamically consistent phase-field models of fracture: Variational principles and multi-field FE implementations. *International Journal for Numerical Methods in Engineering*, 83(10):1273–1311, 2010.

[3] Christian Miehe, Lisa-Marie Schnzel, and Heike Ulmer. Phase field modeling of fracture in multi-physics problems. Part I. balance of crack surface and failure criteria for brittle crack propagation in thermo-elastic solids. *Computer Methods in Applied Mechanics and Engineering*, 294:449–485, 2015.

[4] Abigail Hunter, Irene J Beyerlein, Timothy C Germann, and Marisol Koslowski. Influence of the stacking fault energy surface on partial dislocations in fcc metals with a three-dimensional phase field dislocations dynamics model. *Physical Review B*, 84(14):144108, 2011.

[5] Lei Cao, Abigail Hunter, Irene J Beyerlein, and Marisol Koslowski. The role of partial mediated slip during quasi-static deformation of 3d nanocrystalline metals. *Journal of the Mechanics and Physics of Solids*, 78:415–426, 2015.

[6] Eric Chason, Nitin Jadhav, Fei Pei, Eric Buchovecky, and Allan Bower. Growth of whiskers from Sn surfaces: Driving forces and growth mechanisms. *Progress in Surface Science*, 88(2):103 – 131, 2013.

[7] E. Chason, F. Pei, C. L. Briant, H. Kesari, and A. F. Bower. Significance of nucleation kinetics in Sn whisker formation. *Journal of Electronic Materials*, 43(12):4435–4441, Dec 2014.

[8] Eric Chason and Fei Pei. Measuring the stress dependence of nucleation and growth processes in Sn whisker formation. *JOM*, 67(10):2416–2424, Oct 2015.

[9] P. T. Vianco and J. A. Rejent. Dynamic recrystallization (DRX) as the mechanism for Sn whisker development. part i: A model. *Journal of Electronic Materials*, 38(9):1815–1825, Sep 2009.

[10] P. T. Vianco and J. A. Rejent. Dynamic recrystallization (DRX) as the mechanism for sn whisker development. partii: Experimental study. *Journal of Electronic Materials*, 38(9):1826–1837, Sep 2009.

[11] Tomoyuki Kakeshita, Ken'ichi Shimizu, Ryusuke Kawanaka, and Tomoharu Hasegawa. Grain size effect of electro-plated tin coatings on whisker growth. *Journal of Materials Science*, 17(9):2560–2566, Sep 1982.

[12] Subramanya Sadasiva, Ganesh Subbarayan, Lei Jiang, and Daniel Pantuso. Numerical simulations of electromigration and stressmigration driven void evolution in solder interconnects.(author abstract)(report). *Journal of Electronic Packaging*, 134(2):020907–20905), 2012.

[13] Marisol Koslowski, Alberto Cuitiño, and Michael Ortiz. A phase-field theory of dislocations dynamics, strain hardening and hysteresis in ductile single crystals. *Journal of the Mechanics and Physics of Solids*, 50(12):2957–2635, 2002.

[14] Xiaorong Cai, Carol A Handwerker, John E Blendell, and Marisol Koslowski. Shallow grain formation in Sn thin films. *Acta Materialia*, 192:1–10, 2020.

[15] J. W. Osenbach. Tin whiskers: An illustrated guide to growth mechanisms and morphologies. *JOM*, 63(10):57, Oct 2011.

[16] Milton O. Peach. Mechanism of growth of whiskers on Cadmium. *Journal of Applied Physics*, 23(12):1401–1403, 1952.

[17] S. Eloise Koonce and S. M. Arnold. Growth of metal whiskers. *Journal of Applied Physics*, 24(3):365–366, 1953.

[18] J. D. Eshelby. A tentative theory of metallic whisker growth. *Phys. Rev.*, 91:755–756, Aug 1953.

[19] F.C. Frank. Xc. on tin whiskers. *The London, Edinburgh, and Dublin Philosophical Magazine and Journal of Science*, 44(355):854–860, 1953.

[20] J. B. LeBret and M. G. Norton. Electron microscopy study of tin whisker growth. *Journal of Materials Research*, 18(3):585–593, 2003.

[21] K.N. Tu and J.C.M. Li. Spontaneous whisker growth on lead-free solder finishes. *Materials Science and Engineering: A*, 409(1):131 – 139, 2005. Micromechanics of Advanced Materials II.

[22] P. Sarobol, Y. Wang, W. H. Chen, A. E. Pedigo, J. P. Koppes, J. E. Blendell, and C. A. Handwerker. A predictive model for whisker formation based on local microstructure and grain boundary properties. *JOM*, 65(10):1350–1361, Oct 2013.

[23] P. Sarobol, J.E. Blendell, and C.A. Handwerker. Whisker and hillock growth via coupled localized coble creep, grain boundary sliding, and shear induced grain boundary migration. *Acta Materialia*, 61(6):1991 – 2003, 2013.

[24] J. Smetana. Theory of tin whisker growth: "the end game". *IEEE Transactions on Electronics Packaging Manufacturing*, 30(1):11–22, Jan 2007.

[25] B.-Z. Lee and D.N. Lee. Spontaneous growth mechanism of tin whiskers. *Acta Materialia*, 46(10):3701 – 3714, 1998.

[26] Lucine Reinbold, Nitin Jadhav, Eric Chason, and K. Sharvan Kumar. Relation of sn whisker formation to intermetallic growth: Results from a novel Sn-Cu "bimetal ledge specimen". *Journal of Materials Research*, 24(12):3583–3589, 2009.

[27] C Trinks and Cynthia Volkert. Transition from dislocation glide to creep controlled damage in fatigued thin Cu films. *Journal of Applied Physics*, 114:093510–093510, 09 2013.

[28] Brian Alger, David Andrš, Robert W. Carlsen, Derek R. Gaston, Fande Kong, Alexander D. Lindsay, Jason M. Miller, Cody J. Permann, John W. Peterson, Andrew E. Slaughter, and Roy Stogner. *MOOSE Web page*, 2020. `https://mooseframework.org`.

[29] K. Chockalingam, M. Tonks, J. Hales, D. Gaston, P. Millett, and Liangzhe Zhang. Crystal plasticity with Jacobian-Free Newton-Krylov. *Computational Mechanics*, 51(5):617–627, 2013.

[30] Nicolò Grilli and Marisol Koslowski. The effect of crystal orientation on shock loading of single crystal energetic materials. *Computational Materials Science*, 155:235–245, 2018.

[31] F. Roters, P. Eisenlohr, L. Hantcherli, D.D. Tjahjanto, T.R. Bieler, and D. Raabe. Overview of constitutive laws, kinematics, homogenization and multiscale methods in crystal plasticity finite-element modeling: Theory, experiments, applications. *Acta Materialia*, 58(4):1152 – 1211, 2010.

[32] V. T. Deshpande and D. B. Sirdeshmukh. Thermal expansion of tetragonal tin. *Acta Crystallographica*, 14(4):355–356, 1961.

[33] A. Zamiri, T.R. Bieler, and F. Pourboghrat. Anisotropic crystal plasticity finite element modeling of the effect of crystal orientation and solder joint geometry on deformation after temperature change. *Journal of Electronic Materials*, 38(2):231–240, 2009.

[34] P. Darbandi, T.R. Bieler, F. Pourboghrat, and Tae-kyu Lee. Crystal plasticity finite-element analysis of deformation behavior in multiple-grained lead-free solder joints. *Journal of Electronic Materials*, 42(2):201–214, 2013.

[35] P Darbandi, Tk Lee, Tr Bieler, and F Pourboghrat. Crystal plasticity finite element study of deformation behavior in commonly observed microstructures in lead free solder joints. *Computational Materials Science*, 85(C):236–243, 2014.

[36] L. Zhao, P. Chakraborty, M.R. Tonks, and I. Szlufarska. On the plastic driving force of grain boundary migration: A fully coupled phase field and crystal plasticity model. *Computational Materials Science*, 128:320 – 330, 2017.

[37] B. Duzgun, A.E. Ekinci, I. Karaman, and N. Ucar. Investigation of dislocation movements and deformation characteristics in β-sn single crystals. *Journal of the Mechanical Behavior of Materials*, 10(3):187–203, 1999.

[38] J.P. Tucker, D.K. Chan, G. Subbarayan, and C.A. Handwerker. Maximum entropy fracture model and its use for predicting cyclic hysteresis in Sn3.8Ag0.7Cu and Sn3.0Ag0.5 solder alloys. *Microelectronics Reliability*, 54(11):2513–2522, 2014.

[39] R. Darveaux. Shear deformation of lead free solder joints. In *Proceedings Electronic Components and Technology, 2005. ECTC '05.*, pages 882–893 Vol. 1, May 2005.

[40] Eric Chason, Fei Pei, Nupur Jain, and Andrew Hitt. Studying the effect of grain size on whisker nucleation and growth kinetics using thermal strain. *Journal of Electronic Materials*, 48(1):17–24, 2019.

[41] W. C. ELLIS. Growth of metal whiskers from the solid. *Growth and Perfection of Crystals*, 1958.

[42] V.K. Glazunova and K.M. Gorbunova. Spontaneous growth of whiskers from electrodeposited coatings. *Journal of Crystal Growth*, 10(1):85 – 90, 1971.

[43] R. Kobayashi, J.A. Warren, and W.C. Carter. Vector-valued phase field model for crystallization and grain boundary formation. *Physica D: Nonlinear Phenomena*, 119(3):415 – 423, 1998.

[44] Ryo Kobayashi, James A. Warren, and W. Craig Carter. A continuum model of grain boundaries. *Physica D: Nonlinear Phenomena*, 140(1):141 – 150, 2000.

[45] Michael Tonks and Paul Millett. Phase field simulations of elastic deformation-driven grain growth in 2D copper polycrystals. *Materials Science and Engineering: A*, 528(12):4086 – 4091, 2011.

[46] Marisol Koslowski, Dong Wook Lee, and Lei Lei. Role of grain boundary energetics on the maximum strength of nanocrystalline Nickel. *Journal of the Mechanics and Physics of Solids*, 59(7):1427 – 1436, 2011.

[47] M.A. Bhatia, I. Adlakha, G. Lu, and K.N. Solanki. Generalized stacking fault energies and slip in β-tin. *Scripta Materialia*, 123:21 – 25, 2016.

[48] R.D. Doherty, D.A. Hughes, F.J. Humphreys, J.J. Jonas, D.Juul Jensen, M.E. Kassner, W.E. King, T.R. McNelley, H.J. McQueen, and A.D. Rollett. Current issues in recrystallization: a review. *Materials Science and Engineering: A*, 238(2):219 – 274, 1997.

[49] Y. Xie and M. Koslowski. Inelastic recovery in nano and ultrafine grained materials. *Modelling and Simulation in Materials Science and Engineering*, 24(5):055003, may 2016.

[50] J. F. Nye. Some geometrical relations in dislocated crystals. *Acta Metallurgica*, 1:153–162, 1953.

[51] Toshio Mura. *Micromechanics of defects in solids*. Springer Science & Business Media, 2013.

[52] Paolo Cermelli and Morton Gurtin. On the characterization of geometrically necessary dislocations in finite plasticity. *Journal of the Mechanics and Physics of Solids*, 49:1539–1568, 07 2001.

[53] Y. F. Gao, B. C. Larson, J. H. Lee, L. Nicola, J. Z. Tischler, and G. M. Pharr. Lattice Rotation Patterns and Strain Gradient Effects in Face-Centered-Cubic Single Crystals Under Spherical Indentation. *Journal of Applied Mechanics*, 82(6), 06 2015. 061007.

[54] D.A. Hughes, Q. Liu, D.C. Chrzan, and N. Hansen. Scaling of microstructural parameters: Misorientations of deformation induced boundaries. *Acta Materialia*, 45(1):105 – 112, 1997.

[55] M. Jahedi, M. Ardeljan, I.J. Beyerlein, M.H. Paydar, and M. Knezevic. Enhancement of orientation gradients during simple shear deformation by application of simple compression. *Journal of Applied Physics*, 117(21):214309, 2015.

[56] D.A. Hughes and N. Hansen. High angle boundaries formed by grain subdivision mechanisms. *Acta Materialia*, 45(9):3871 – 3886, 1997.

[57] D.A Hughes and N Hansen. Microstructure and strength of nickel at large strains. *Acta Materialia*, 48(11):2985 – 3004, 2000.

[58] F. Pei, N. Jadhav, and E. Chason. Correlating whisker growth and grain structure on Sn-Cu samples by real-time scanning electron microscopy and backscattering diffraction characterization. *Applied Physics Letters*, 100, 05 2012.

[59] K.N Tu. Irreversible processes of spontaneous whisker growth in bimetallic Cu-Sn thin-film reactions. *Physical review. B, Condensed matter*, 49(3):2030, 1994.

[60] W.J Boettinger, C.E Johnson, L.A Bendersky, K.-W Moon, M.E Williams, and G.R Stafford. Whisker and hillock formation on Sn, Sn-Cu and Sn-Pb electrodeposits. *Acta Materialia*, 53(19):5033–5050, 2005.

[61] S. Aubry and M. Ortiz. The mechanics of deformation-induced subgrain-dislocation structures in metallic crystals at large strains. *Proceedings of The Royal Society A: Mathematical, Physical and Engineering Sciences*, 459:3131–3158, 12 2003.

[62] WH Chen, P. Sarobol, J.R. Holaday, C.A. Handwerker, and J.E. Blendell. Effect of crystallographic texture, anisotropic elasticity, and thermal expansion on whisker formation in β-Sn thin films. *Journal of Materials Research*, 29(2):197–206, 2014.

[63] T Laurila, V Vuorinen, and J.K Kivilahti. Interfacial reactions between lead-free solders and common base materials. *Materials Science and Engineering R*, 49(1):1–60, 2005.

[64] Chaoran Yang, Fuliang Le, and S.W. Ricky Lee. Experimental investigation of the failure mechanism of Cu-Sn intermetallic compounds in SAC solder joints. *Microelectronics Reliability*, 62:130–140, 2016.

[65] Z. Huang, P. Kumar, I. Dutta, R. Sidhu, M. Renavikar, and R. Mahajan. Incorporation of interfacial intermetallic morphology in fracture mechanism map for Sn-Ag-Cu solder joints. *Journal of Electronic Materials*, 43(1):88–95, 2014.

[66] Q.K Zhang and Z.F Zhang. Fracture mechanism and strength-influencing factors of Cu/Sn-4Ag solder joints aged for different times. *Journal of Alloys and Compounds*, 485(1-2):853–861, 2009.

[67] Tong An and Fei Qin. Effects of the intermetallic compound microstructure on the tensile behavior of Sn3.0Ag0.5Cu/Cu solder joint under various strain rates. *Microelectronics Reliability*, 54(5):932–938, 2014.

[68] Rui Zhang, Yanhong Tian, Chunjin Hang, Baolei Liu, and Chunqing Wang. Formation mechanism and orientation of Cu_3Sn grains in Cu-Sn intermetallic compound joints. *Materials Letters*, 110:137–140, 2013.

[69] Hsiang-Yao Hsiao, Chien-Min Liu, Han-Wen Lin, Tao-Chi Liu, Chia-Ling Lu, Yi-Sa Huang, Chih Chen, and K N Tu. Unidirectional growth of microbumps on (111)-oriented and nanotwinned copper. *Science (New York, N.Y.)*, 336(6084):1007, 2012.

[70] Wei Liu, Yanhong Tian, Chunqing Wang, Xuelin Wang, and Ruiyang Liu. Morphologies and grain orientations of Cu-Sn intermetallic compounds in Sn3.0Ag0.5Cu/Cu solder joints. *Materials Letters*, 86:157–160, 2012.

[71] G Ghosh. Elastic properties, hardness, and indentation fracture toughness of intermetallics relevant to electronic packaging. *Journal of Materials Research*, 19(5):1439–1454, 2004.

[72] Chaoran Yang, Fubin Song, and S. W. R Lee. Effect of interfacial strength between Cu_6Sn_5 and Cu_3Sn intermetallics on the brittle fracture failure of lead-free solder joints with OSP pad finish. In *2011 IEEE 61st Electronic Components and Technology Conference (ECTC)*, pages 971–978. IEEE, 2011.

[73] Z. Huang, P. Kumar, I. Dutta, J.H.L. Pang, R. Sidhu, M. Renavikar, and R. Mahajan. Fracture of Sn-Ag-Cu solder joints on Cu substrates: I. effects of loading and processing conditions. *Journal of Electronic Materials*, 41(2):375–389, 2012.

[74] Chaoran Yang, Guangsui Xu, S. W. Ricky Lee, and Xinping Zhang. Brittle fracture of intermetallic compounds in SAC solder joints under high speed ball pull/pin pull and Charpy impact tests. In *2013 IEEE 63rd Electronic Components and Technology Conference*, pages 1294–1299. IEEE, 2013.

[75] Hong-Bo Qin and Xin-Ping Zhang. Three-dimensional finite element analysis of mechanical and fracture behavior of micro-scale BGA structure solder joints containing cracks in the intermetallic compound layer. In *2012 13th International Conference on Electronic Packaging Technology & High Density Packaging*, pages 1244–1249. IEEE, 2012.

[76] Saeed Akbari, Amir Nourani, and Jan Spelt. Effect of solder joint length on fracture under bending. *Journal of Electronic Materials*, 45(1):473–485, 2016.

[77] Yuan-Wei Chang, Yin Cheng, Feng Xu, Lukas Helfen, Tian Tian, Marco Di Michiel, Chih Chen, King-Ning Tu, and Tilo Baumbach. Study of electromigration-induced formation of discrete voids in flip-chip solder joints by in-situ 3D laminography observation and finite-element modeling. *Acta Materialia*, 117(C):100–110, 2016.

[78] Yuan-Wei Chang, Yin Cheng, Lukas Helfen, Feng Xu, Tian Tian, Mario Scheel, Marco Di Michiel, Chih Chen, King-Ning Tu, and Tilo Baumbach. Electromigration mechanism of failure in flip-chip solder joints based on discrete void formation. *Sci Rep*, 7(1):17950–17950, 2017.

[79] Glenn Ross, Vesa Vuorinen, and Mervi Paulasto-Krckel. Void formation and its impact on CuSn intermetallic compound formation. *Journal of Alloys and Compounds*, 677:127–138, 2016.

[80] Xiaoqin Lin and Le Luo. Void evolution in sub-100-micron Sn-Ag solder bumps during multi-reflow and aging and its effects on bonding reliability. *Journal of Electronic Materials*, 37(3):307–313, 2008.

[81] *Metals handbook*. Second edition. edition, 1998.

[82] *Metals handbook*. American Society for Metals, Metals Park, Ohio, 9th ed. edition, 1978.

[83] Yuesong Xie, Oleksandr G Kravchenko, R. Byron Pipes, and Marisol Koslowski. Phase field modeling of damage in glassy polymers. *Journal of the Mechanics and Physics of Solids*, 93:182–197, 2016.

[84] Bogdan Tanasoiu and Marisol Koslowski. A parametric study of the dynamic failure of energetic composites. *Journal of Applied Physics*, 122(12), 2017.

[85] Akshay Dandekar, Zane A Roberts, Shane Paulson, Weinong Chen, Steven F Son, and Marisol Koslowski. The effect of the particle surface and binder properties on the response of polymer bonded explosives at low impact velocities. *Computational Materials Science*, 166:170–178, 2019.

[86] Nicolò Grilli, Camilo A. Duarte, and Marisol Koslowski. Dynamic fracture and hot-spot modeling in energetic composites. *Journal of Applied Physics*, 123(6), 2018.

[87] Camilo A. Duarte, Nicolò Grilli, and Marisol Koslowski. Effect of initial damage variability on hot-spot nucleation in energetic materials. *Journal of Applied Physics*, 124(2), 2018.

[88] Pritam Chakraborty, Yongfeng Zhang, and Michael R Tonks. Multi-scale modeling of microstructure dependent intergranular brittle fracture using a quantitative phase-field based method. *Computational Materials Science*, 113(C):38–52, 2016.

[89] Van Luong Nguyen, Chin-Sung Chung, and Ho-Kyung Kim. The tensile impact properties of aged Sn-3Ag-0.5Cu/Cu solder joints. *Microelectronics Reliability*, 55(12):2808–2816, 2015.

[90] RJ Fields, SR Low III, GK Lucey Jr, MJ Cieslak, JH Perepezko, S Kang, et al. The metal science of joining. In *TMS Symp. Proc. 165 (The Metallurgical Society, 1992)*, 1992.

[91] A. Hohenwarter and R. Pippan. Fracture and fracture toughness of nanopolycrystalline metals produced by severe plastic deformation. *Philosophical transactions. Series A, Mathematical, physical, and engineering sciences*, 373(2038), 2015.

[92] Peter Ratchev, Tony Loccufier, Bart Vandevelde, Bert Verlinden, Steven Teliszewski, Daniel Werkhoven, and Bart Allaert. A study of brittle to ductile fracture transition temperatures in bulk Pb-free solders. 2005.

[93] Eric Buchovecky, Nitin Jadhav, Allan Bower, and Eric Chason. Finite element modeling of stress evolution in Sn films due to growth of the Cu_6Sn_5 intermetallic compound. *Journal of Electronic Materials*, 38(12):2676–2684, 2009.

[94] Varun A Baheti, Sanjay Kashyap, Praveen Kumar, Kamanio Chattopadhyay, and Aloke Paul. Bifurcation of the Kirkendall marker plane and the role of Ni and other impurities on the growth of Kirkendall voids in the Cu-Sn system. *Acta Materialia*, 131:260–270, 2017.

[95] Liping Mo, Zhichao Chen, Fengshun Wu, and Changqing Liu. Microstructural and mechanical analysis on Cu-Sn intermetallic micro-joints under isothermal condition, Jan 2015.

[96] J.F Li, P.A Agyakwa, and C.M Johnson. Interfacial reaction in Cu/Sn/Cu system during the transient liquid phase soldering process. *Acta materialia*, 59(3):1198–1211, 2011.

[97] Jiayun Feng, Chunjin Hang, Yanhong Tian, Chenxi Wang, and Baolei Liu. Effect of electric current on grain orientation and mechanical properties of Cu-Sn intermetallic compounds joints. *Journal of alloys and compounds*, 753:203–211, 2018.

[98] P.J Shang, Z.Q Liu, X.Y Pang, D.X Li, and J.K Shang. Growth mechanisms of Cu3Sn on polycrystalline and single crystalline Cu substrates. *Acta materialia*, 57(16):4697–4706, 2009.

[99] K.E Yazzie, H.E Fei, H Jiang, and N Chawla. Rate-dependent behavior of Sn alloy-Cu couples: Effects of microstructure and composition on mechanical shock resistance. *Acta Materialia*, 60(10):4336–4348, 2012.

[100] Tong An and Fei Qin. Effects of the intermetallic compound microstructure on the tensile behavior of Sn3.0Ag0.5Cu/Cu solder joint under various strain rates. *Microelectronics Reliability*, 54(5):932–938, 2014.

[101] Yifei Zeng, Xiaorong Cai, and Marisol Koslowski. Effects of the stacking fault energy fluctuations on the strengthening of alloys. *Acta Materialia*, 164:1–11, 2019.

[102] Alan J Ardell. Precipitation hardening. *Metallurgical Transactions A*, 16(12):2131–2165, 1985.

[103] Jacques Friedel. *Dislocations*. Pergamon Press Oxford, 1964.

[104] Rea Labusch. A statistical theory of solid solution hardening. *Physica Status Solidi (b)*, 41(2):659–669, 1970.

[105] Michael Zaiser. Dislocation motion in a random solid solution. *Philosophical Magazine A*, 82(15):2869–2883, 2002.

[106] Libor Kovarik, Raymond R. Unocic, Ju Li, P. Sarosi, C. Shen, Yunzhi Wang, and Michael J. Mills. Microtwinning and other shearing mechanisms at intermediate temperatures in Ni-based superalloys. *Progress in Materials Science*, 54(6):839–873, 2009.

[107] Akiyuki Takahashi, Mitsuru Kawanabe, and Nasr M. Ghoniem. γ-precipitate strengthening in nickel-based superalloys. *Philosophical Magazine*, 90(27-28):3767–3786, 2010.

[108] Raymond R Unocic, Ning Zhou, Libor Kovarik, Chen Shen, Yunzhi Wang, and Michael J Mills. Dislocation decorrelation and relationship to deformation microtwins during creep of a γ precipitate strengthened Ni-based superalloy. *Acta Materialia*, 59(19):7325–7339, 2011.

[109] Minsheng Huang and Zhenhuan Li. The key role of dislocation dissociation in the plastic behaviour of single crystal nickel-based superalloy with low stacking fault energy: Three-dimensional discrete dislocation dynamics modelling. *Journal of the Mechanics and Physics of Solids*, 61(12):2454–2472, 2013.

[110] Peter B Hirsch and Anthony Kelly. Stacking-fault strengthening. *Philosophical Magazine*, 12(119):881–900, 1965.

[111] Daniel B Miracle and Oleg N Senkov. A critical review of high entropy alloys and related concepts. *Acta Materialia*, 122:448–511, 2017.

[112] Oleg N Senkov, GB Wilks, JM Scott, and Daniel B Miracle. Mechanical properties of $Nb_{25}Mo_{25}Ta_{25}W_{25}$ and $V_{20}Nb_{20}Mo_{20}Ta_{20}W_{20}$ refractory high entropy alloys. *Intermetallics*, 19(5):698–706, 2011.

[113] Oleg N Senkov, Svetlana V Senkova, Christopher Woodward, and Daniel B Miracle. Low-density, refractory multi-principal element alloys of the Cr–Nb–Ti–V–Zr system: Microstructure and phase analysis. *Acta Materialia*, 61(5):1545–1557, 2013.

[114] Frederik Otto, A Dlouhỳ, Ch Somsen, Hongbin Bei, G Eggeler, and Easo P George. The influences of temperature and microstructure on the tensile properties of a CoCrFeMnNi high-entropy alloy. *Acta Materialia*, 61(15):5743–5755, 2013.

[115] Andrey V Kuznetsov, Dmitry G Shaysultanov, Nikita D Stepanov, Gennady A Salishchev, and Oleg N Senkov. Tensile properties of an AlCrCuNiFeCo high-entropy alloy in as-cast and wrought conditions. *Materials Science and Engineering: A*, 533:107–118, 2012.

[116] Yong Zhang, Ting Ting Zuo, Zhi Tang, Michael C Gao, Karin A Dahmen, Peter K Liaw, and Zhao Ping Lu. Microstructures and properties of high-entropy alloys. *Progress in Materials Science*, 61:1–93, 2014.

[117] Céline Varvenne, Gerard Paul M. Leyson, Maryam Ghazisaeidi, and William A Curtin. Solute strengthening in random alloys. *Acta Materialia*, 124:660–683, 2017.

[118] Céline Varvenne, Aitor Luque, and William A Curtin. Theory of strengthening in fcc high entropy alloys. *Acta Materialia*, 118:164–176, 2016.

[119] Joseph A Yasi, Louis G Hector, and Dallas R Trinkle. First-principles data for solid-solution strengthening of magnesium: From geometry and chemistry to properties. *Acta Materialia*, 58(17):5704–5713, 2010.

[120] Satish.I. Rao, Christopher Woodward, Triplicane A. Parthasarathy, and Oleg Senkov. Atomistic simulations of dislocation behavior in a model fcc multicomponent concentrated solid solution alloy. *Acta Materialia*, 134(Supplement C):188 – 194, 2017.

[121] Timothy M. Smith, Mohammad Shahriar Hooshmand, Bryan D. Esser, Frederik Otto, David W. McComb, Easo P. George, Maryam Ghazisaeidi, and Margaret J. Mills. Atomic-scale characterization and modeling of 60° dislocations in a high-entropy alloy. *Acta Materialia*, 110:352 – 363, 2016.

[122] Y.H. Zhang, Yu Zhuang, Alice Hu, Ji-Jung Kai, and Chaintsuan T. Liu. The origin of negative stacking fault energies and nano-twin formation in face-centered cubic high entropy alloys. *Scripta Materialia*, 130:96 – 99, 2017.

[123] Shuo Huang, He Huang, Wei Li, Dongyoo Kim, Song Lu, Xiaoqing Li, Erik Holmstrm, Se Kwon, and Levente Vitos. Twinning in metastable high-entropy alloys. *Nature Communications*, 9(1):1–7, 2018.

[124] Gerard Paul M Leyson, William A Curtin, Louis G Hector, and Christopher F Woodward. Quantitative prediction of solute strengthening in aluminium alloys. *Nature Materials*, 9(9):750, 2010.

[125] Gerard Paul M Leyson, Louis G Hector, and William A Curtin. Solute strengthening from first principles and application to aluminum alloys. *Acta Materialia*, 60(9):3873–3884, 2012.

[126] Gerard Paul M Leyson, Louis G Hector, and William A Curtin. First-principles prediction of yield stress for basal slip in Mg–Al alloys. *Acta Materialia*, 60(13):5197–5203, 2012.

[127] Vaclav Vitek. Intrinsic stacking faults in body-centred cubic crystals. *Philosophical Magazine*, 18(154):773–786, 1968.

[128] Sonia Raujol, Mustafa Benyoucef, Didier Locq, Pierre Caron, F Pettinari, Nicole Clément, and Armand Coujou. Decorrelated movements of shockley partial dislocations in the γ-phase channels of nickel-based superalloys at intermediate temperature. *Philosophical Magazine*, 86(9):1189–1200, 2006.

[129] Marc Condat and Brigitte Décamps. Shearing of γ precipitates by single $a/2 <$ $110 >$ matrix dislocations in a γ/γ Ni-based superalloy. *Scripta Metallurgica*, 21(5):607–612, 1987.

[130] Hideji Suzuki. Chemical interaction of solute atoms with dislocations. *Science Reports of the Research Institutes, Tohoku University. Ser. A, Physics, chemistry and metallurgy*, 4:455–463, 1952.

[131] Robert L Fleisgher. Solution hardening. *Acta Metallurgica*, 9(11):996–1000, 1961.

[132] Robert L Fleischer. Substitutional solution hardening. *Acta Metallurgica*, 11(3):203–209, 1963.

[133] Nevill Francis Mott and Frank Nabarro. *Dislocation theory and transient creep*. Physical Society, 1948.

[134] Nevill Francis Mott. A theory of work-hardening of metal crystals. *The London, Edinburgh, and Dublin Philosophical Magazine and Journal of Science*, 43(346):1151–1178, 1952.

[135] Abigail Hunter, Hariharanath Kavuri, and Marisol Koslowski. A continuum plasticity model that accounts for hardening and size effects in thin films. *Modelling and Simulation in Materials Science and Engineering*, 18(4):045012, 2010.

[136] Dong Wook Lee, Hojin Kim, Alejandro Strachan, and Marisol Koslowski. Effect of core energy on mobility in a continuum dislocation model. *Physical Review B*, 83(10):104101, 2011.

[137] Abigail Hunter, Ruifeng Zhang, Irene J Beyerlein, Timothy C Germann, and Marisol Koslowski. Dependence of equilibrium stacking fault width in fcc metals on the γ-surface. *Modelling and Simulation in Materials Science and Engineering*, 21(2):025015, 2013.

[138] Gunther Schoeck. The core structure, recombination energy and peierls energy for dislocations in Al. *Philosophical Magazine A*, 81(5):1161–1176, 2001.

[139] Joël Douin, Florence Pettinari-Sturmel, and Armand Coujou. Dissociated dislocations in confined plasticity. *Acta Materialia*, 55(19):6453–6458, 2007.

[140] Enrique Martinez, Jaime Marian, Athanasios Arsenlis, Max P Victoria, and Jose Manuel Perlado. Atomistically informed dislocation dynamics in fcc crystals. *Journal of the Mechanics and Physics of Solids*, 56(3):869–895, 2008.

[141] John Price Hirth and Jens Lothe. *Theory of Dislocations*. McGraw-Hill, New York, 1968.

[142] Helena Van Swygenhoven, Peter M. Derlet, and Anders Gudmund Frseth. Stacking fault energies and slip in nanocrystalline metals. *Nature Materials*, 3(6), May 2004.

[143] Sheela Singh, Nelia Wanderka, Klaus Kiefer, Konrad Siemensmeyer, and John Banhart. Effect of decomposition of the Cr–Fe–Co rich phase of AlCoCrCuFeNi high entropy alloy on magnetic properties. *Ultramicroscopy*, 111(6):619–622, 2011.

VITA

VITA

Xiaorong Cai obtained a Bachelors of Science degree in Mechanical Engineering in 2016 from Shanghai Jiao Tong University, Shanghai, China. She came to Purdue University in Mechanical Engineering Department as an exchange student in 2015 and enrolled as a master student in fall of 2016. She joined Prof. Koslowski's research group and converted to a direct PhD in spring of 2017. Her research interests focus on multiscale computational modeling of deformation process and material properties of crystalline materials using phase field method and phase field dislocation dynamics.